Airborne ultrasound phased arrays

Phased Arrays für luftgekoppelten Ultraschall
Zur Erlangung des akademischen Grades Doktor-Ingenieur (Dr.-Ing.)
genehmigte Dissertation von Dipl.-Ing. Axel Jäger aus Frankfurt
Tag der Einreichung: 30. Oktober 2018, Tag der Prüfung: 28. Januar 2019
Darmstadt — D 17

1. Gutachten: Prof. Dr. Mario Kupnik
2. Gutachten: Prof. Dr. Bernd Henning

TECHNISCHE
UNIVERSITÄT
DARMSTADT

Fachbereich
Elektrotechnik und Informationstechnik
Fachgebiet Mess- und Sensortechnik

Airborne ultrasound phased arrays
Phased Arrays für luftgekoppelten Ultraschall

Genehmigte Dissertation von Dipl.-Ing. Axel Jäger aus Frankfurt

1. Gutachten: Prof. Dr. Mario Kupnik
2. Gutachten: Prof. Dr. Bernd Henning

Tag der Einreichung: 30. Oktober 2018
Tag der Prüfung: 28. Januar 2019

Darmstadt — D 17

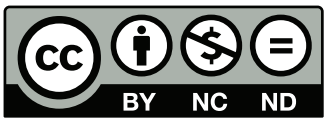

Erklärung zur Dissertation

Hiermit versichere ich, die vorliegende Dissertation ohne Hilfe Dritter nur mit den angegebenen Quellen und Hilfsmitteln angefertigt zu haben. Alle Stellen, die aus Quellen entnommen wurden, sind als solche kenntlich gemacht. Diese Arbeit hat in gleicher oder ähnlicher Form noch keiner Prüfungsbehörde vorgelegen.

Darmstadt, den 16. Oktober 2019

(A. Jäger)

Zusammenfassung

Diese Arbeit beschreibt die Entwicklung und Charakterisierung eines 2D-Luftultraschall-Phased-Arrays unter Verwendung eines 3D-gedruckten Wellenleiters. Der Wellenleiter ermöglicht einen Elementabstand von $\lambda/2$ mit existierenden Ultraschallwandlern, deren Baugröße $\lambda/2$ übersteigt. Mit einem Elementabstand von $\lambda/2$ wird eine grating-lobe-freie Abstrahlcharakteristik realisiert. Neben der verbesserten Abstrahlcharakteristik wird die räumliche Trennung von Wandlern und akustisch aktiver Apertur ermöglicht. Dies erlaubt die freie Anordnung der Ultraschallwandler im Bauraum und den Einsatz größerer und leistungsstärkerer Ultraschallwandler, da die Wandlergröße nicht durch die Elementanordnung beschränkt ist.

Neben dem Entwurf des Wellenleiters wird eine Phased-Array-Elektronik vorgestellt, welche Beamforming beim Senden und Empfangen von Ultraschallsignalen ermöglicht. Weiterhin wird die benötigte Signalverarbeitungsarchitektur zum Empfangsbeamforming vorgestellt. Die Signalverarbeitung nutzt GPU-Beschleunigung, womit eine instantane Auswertung der empfangenen Signale erreicht wird.

Mit dem aufgebauten System werden verschiedene Beispielanwendungen realisiert. Die erste Anwendung ist eine Gasdurchflussmessung nach dem Laufzeitprinzip. Durch die Verwendung des Arrays wird, im Vergleich zu konventionellen Einzelwandlern, der messbare Geschwindigkeitsbereich erweitert.

Weiterhin wird die Bildgebung basierend auf der Pulse-Echo-Ortung demonstriert. Dieses Verfahren ist in der medizinischen Sonographie, sowie in Sonarsystemen unter Wasser Stand der Technik. In der vorliegenden Arbeit wird dieses Verfahren auf Luftultraschall übertragen. Hierfür wird eine Charakterisierung mit verschiedenen Messreihen durchgeführt. Dabei konnten Reichweiten bis zu 6 m demonstriert werden. Die erreichbare laterale Auflösung zum Trennen zweier nebeneinander liegender Objekte beträgt mindestens 12°. Weiterhin können hintereinander liegende, sich verdeckende Objekte mit einer axialen Auflösung von 200 mm aufgelöst werden.

Mit Hilfe der Schlierenfotografie konnte das Beamforming sichtbar gemacht werden. Die dazu notwendige Bildverarbeitung wird vorgestellt. Die Schlierenaufnahmen dienen dem qualitativen Vergleich zwischen Simulation und realem Beamformingverhalten.

Die entwickelte Plattform ermöglicht die Evaluation verschiedener weiterer Ultraschallapplikationen. Hierzu zählen die zerstörungsfreie Materialprüfung mit Hilfe von Lamb-Wellen, welche Gegenstand aktueller Forschung am Fachgebiet Mess- und Sensortechnik an der Technischen Universität Darmstadt sind. Weiterhin wird bereits die Umfelderfassung für Robotikanwendungen mit Hilfe des Arrays untersucht und mit etablierten Sensorsystemen verglichen. Neben den Ultraschallapplikationen ist die entwickelte Plattform ein Modellsystem für verschiedene Fragestellungen der Signalverarbeitung und Kommunikationstechnik.

Abstract

This work shows the development and the characterization of an air-coupled ultrasonic phased array using a 3D-printed waveguide. The waveguide allows an element distance of $\lambda/2$ with existing ultrasonic transducers exceeding $\lambda/2$ dimension. With an element distance of $\lambda/2$, a grating-lobe-free radiation characteristic is realized. In addition to the improved radiation characteristic, the spatial separation of transducers and the acoustically active aperture is achieved. This allows the free arrangement of the ultrasonic transducers in the design space and the use of larger and more powerful ultrasonic transducers, since the transducer size is not limited by the element arrangement.

Apart from the design of the waveguide, phased array electronics is presented which enables transmit and receive beamforming of ultrasonic signals. Furthermore, the required signal processing architecture for receive beamforming is presented. The signal processing uses GPU-acceleration to achieve an immediate evaluation of the received signals.

Different applications are demonstrated with the built up system. The first application is a gas flow metering based on the the time-of-flight-principle. By exploiting the electronic beam steering, the measurable velocity range is extended compared to conventional single transducers.

Furthermore, the imaging based on pulse echo localization is demonstrated. This method is state of the art in medical imaging as well as in sonar systems under water. In this thesis, this method is transferred to air-coupled ultrasound. For this, a characterization with different measurement series is carried out. It was possible to demonstrate ranges up to 6 m. The achievable lateral resolution for separating two adjacent objects is at least 12°. Furthermore, successive objects can be resolved with an axial resolution of 200 mm.

In another experiment the beamforming of sound waves is made visible with the help of schlieren photography. The necessary image processing is presented. The schlieren images are used for the comparison between simulation and the real beamforming behavior.

The developed platform enables the evaluation of additional ultrasonic applications. These include non-destructive testing using Lamb waves, which are the subject of current research at the Measurement and Sensor Technology Group at the Technische Universität Darmstadt. Furthermore, the field monitoring for robotic applications is already being investigated using the array and compared with established sensor systems.

In addition to these ultrasound applications, the developed platform is a model system for various questions of signal processing and communication technology.

List of own publications

A. Jäger, D. Grokurth, M. Rutsch, A. Unger, R. Golinske, H. Wang, S. Dixon, K. Hofmann, and M. Kupnik. "Air-coupled 40-kHz ultrasonic 2D-phased array based on a 3D-printed waveguide structure". In: *2017 IEEE International Ultrasonics Symposium (IUS)*. 2017. DOI: 10.1109/ULTSYM.2017.8092532

A. Jäger, A. Unger, H. Wang, Y. Arnaudov, L. Kang, R. Su, D. Lines, S. N. Ramadas, S. Dixon, and M. Kupnik. "Ultrasonic phased array for sound drift compensation in gas flow metering". In: *2017 IEEE International Ultrasonics Symposium (IUS)*. 2017. DOI: 10.1109/ULTSYM.2017.8092174

A. Jäger, S. Johannesmann, L. Claes, M. Webersen, B. Henning, and M. Kupnik. "Evaluating the influence of 3D-printing parameters on acoustic material properties". In: *2017 IEEE International Ultrasonics Symposium (IUS)*. Nov. 2017, pp. 1–4. DOI: 10.1109/ULTSYM.2017.8092398

L. Claes, A. Jäger, S. Johannesmann, M. Webersen, M. Kupnik, and B. Henning. "Acoustic Material Characterization of Additively Manufactured Components". In: *Proceedings Sensor 2017*. 2017, pp. 605–610. DOI: 10.5162/sensor2017/P2.9

L. Kang, A. Feeney, R. Su, D. Lines, A. Jäger, H. Wang, Y. Arnaudov, S. N. Ramadas, M. Kupnik, and S. Dixon. "Two-dimensional flexural ultrasonic phased array for flow measurement". In: *2017 IEEE International Ultrasonics Symposium (IUS)*. Sept. 2017, pp. 1–4. DOI: 10.1109/ULTSYM.2017.8092220

M. Hoffmann, A. Unger, A. Jäger, and M. Kupnik. "Effect of transducer port cavities in invasive ultrasonic transit-time gas flowmeters". In: *2015 IEEE International Ultrasonics Symposium (IUS)*. Oct. 2015, pp. 1–4. DOI: 10.1109/ULTSYM.2015.0272

Conference talks

A. Jäger, D. Grokurth, M. Rutsch, A. Unger, R. Golinske, H. Wang, S. Dixon, K. Hofmann, and M. Kupnik. "Air-coupled 40-kHz ultrasonic 2D-phased array based on a 3D-printed waveguide structure". In: *2017 IEEE International Ultrasonics Symposium (IUS)*. 2017. DOI: 10.1109/ULTSYM.2017.8092532

A. Jäger, A. Unger, H. Wang, Y. Arnaudov, L. Kang, R. Su, D. Lines, S. N. Ramadas, S. Dixon, and M. Kupnik. "Ultrasonic phased array for sound drift compensation in gas flow metering". In: *2017 IEEE International Ultrasonics Symposium (IUS)*. 2017. DOI: 10.1109/ULTSYM.2017.8092174

Conference posters

A. Jäger, S. Johannesmann, L. Claes, M. Webersen, B. Henning, and M. Kupnik. "Evaluating the influence of 3D-printing parameters on acoustic material properties". In: *2017 IEEE International Ultrasonics Symposium (IUS)*. Nov. 2017, pp. 1–4. DOI: 10.1109/ULTSYM.2017.8092398

Patents

A. Jäger and F. Klug. “Vertical interconnection on porous substrates with conductive ink”. DE 102016122508. 2016

Danksagung

Mein besonderer Dank gilt meinem Doktorvater, Herrn Professor Mario Kupnik, der mir die Gelegenheit gegeben hat, auf dem spannenden Gebiet der Phased-Arrays zu arbeiten und dieses entsprechend meiner persönlichen Interessen zu gestalten. Phased Arrays hatten mich schon vor dieser Arbeit fasziniert.

Ganz herzlich bedanken möchte ich mich bei Herrn Professor Bernd Henning für das Zweitgutachten meiner Arbeit sowie den fachlichen Austausch auf dem Gebiet der Schlierenfotografie.

Weiterer Dank gilt meinen beiden Korrekturlesern, Herrn Gianni Allevato und Herrn Dr. Stefan Schmidt. Besonders freue ich mich, dass ich zum September Herrn Allevato als neuen Kollegen begrüßen durfte. Er hat schon durch seine Masterarbeit im Bereich der Signalverarbeitung einen wesentlichen Beitrag zum Gelingen dieser Arbeit geleistet.

Ebenfalls bedanken möchte ich mich bei meinen beiden anderen Masterarbeitern, Herrn Jan Hinrichs und Herrn Dominik Großkurth, die im Bereich der Elektronik wesentliche Beiträge zu dieser Arbeit geleistet haben. Sie gehören mittlerweile ebenfalls zum Kollegenkreis.

Ein weiter Dank gilt den Herren Alexander Unger und Matthias Rutsch, die nicht nur wesentliche Vorarbeiten geleistet haben, ohne die meine Arbeit nie zustande gekommen wäre, sondern die auch durch Messungen im schalltoten Raum geholfen haben.

Ich möchte mich ebenso bei meinen Eltern, Frau Gisela Pusch-Jäger und Herrn Egon Jäger bedanken, die meine Neugierde stehts unterstützt haben und meinen Weg nie in Frage gestellt haben.

Contents

Acknowledgements

This work received funding from the European Research Council under the European Union's Seventh Framework Programme (FP7/2007-2013)/European Commission Ref. 612118.

1 Introduction

The phased-array-principle, first demonstrated by Ferdinand Braun in 1909 [8], is widely used in various engineering fields. Microwave applications utilizing phased arrays include telecommunications networks such as wireless lan (WIFI) or long term evolution (LTE) as well as various types of radio detection and ranging (RADAR) systems. Examples for ultrasound applications are medical imaging and high intensity focused ultrasound (HiFU)-therapy as well as non-destructive testing (NDT).

The principle utilizes multiple wave sources or receivers in conjunction. When the array is operated as a sender, each wave source is excited by an own, pre-calculated signal. The interference of the individually generated waves superimpose to a desired wave field. Changing the individual signals changes the overall beam characteristics of the array, and, thus, allows steering and focusing of a sound field controlled by software. When the array is operated as a receiver, each individual array member receives a slightly different signal and using all received signals in conjunction, the direction of a signal source can be obtained as well as multiple sources can be distinguished.

For air-coupled ultrasound, only recently promising new applications emerge that utilize phased arrays. These are acoustic levitation and haptic feedback. Significant contributions where made by the Drinkwater group from Bristol that published on both applications [9] [10] and also made the electronics publicly available for further research [11]. Both application utilize a phased array in the *near field*. This means that the area where a sample can be levitated or where a haptic impression is possible is close to the phased array itself. Close means the distance to the phased array is comparable to or even less than the dimensions of the array aperture size. Also, both applications use the phased array only as a sender, therefore only sending is implemented in the published electronic circuit.

Mature air-coupled ultrasound applications such as park distance control, sensors in industrial environments such as assembly lines or chemical processing plants do not benefit from those recent developments. These applications require either a pitch catch or a pulse echo configuration. In a pitch catch configuration, a dedicated sender and receiver work in conjunction whereas in a pulse echo configuration, the same transducer first transmits a pulse and then listens for the echo caused by the reflection on any object in the surrounding area. These applications operate in the far field and building a suitable array requires a distance of $\lambda/2$ or less between the individual transducers where λ is the wavelength.

One of the main challenges in designing a far field array from commercially available transducers is the fact that these transducers were not designed to be used in such a $\lambda/2$-array and, thus, have dimensions exceeding $\lambda/2$. Building smaller transducers is challenging as efficient air-coupled ultrasound transducers are designed as resonant systems. Therefore, the geometric dimensions cannot be chosen arbitrarily and even if a resonant system fitting into a $\lambda/2$-pitch was designed, the achievable sound pressure would be lower compared to the larger transducers due to the limited power density of the active material.

The goal of this thesis is the design of an air-coupled ultrasound array operating at a frequency of $f = 40\,\text{kHz}$ that is suitable for far field operation. The issue of transducer dimensions exceeding $\lambda/2$ is addressed by utilizing an additional component in front of the transducer array, a waveguide that shrinks the aperture pitch down to $\lambda/2$. This idea was already proposed by Langen[12] in 1996 where transducers larger than $\lambda/2$ are arranged in two rows and then alternately connected to an array aperture of smaller pitch [Figure 1.1 (a)]. Takahashi et al. showed an actual realization of this method for a sending 1×6-array [Figure 1.1 (b)] [13].

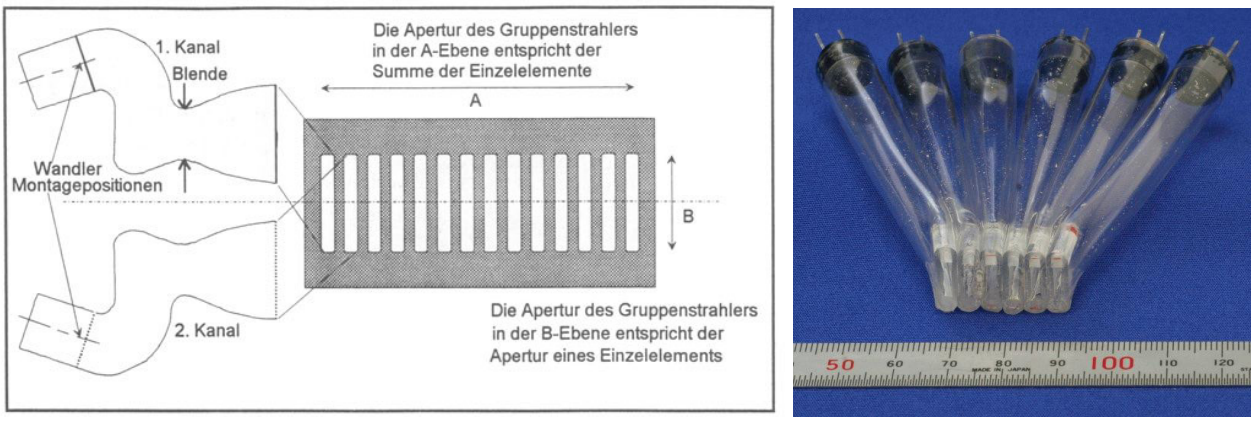

(a) (b)

Figure 1.1.: Proposed alternating waveguide by Langen [12] and realization by Takahashi [13] using heat shrink tubes. (a) is reprinted by permission from Springer Nature, *Analyse der Lösungsmöglichkeiten zur Konstruktion von Ultraschallköpfen* by Achim Langen (1993) [12]. (b) is reprinted with permission from SPIE Digital Library from T. Takahashi, R. Takahashi, S. Jeong, *Ultrasonic phased array sensor for electric travel aids for visually impaired people*, Proceedings Vol. 6794, ICMIT 2007: Mechatronics, MEMS, and Smart Materials, 2007, Gifu, Japan [13].

Unger et al. [14, 15] showed a more sophisticated variant using 8 array elements, each made up of 12 individual transducers (Figure 1.2). This array emits a more focused beam compared to the array of Takahashi et al. due to the larger acoustic aperture perpendicular to the array direction. In addition, receiving by using this array was also demonstrated [16].

Both arrays use the same ultrasound transducer (MA40S4S, Murata Seisakusho, Kyōto, Japan) [17], operating at a frequency of $f = 40\,\mathrm{kHz}$. This corresponds to a wavelength of $\lambda = 8.6\,\mathrm{mm}$. The transducer itself is cylindrically shaped, with a diameter of $\varnothing = 10\,\mathrm{mm}$ or $\varnothing 1.2\lambda$. A bundle of heat shrinking tubes reduces the aperture down to $\lambda/2 = 4.3\,\mathrm{mm}$. Both arrays use channels of the same length.

By using this approach, an evaluation of an air-coupled phased-array operating a 40 kHz is possible without designing dedicated transducers. Beside this primary function, the waveguide provides additional benefits such as thermal separation in harsh environments or the use of larger, more powerful transducers in a $\lambda/2$ array, resulting in higher sound pressures.

Similar acoustic waveguides that change the acoustic aperture of sound sources are a common building block in modern speakers for public address system (PA), providing audio playback for large audiences. One optimization goal of such systems is to cover the area of the audience with reasonable audio quality but to omit other areas. The directivity of a speaker is inversely related to the size of its acoustic aperture with respect to the wavelength. This means a wide speaker has a narrow sound beam in contrast to a narrow speaker that has a wide sound beam. Because the primary speaker driver is a resonant system, its dimensions cannot be chosen arbitrary. A secondary acoustic element is used to change the size of the acoustic aperture.

Up to a certain increase in aperture size, a simple horn, like in a trumpet, sufficiently increases the aperture but still emits a planar wave. For larger apertures, the difference in length between the the path from the driver to the center of the aperture and the path from driver to the outer region of the aperture becomes significant. Sound traveling to the center of the aperture arrives earlier than sound

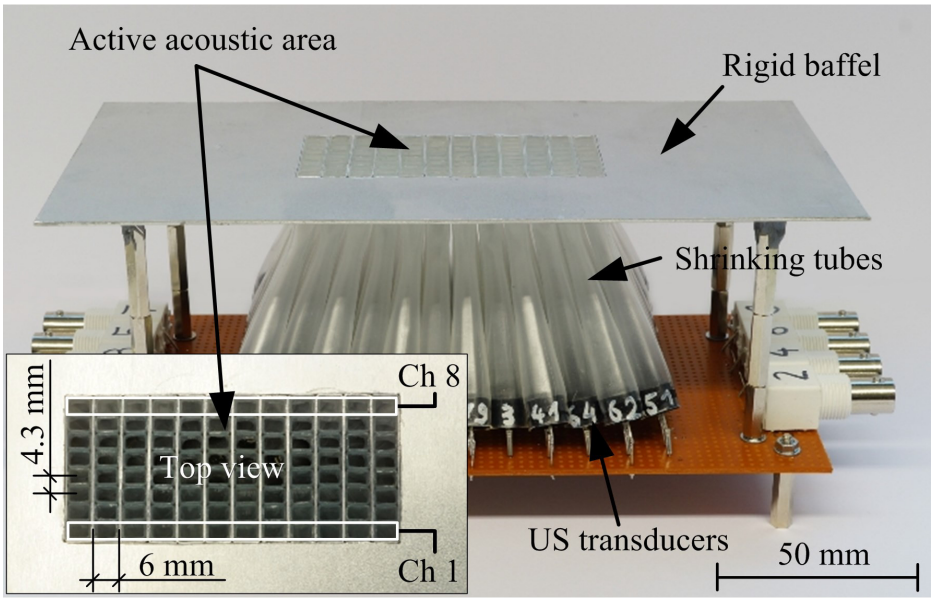

Figure 1.2.: Phased array transducer by Unger et. al. consisting of a matrix of 8×12 transducers that are combined in rows of 12 to form a line array of 8 elements. Heat shrinking tubes connect the individual transducer apertures to the active acoustic area in a rigid baffle [14].

traveling to the edge of the aperture. Both parts do no longer superimpose to a planar wavefront and thus no directional audio playback is achieved.

Specially designed waveguides incorporate obstacles, thus ensuring the sound travels a similar distance along the outer wall and to the center of the aperture. Various designs are already commercially available including continuous obstacles (Figure 1.3) [18], splitting and merging the soundbeam using channels [Figure 1.4 (a)] [19] [20], or using a large number of obstacles forming many sound paths [Figure 1.4 (b)] [21]. Using multiple speakers in a line array [22] further increases the aperture and

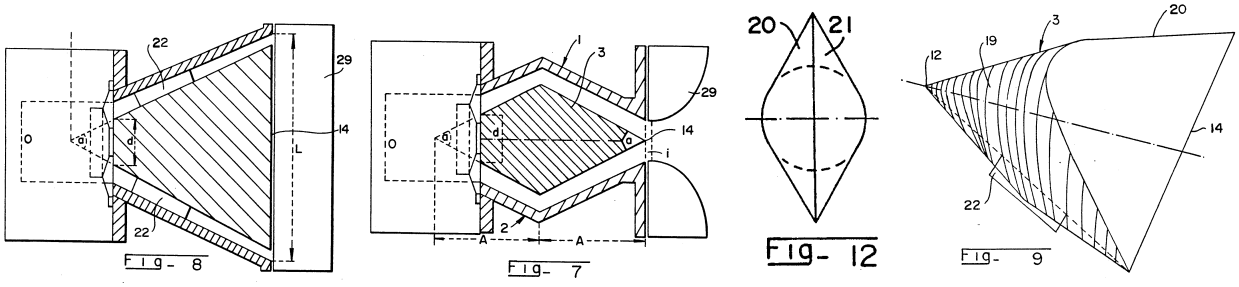

(a) (b) (c) (d)

Figure 1.3.: Obstacle in compression chamber of a line speaker. The maximum of the diameter of the obstacle is in the center and decreases towards the edges. (a) Section view parallel to aperture axis. (b) Section view perpendicular to aperture axis. (c) Front view on obstacle parallel to driver axis. (d) 3D-view of obstacle [18].

thus the directivity of a speaker system. One more noteworthy related concept is an acoustic lens. Here, a material with a similar but not equal speed of sound compared to the surrounding material is shaped with either a concave or convex surface. The sound waves refract on the material interface according to Snell's law, equivalent to an optical lens [24]. Possible materials are foams that are made up to a large portion of air or balloons filled with other gases of lower or higher density than the surrounding air.

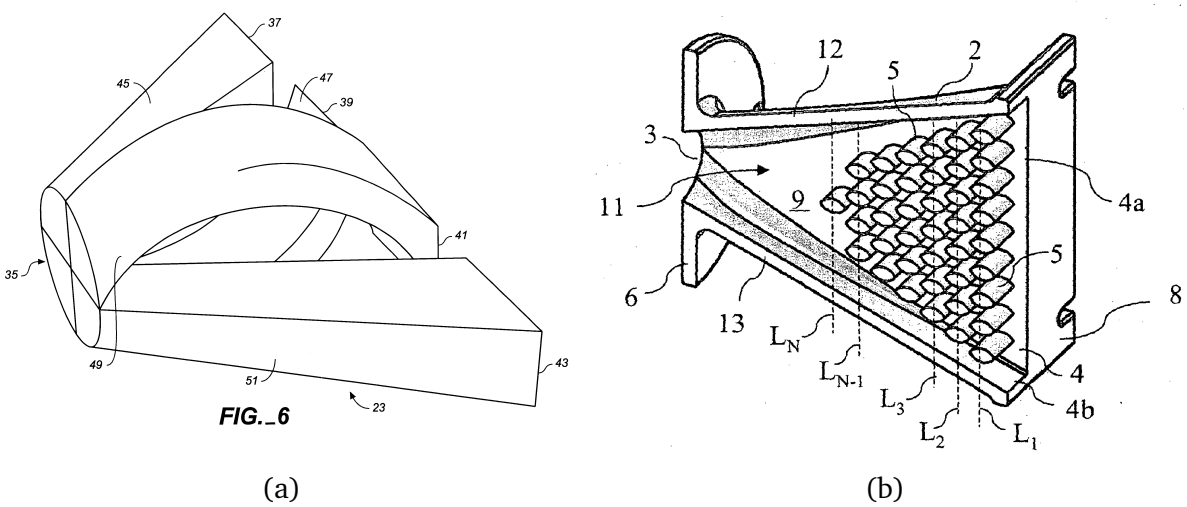

Figure 1.4.: Waveguide designs providing a planar wavefront by delaying the center sound path using four discrete sound paths (a) [19] or a large number of obstacles similar to a bean machine or a Galton Board (b) [21, 23].

The concept of partitioning the acoustic aperture into four discrete sections, each resulting in a channel of the same length and ultimately combining them to a new aperture [Figure 1.4 (a)] is already very similar to the array design by Unger et. al [14, 15, 16]. However, as the design is only a one-dimensional line array, the geometry can be sufficiently well separated into two halfs and each half can be manufactured using injection molding. Building a waveguide suitable for a two-dimensional array requires complex tooling or the assembly from several different parts.

In this thesis, 3D-printing is used as the advent of 3D-printing resulted in a number of experiments where 3D-printed parts are used to influence air-coupled ultrasound. Gurato et al. [25] used a 3D-printed bowl that covers the vibrating surface of an ultrasound tranducer, leaving only a small hole uncovered and, thus, effectively reducing the aperture. The result is a broader beam width compared to the raw transducer.

Beside changing the aperture, a number of groups published 3D-printed phase-changing devices. These consist of an arrangement of modular blocks containing channels of different lengths. The blocks are assembled according to a desired phase map and allow static phase shifts per module to accomplish acoustic holograms [26, 27] or the necessary phase distribution for single side acoustic levitation [28]. As the sound passes the blocks, each module causes a different phase shift resulting in an effect similar to a phased array but using only one sound source. However, if a different phase distribution is needed, the setup has to be reassembled using a different set of phase-changing blocks.

1.1 Original work and contributions

In the author's opinion the main contributions carried out through this thesis are:

1. The use of a 3D-printed waveguide for shrinking the aperture of a transducer array down to $\lambda/2$. This approach allows the building of a fully populated, 2D-array compared to the state of the art that only demonstrates 1D-arrays [12, 14, 15, 16]. Two different geometrical models are developed, fabricated and characterized. The first design resembles the approach of previous work,

however using a new fabrication method. The second design uses channels of different length to allow easier fabrication and the potential use of transducer arrays build on top of planar substrates.

2. The design of electronics for ultrasound arrays in the frequency range up to 200 kHz for sending and receiving for up to 64 channels. This makes experiments using the waveguides possible in the first place as the sheer number of laboratory equipment needed otherwise is impractical.

3. The demonstration of a gas flow meter utilizing this array that compensates the sound drift effect, and, thus, allows gas flow metering at higher flow velocities.

4. Exposing of reflecting features in an anechoic chamber that potentially limit the overall acoustic absorption.

5. The visualization of a steerable air-coupled ultrasound beam using the the Schlieren imaging method. This method is well established for visualizing ultrasound waves in water. However, as the effect is far weaker in air, only high sound pressures change the refractive index of air enough for visible image. The presented array is capable of producing sound pressures of the necessary magnitude, thus, capturing of the soundbeam using Schlieren imaging could be demonstrated.

1.2 Structure of this thesis

This thesis starts with a background chapter, explaining the fundamental effects and relationships in phased array systems. No background in communication technology is required, although most of the formulas are directly taken from antenna theory. Visual and geometric illustrations are included whenever possible. The calculation of sound fields using the Rayleigh integral is explained. The chapter closes with an overview of available air-coupled ultrasound devices suitable for a phased array and how to include these into the calculation methods stated before.

The next two chapter describe the system design. The system consists of three parts, the waveguide including the transducers, the electronics and a signal processing application running on a personal computer (PC). The two waveguide designs are described by geometrical curves. This is necessary because a geometric model is necessary for 3D printing of the waveguides as well as the calculation of the channel lengths for the second design.

A chapter describing a comprehensive system characterization follows. Here, characteristic values for a datasheet of the complete system are obtained. Besides the measurement using a calibrated microphone, an alternate method that uses the optical imaging technique of Schlieren imaging is also used for the transmit characteristics.

The system is then tested in two real world applications: The first application is park distance control (PDC), where the system is used in a pulse echo configuration. On a parking lot, obstacles comparable to poles of traffic lights are placed in the field of view of the array and detected. The system is also compared to the implementation of a current premium car. The second application is gas flow metering where a pitch-catch configuration is used.

The last chapter concludes the thesis and gives an outlook about future work.

2 Background

This chapter summarizes the theoretical backgrounds required for understanding phased array systems and ultrasound fields in air. Starting with a general introduction to phased array systems independent of ultrasound but by physics-based reasoning. The basic operating modes of steering and focusing are explained and the distinction between the near and far field is explained. The influence of the array geometry on the resulting sound field is discussed and the terms *side lobes* and *grating lobes* are introduced. The importance of the $\lambda/2$-spacing between the individual transducers is shown.

After introducing the key aspects, a more formal introduction to the calculation of sound fields using the Rayleigh-Integral is given. A number of special solutions for the Rayleigh-Integral are introduced as well as one approach of numerically solving arbitrary acoustic apertures.

From the Rayleigh-Integral, the fundamental finding is derived that the far field of any acoustic aperture is simply calculated from the 2D-Fourier transform of the aperture geometry. This finding turns out to be useful to prove a number of formulas previously given. These are the piston transducer equation, the $\lambda/2$- spacing and the occurrence of grating lobes. These findings are then used to explain the pattern multiplication theorem that states that the far field of any array of real transducers can be calculated by multiplying the far field of an ideal array and the far field of single transducer.

2.1 Conventions and Terms

The vibrating surface or membrane of any ultrasound system is called the *aperture*. All ultrasound systems described in this thesis, including all examples and all phased arrays, have a flat aperture, i.e. the aperture is contained in a plane. This aperture plane is always oriented in the xy-plane of a Cartesian coordinate system. The aperture is always centered around the origin and is facing in positive z-direction [Figure 2.1 (a)].

Angles are either measured in spherical coordinates (r, φ, ϑ) [Figure 2.1 (b)] or using the azimuth/elevation system (r, AZ, EL) consisting of also of distance to the origin r, a horizontal angle (azimuth, AZ) and a vertical angle (elevation, EL) [Figure 2.1 (c)].

The transformation from spherical to Cartesian coordinates is given by

$$x = r \cdot \sin(\vartheta) \cdot \cos(\varphi); \tag{2.1}$$
$$y = r \cdot \sin(\vartheta) \cdot \sin(\varphi); \tag{2.2}$$
$$z = r \cdot \cos(\vartheta). \tag{2.3}$$

When a reduction to a 2D-coordinate system is done, the system is shown in the xz-plane. The spherical coordinates reduce to polar coordinates ($\varphi = 0$), i.e.

$$x = r \cdot \sin(\vartheta); \tag{2.4}$$
$$z = r \cdot \cos(\vartheta). \tag{2.5}$$

The transformation from spherical to the (AZ, EL, r) system is given by

$$x = r \cdot \cos(EL) \cdot \sin(AZ); \tag{2.6}$$
$$y = r \cdot \sin(EL); \tag{2.7}$$
$$z = r \cdot \cos(EL) \cdot \cos(AZ). \tag{2.8}$$

Both non Cartesian coordinate systems are useful in their own specific use case: The spherical coordinate system reduces to a two dimensional system when an axial symmetric transducer is described, i.e. the situation is independent of φ. The AZ/EL-system resembles more the natural movement of the human head: An observer standing in the origin will move his head sideways, i.e. in AZ-direction, or up and down, i.e in EL-direction. Rotating the head around the z-axis, i.e. the φ-axis feels unnatural as the field of view is not changed but only rotated.

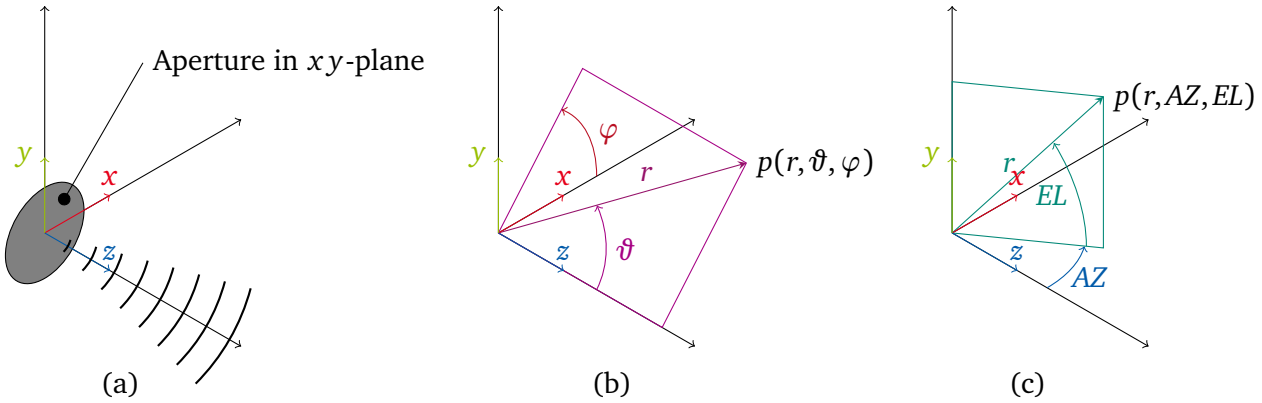

Figure 2.1.: Coordinate system used in this thesis. Transducers are generally oriented in the xy-plane facing and radiating in z-direction. Two other coordinate systems complement the description of positions in space: Spherical coordinates describe a point by the distance to the origin r and the two angles φ and ϑ (b). The EL/AZ-system uses the two angles AZ and EL as well as r (c).

Whenever plots show a field quantity in false colors, uniform perception color maps are used. The two color maps of choice are *viridis* [29] for non symmetric quantities and a blue-gray-red colormap for symmetric quantities [30] (Figure 2.2). The same blue and red colorscheme is used in schematic drawings of wave phenomena where red is a positive elongation, i.e. a peak, and blue is a negative elongation, i.e. a trough.

Figure 2.2.: Uniform perceptional colormaps viridis (a) and symmetric colormap (b). These color maps take into account the brightness perception of the human eye, and, thus, are recognized as a constant brightness gradient.

2.2 Introduction to phased array systems

According to Huygens's principle, every point on a wave front acts as a source of a spherical wavelet. This also means that a wavefront can be described as an infinite sum of spherical wavelets. A phased array is a technical implementation of this principle that uses only a finite number of wave sources to synthesize a wave front. In this thesis, these individual wave sources are designated as *transducers* because this is the term used in ultrasonic engineering. The explanation, however, is valid for other kinds of wave sources such as antennas or speakers. The wavefront is composed of the interference of spherical waves emitted by the individual transducers. The final wavefront is dependent on the excitation signals of the individual transducers and can be altered by changing those excitation signals.

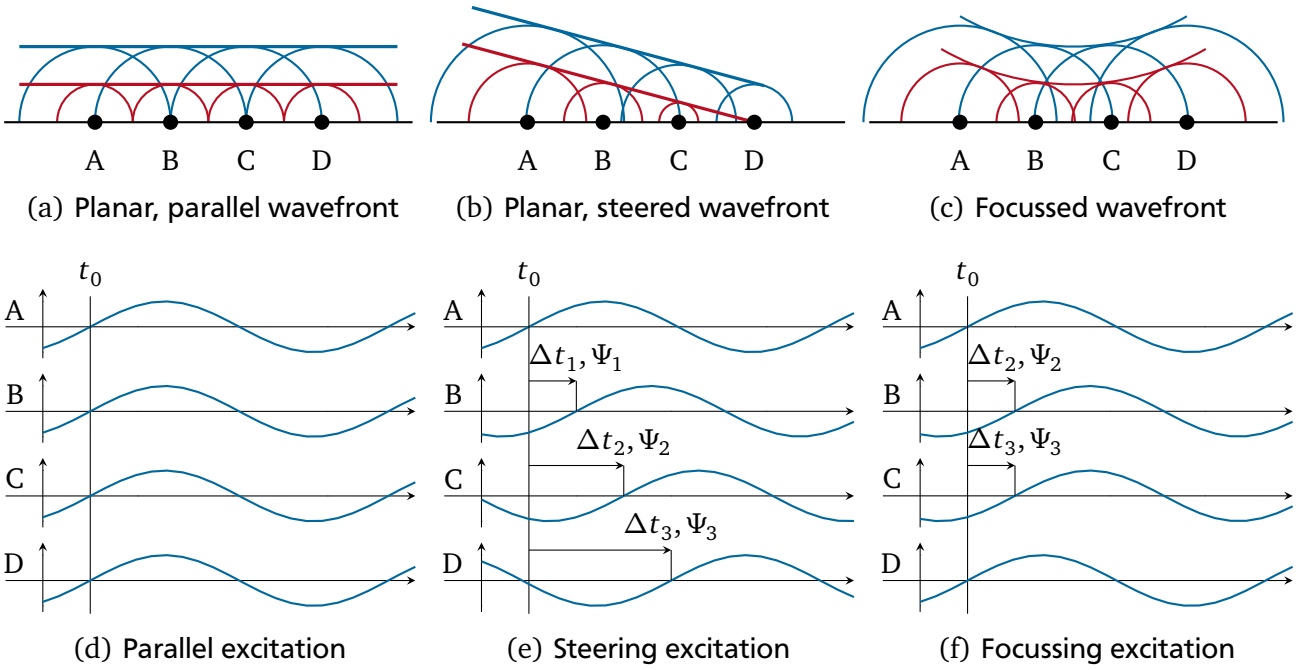

(a) Planar, parallel wavefront (b) Planar, steered wavefront (c) Focussed wavefront

(d) Parallel excitation (e) Steering excitation (f) Focussing excitation

Figure 2.3.: Steering and focusing in a phased array system. 4 elements (A-D) are excited using different signal combinations (d-f) resulting in different waveforms (a-c). Each elements emits spherical wavelets consisting of peaks (read) and troughs (blue) that superimpose to a planar wavefront (a) and (b) or to a focusing wavefront (c). The shift of the individual excitation signals is either described by a time delay Δt_k or a phase shift Ψ_k.

Consider three examples of excitation signals for an array consisting of four transducers (*A* - *D*) placed along a line (Figure 2.3). When all transducers are excited by the same signal, a planar wavefront parallel to the array is emitted [Figure 2.3 (a) and (d)]. When the signals are linearly delayed, a planar wavefront that is tilted with respect to the array is emitted [Figure 2.3 (b) and (e)]. When the signals are delayed so the wavelets meet up at a certain point in front of the aperture, the energy is intensified at that certain position, the so called focus point [Figure 2.3 (c) and (f)]. It is necessary that all the excitation signals are coherent, i.e. generated from a common time base, otherwise the individual excitation signals drift apart and the phase between the signals changes constantly.

These are examples of using a phased array as a sender. A phased array also works as a receiver when the transducers are used as receivers. The same three cases can be distinguished: If a planar wavefront that is parallel to the transducers hits the array, identical signals are received. If a wavefront tilted with respect to the array hits the array, the individual received signals are delayed linearly. If a spherical

wavefront hits the array, the signals are delayed non linearly. The source of the spherical wave can be located by investigating the individual delays.

2.3 Near field, natural focus and far field

The sound field relative to any ultrasound transducer is described by a function of pressure for any given point in space, either $p(x,y,z)$, $p(r,\vartheta,\varphi)$ or $p(r,AZ,EL)$. For every transducer or array of transducers, there is a certain distance N which makes several simplifications in the calculations valid. This distance N, the *natural focus* is given by [31, p. 160]

$$N = \frac{R_t^2}{\lambda}, \tag{2.9}$$

where R_t is the radius of a circular transducer. The region between the transducer surface and the natural focus is called the *near field* wheras the region beyond the natural focus is called the *far field* (Figure 2.4). In the far field, $p(r,\vartheta,\varphi)$ can be separated into a function of the distance $f(r)$ and a function of the two angles $f(\vartheta,\varphi)$. In this thesis, this function is called the *radiation pattern*. When the radiation pattern is given as a dimensionless function, it is designated as $E(\vartheta,\varphi)$.

It is important to distinguish between operating a phased array system in either the near or far field. Several simplification are only valid in the far field and when designing an array for either operating distance, mutually contradictory design rules apply.

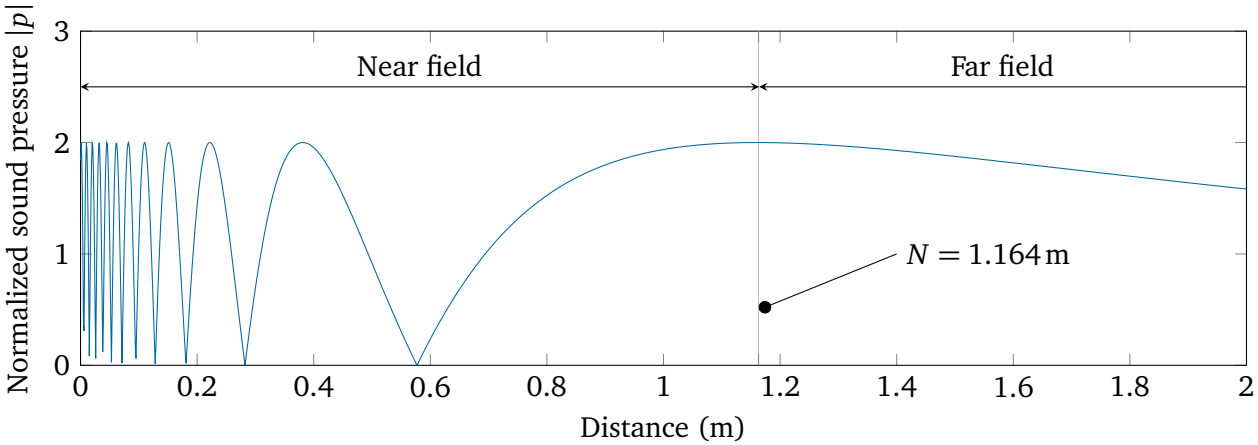

Figure 2.4.: Sound pressure along the z-axis of a circular vibrating surface with a diameter of $2R_t = \varnothing 200\,\text{mm}$, $f = 40\,\text{kHz}$. The sound pressure oscillates in the near field between zero and two times the surface sound pressure due to constructive and destructive interference. Beyond the natural focus which is the farthest maximum, the amplitude decreases monotonically.

2.4 Influence of the inter element spacing and the occurrence of grating lobes

It is obvious that the synthesized wavefront will not be ideal because of the finite number of elements. It is further likely that the more elements are used and the closer they are together, the better the synthesized wavefront will approximate the desired wavefront. However, the more elements are used, the more resources are needed for a technical realization. Understanding the relationship between the number of elements and their spacing on the resulting sound field enables the design of an optimized array that meets a technical specification utilizing only a minimal amount of resources. First, the effect of the inter-element spacing d is discussed since lowering this distance is one fundamental basis of this thesis.

An array made up of the minimum number of two elements is considered. In this example, no steering is done, i.e. both transducers are excited by the same signal. Constructive interference, where peaks meet peaks and troughs meet troughs, occurs at all positions where the difference in distance (Δs) to the two elements fulfills

$$\Delta s = i\lambda, i \in \mathbb{Z}, \tag{2.10}$$

where λ is the wavelength and i is an integer.

Mathematical background

A mathematical primitive that is useful for modeling this set of positions is the *hyperbola* [32, p. 207]. It is defined by all points P that have a constant difference in distance $2a$ to two focal points F_1 and F_2, i.e.

$$H = \{P \mid ||PF_2| - |PF_1|| = 2a\}. \tag{2.11}$$

This is a system of two degrees of freedom: The already known difference in distance $2a$ and the distance $2e$ between F_2 and F_1. For any e, there is an infinite number of hyperbolas as long as

$$0 < a < e \tag{2.12}$$

is fulfilled [Figure 2.5 (a) and (b)]. The two corner cases $a = 0$ and $a = e$ are of special interest: The first case, $a = 0$, means that there is no difference in distance at all, i.e. the distance from any point P on that curve to F_1 is equal to the distance from P to F_2. The two branches to the left and to the right collapse to a vertical line. For the second case of $a = e$, every point on the horizontal axis outside of F_1 and F_2 fulfills Equation 2.11. Geometrically speaking, the left and right branches of the hyperbola both collapse to a horizontal line.

There is a third parameter b that is connected to a and e by

$$e^2 = a^2 + b^2. \tag{2.13}$$

This variable b is needed for some parameterizations of the hyperbola and its asymptotes that are given by line of slope b/a [Figure 2.5 (c)]. These will be useful later on.

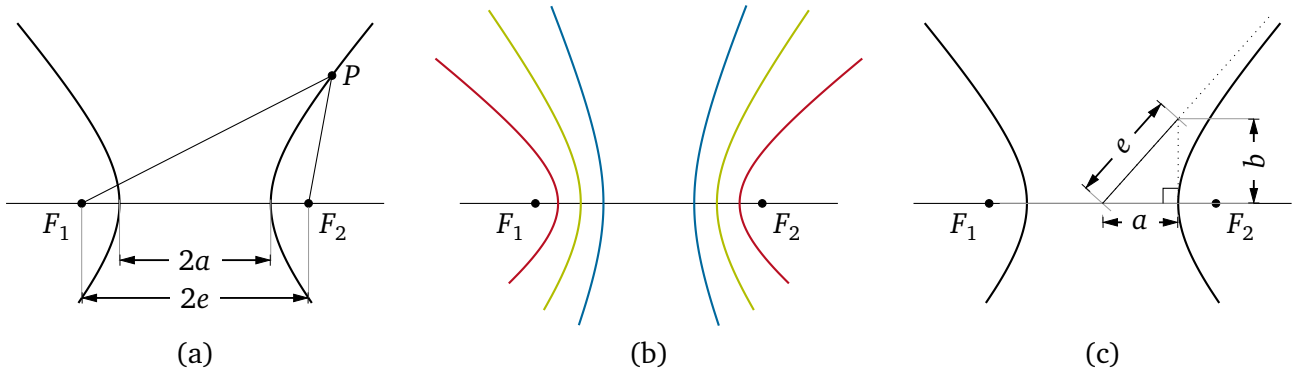

Figure 2.5.: A hyperbola is defined as the set of all points that have a constant difference in distance of $2a$ to two focal points F_1 and F_2. The distance between the focal points is designated as $2e$ (a). For any two focal points, an infinite number of hyperbolas exist as $2a$ can be chosen freely as long as $a < e$. (b) shows three examples for $a = 0.4 \cdot e$ (blue), $a = 0.6 \cdot e$ (green) and $a = 0.8 \cdot e$ (red) for a fixed e. The hyperbola has an asymptote that is a line passing the origin of slope b/a (c).

Adopting the hyperbola as locus for constructive interference

Transfered to the problem of describing constructive interference, the positions of the two focal points F_1 and F_2 are the positions of the two array elements, i.e. $2e$ is the distance between the two transducers d. The second parameter $2a$ is Δs as in Equation 2.10. Solutions of this system are the locations of constructive interference.

If there are solutions beside the special case of $a = 0$, the array is radiating into additional directions next to the desired positive z-direction at full amplitude. In the radiation pattern, additional lobes next to the desired main lobe become visible. These additional lobes are called *grating lobes*. This is unwanted behavior because the energy is not only distributed over all lobes, but also sending and receiving becomes ambiguous between the main lobe and all grating lobes.

For the corner case of $d = \lambda$, i.e $e = a$, the hyperbola describing the areas of constructive interference are collapsed to the x-axis. Two grating lobes pointing in positive and negative x-direction are present. When separating the transducers further apart, i.e. $d > \lambda$, the previously collapsed branches of the hyperbola separate and the grating lobes move closer to the main lobe (Figure 2.6). Increasing d even further leads to additional grating lobes. The reason for this behavior is because the larger the distance d between the transducers become, the more solutions to Equation 2.10 exist.

The angles of the grating lobes are calculated by obtaining all possible a that fulfill both Equation 2.12 and Equation 2.10. Grating lobes occur for all $a \neq 0$ whereas $a = 0$ is the solution corresponding to the main lobe. The angle of the grating lobe with respect to the main lobe is calculated using the slope of the hyperbola, i.e. $\vartheta_g = \operatorname{atan}(a/b)$. For the example of $d = 3/2 \cdot \lambda$, where $e = 3/4 \cdot \lambda$, $a = \lambda/2$ and $b = \sqrt{5}/4 \cdot \lambda$ the angle of the grating lobe is $\vartheta_g = \operatorname{atan}(a/b) = 41.76°$. In conclusion, the distance between adjacent transducers d must be smaller than the wavelength in order to obtain a grating lobe free radiation pattern.

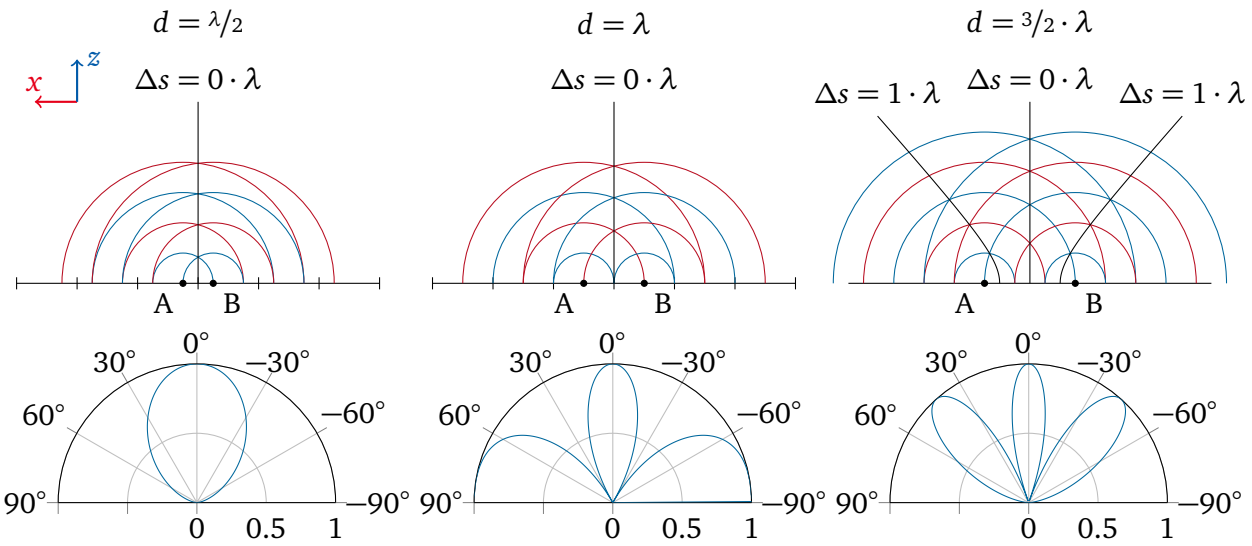

Figure 2.6.: Examples of two point sources located at the three distinct distances $d = \lambda/2$, $d = \lambda$ and $d = 3/2 \cdot \lambda$. Top: Interference of spherical wavelet where red is a peak and blue is a trough. Bottom: radiation pattern. For $d = \lambda/2$, constructive interference occurs only in z-direction where peak and peak (red) as well as trough and trough (blue) meet. For $d = \lambda$, additional grating lobes occur in positive and negative x-direction of the array. For $d = 3/2 \cdot \lambda$, the grating lobes move closer to the main lobe and occur at an angle of 41.76°.

Steering and Grating lobe free area

When steering on the phased array is active and, thus, the excitation signals of the two sources are phase shifted, the condition for a grating lobe free radiation pattern becomes more strict. The time delay between the emission of the wavelets for any given position is no longer fixed. It rather becomes a range of possible time delays depending on the minimum and maximum steering angles. For the worst case of steering to ±90°, an additional path difference of d is added. For Equation 2.12 to stay unambiguous, the transducers need to be spaced $\lambda/2$ apart. This criteria becomes less strict when the steering angle is restricted to maximum steering angle of $\vartheta_{\max}$. The inter element spacing becomes a function of $\vartheta_{\max}$ [33], i.e.

$$d \leq \frac{\lambda}{1 + \sin(\vartheta_{\max})}. \tag{2.14}$$

2.5 Influence of the number of elements

As seen in the radiation pattern in the previous example of two transducers spaced $d = \lambda/2$ apart (Figure 2.6), the main lobe is not a sharp beam pointing in z-direction but has a significant width. In fact, the first null bandwidth (FNBW) of this configuration is 180° meaning that the radiating pattern only reaches zero for $\vartheta = \pm 90°$. At this angle, destructive interference occurs, i.e. the amplitudes of both spherical wavelets sum to zero. Similar to constructive interference (Equation 2.10), this happens when

$$\Delta s = (n + 1/2) \cdot \lambda, n \in \mathbb{Z} \tag{2.15}$$

is fulfilled. However, when more than two transducers are involved, there are multiple possibilities on how the individual wavelets sum to zero. Consider an example of an array consisting of $n = 8$ elements spaced $d = \lambda/2$ apart. The radiation pattern shows the main lobe surrounded by three smaller side

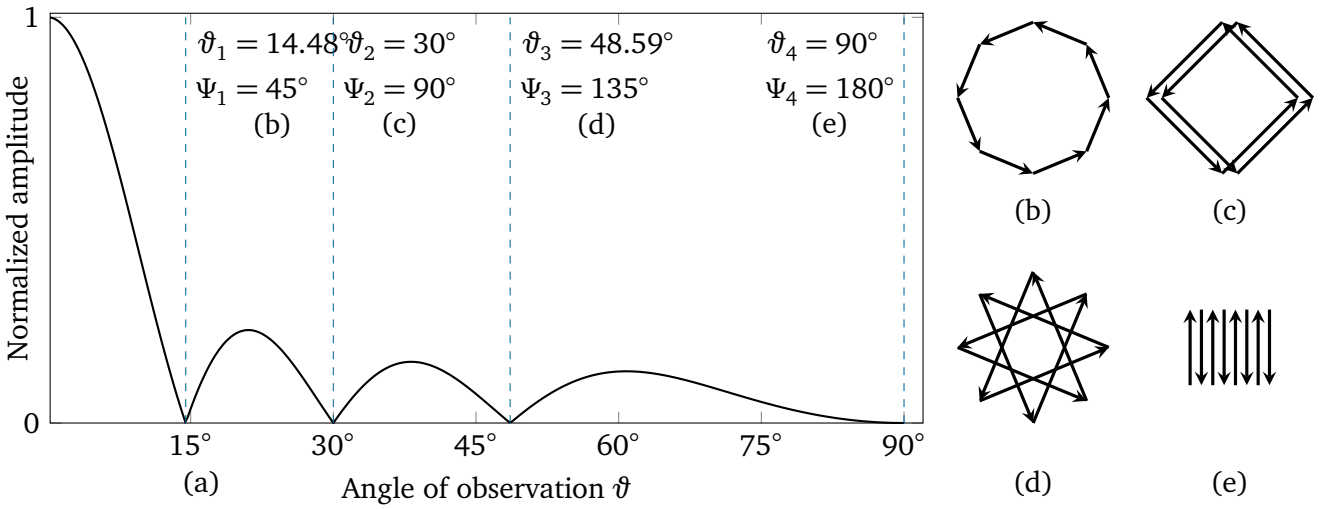

Figure 2.7.: Radiation pattern for an 8 element $\lambda/2$ array (a) and vector diagrams for each minimum (b-e).

lobes [Figure 2.7 (a)]. Between either lobe, destructive interference happens. For each minimum, the corresponding interference situation is shown as vector diagram. At the first minimum at $\vartheta_1 = 14.48°$, the phase shift between the wavelets is $\Psi_1 = 45°$. All eight phases sum up to $n \cdot \Psi = 8 \cdot 45° = 360°$ and all eight participating amplitudes sum up to zero [Figure 2.7 (b)]. At the second minimum at $\vartheta_2 = 30°$, the sum of phase shifts is $8 \cdot 90° = 720°$ which again results in an amplitude of zero [Figure 2.7 (c)]. The same principle also applies for the two remaining minima at $\vartheta_3 = 48.59°$ and $\vartheta_4 = 90°$. The phase shifts for which destructive interference occur are given by

$$\Psi_i = \frac{360°}{n} \cdot i, \tag{2.16}$$

where i is the index of the i-th minimum.

In conclusion, increasing the number of elements results in a narrower main lobe. The reason is because the more elements are present, the earlier all phase shifts sum up to a multiple of 360° and thus the earlier all amplitudes sum up to zero.

The complete radiation pattern of this example consists of one main lobe surrounded by three side lobes on either side resulting in a total of seven lobes. Generalized, the number of lobes including main and side lobes is $n-1$ where n is the number of transducers. Changing the number of elements, while keeping the inter-element distance constant, does not change the occurrence or positions of grating lobes (Figure 2.8)

For regular line array where all n elements are equally spaced d apart, there is a closed form solution for obtaining radiation patterns [31],

$$p(\vartheta) = \frac{\sin\left[n\pi\left(\frac{d}{\lambda}\right)\sin(\vartheta)\right]}{\sin[\pi\left(\frac{d}{\lambda}\right)\sin(\vartheta)].} \tag{2.17}$$

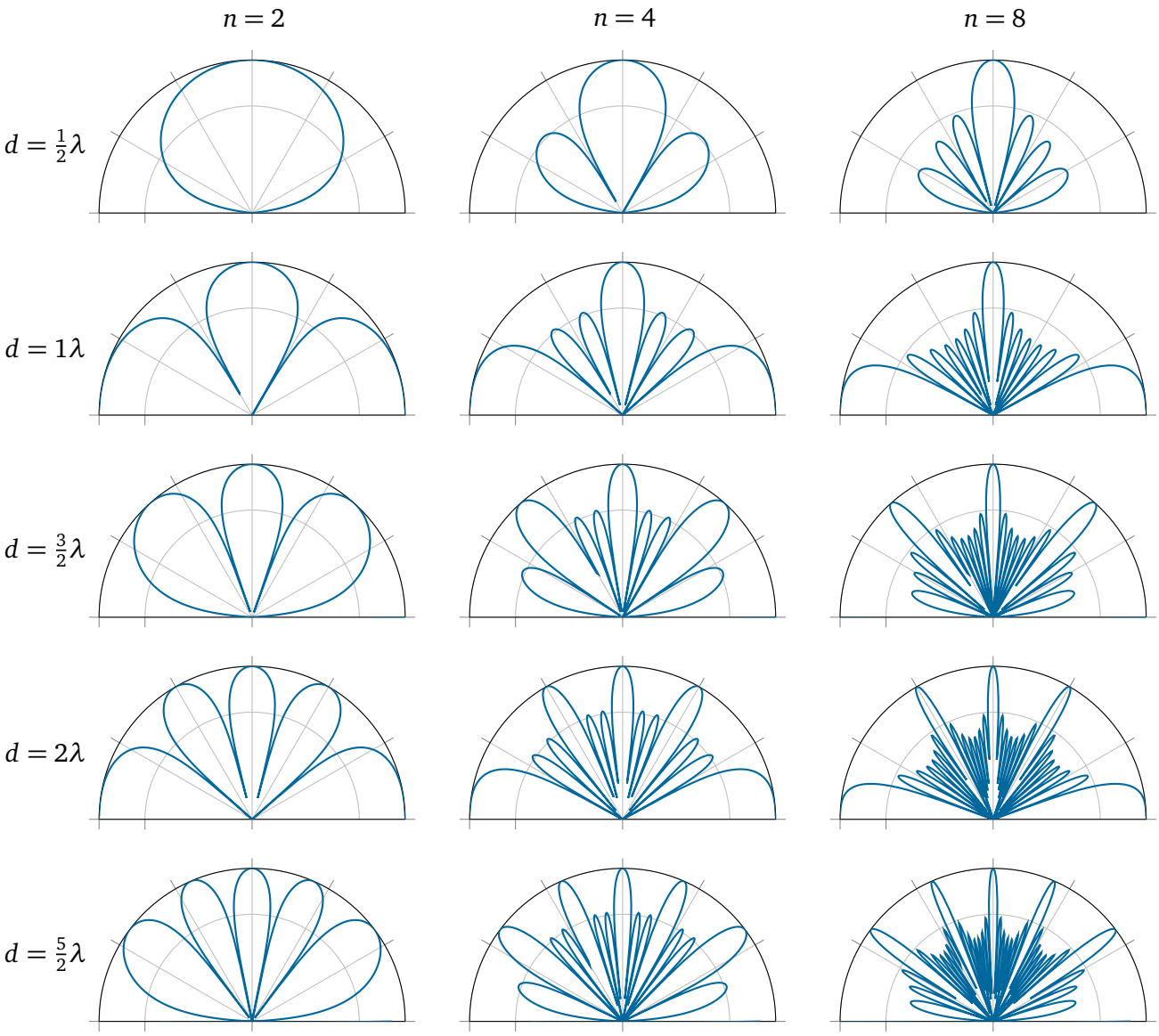

Figure 2.8.: Radiation patterns for different number of elements n and pitch d. More elements result in a narrower main lobe due to the increased size of the aperture, however the positions of grating lobes is constant for a given d. Both the main lobes and the grating lobes are surrounded by $n-1$ side lobes. With increasing d, existing grating lobes move closer to the main lobe and more grating lobes appear.

2.6 Calculation of sound fields

In order to apply these phased array fundamentals to ultrasound fields, a brief introduction to acoustics is given. An acoustic wave is a mechanical wave that interchanges between pressure p and particle velocity in x,y and z directions. The according wave equation [34] is given by

$$\frac{\partial^2 p}{\partial x^2} + \frac{\partial^2 p}{\partial y^2} + \frac{\partial^2 p}{\partial z^2} = \frac{1}{c^2}\frac{\partial^2 p}{\partial t^2} \tag{2.18}$$

For the special case of a flat sound source embedded in an infinite wall, the so called *rigid baffle*, the resulting sound pressure for any point $p(x,y,z)$ is calculated by the *Rayleigh-Integral*, i.e.

$$p(x,y,z) = \frac{j\omega\rho}{2\pi}\int_{-\infty}^{\infty}\int_{-\infty}^{\infty} v(x_q,y_q)\frac{e^{-jkR}}{R}\mathrm{d}x_q\mathrm{d}y_q \tag{2.19}$$

Here, $v(x_q,y_q)$ is the velocity distribution on the transducer surface, ρ is the density of air, $k = \omega/c$ is the wave number and $R = \sqrt{(x-x_q)^2+(y-y_q)^2+z^2}$ is the distance to the point on the vibrating surface (Figure 2.9).

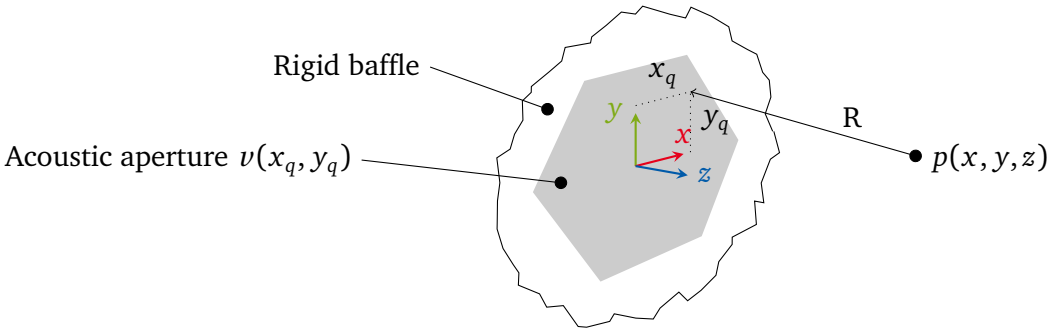

Figure 2.9.: Variables involved in the calculation of a sound field in front of a transducer using the Rayleigh-integral (Equation 2.19). A hexagon shaped transducer as example is mounted in an infinite rigid baffle. The sound pressure p for any particular position (x,y,z) is obtained by integrating over the acoustic aperture of the transducer in respect to that position.

There is no general closed form solution of the Rayleigh-integral. The fundamental problem is the term $\int \frac{e^{-jkR}}{R}\mathrm{d}R$ also known as *exponential integral*. Besides having no closed form solution, the integrand becomes singular at $R = 0$, meaning that the Rayleigh integral cannot compute the sound pressure directly on the surface. However, for a number of special cases, analytical solutions exist:

Point source

When the transducer aperture is shrinked to a single point, the integral simplifies to

$$p(x,y,z) = \frac{j\omega\rho}{2\pi}A_0 v_0 \frac{e^{-jkr}}{r} \tag{2.20}$$

where v_0 is a velocity and A_0 is an artificial area $\neq 0$. The resulting sound field is only a function of r and, thus, has a constant radiation pattern. A pulsating sphere as a technical implementation of a point source generates such a sound field, however, only outside of its finite radius.

Piston transducer along the z-axis

A common case in acoustics is the *piston transducer* [34, p. 117] consisting of a circular shaped aperture with a radius R_t and a constant velocity v_0, i.e.

$$v_p(x_q, y_q) = \mathrm{circ}(R_t) = \begin{cases} v_0 & \text{for} \sqrt{x_q^2 + y_q^2} < R_p \\ 0 & \text{for} \sqrt{x_q^2 + y_q^2} \geq R_p. \end{cases} \tag{2.21}$$

This situation is radial symmetric in respect to the z-axis and a closed solution for the sound pressure is given by

$$p(z) = \rho c v_0 e^{-jkz} \left(1 - e^{-jk\left(\sqrt{R_p^2 + z^2} - z\right)} \right). \tag{2.22}$$

Although this equation is also valid for the near field, the result starts to oscillate when approaching the origin.

Far field of the piston transducer

There is also a closed form solution for the radiation diagram of the piston transducer [31, p. 158] given by

$$p(r, \vartheta) = j\rho c k v_0 R_t^2 \frac{e^{-jkr}}{r} \frac{J_1(kR_t \sin\vartheta)}{kR_t \sin\vartheta}, \tag{2.23}$$

where J_1 is the *Bessel function* of the first kind and first order. Like all radiation patterns, this expression is only valid in the far field. For small diameters compared to λ, there is almost no directivity. This is consistent with the previous solution of a point source. With increasing radii, directivity increases and becomes significant for radii of 0.25λ and beyond (Figure 2.10). One way for deriving this formula is later explained in detail in section 2.7.

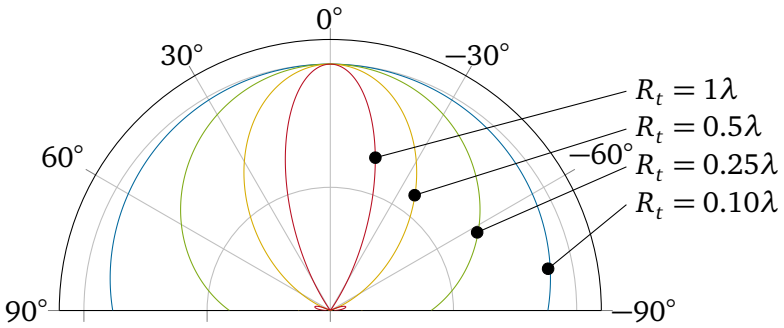

Figure 2.10.: Radiation pattern of piston transducers of different diameters. Significant directivity occurs for diameters of about λ and larger.

Far field using the Fourier transform

The radiation patterns of arbitrary velocity distributions $v(x_q, y_q)$ can be calculated by using the Fourier transform of the vibrating aperture. This method gives far field solutions for various aperture geometries, the circular piston being one of them. This technique is explained in detail in section 2.7. For other cases numeric calculation techniques are used. One approach is explained in section 2.8

2.7 Far field approximation using the Fourier transform

As already statet, the fundamental problem of solving the Rayleigh-Integral (Equation 2.19) is the term $\int \frac{e^{-jkR}}{R} \mathrm{d}R$ where R is the distance to a specific point of the vibrating surface v. For large distances R compared to the dimensions of the vibrating area $v(x, y)$, R can be sufficiently approximated by the distance to the origin r. This factor e^r/r can be moved out of the integral [34, p. 112]. The result expressed in spherical coordinates becomes

$$p(r, \vartheta, \varphi) = \underbrace{\frac{j\omega\rho}{2\pi r} e^{-jkr}}_{f(r)} \underbrace{\int_{-\infty}^{\infty} \int_{-\infty}^{\infty} v(x_q, y_q) \exp\left[-jk(x_q \sin\vartheta \cos\varphi + y_q \sin\vartheta \sin\varphi)\right] \mathrm{d}x_q \mathrm{d}y_q}_{f(\vartheta,\varphi)}. \tag{2.24}$$

This expression already is separated into a function of r and a function of ϑ and φ. Compared to the definition of the 2D Fourier transform

$$F(u, v) = \int_{-\infty}^{\infty} \int_{-\infty}^{\infty} f(x, y) e^{-j2\pi(ux+vy)} \mathrm{d}x \mathrm{d}y, \tag{2.25}$$

we see similarities and can map the parts of both equations (Table 2.1). The conclusion is that the

Table 2.1.: Corresponding parts of Equation 2.24 and Equation 2.25.

Far field estimation (Equation 2.24)	2D fourier transform (Equation 2.25)
$v(x_q, y_q)$	$f(x, y)$
$1/\lambda \sin\vartheta \cos\varphi$	u
$1/\lambda \sin\vartheta \sin\varphi$	v

far field of any vibrating surface even with arbitrary velocity distribution $v(x_q, y_q)$ is calculated by the Fourier transform of $v(x_q, y_q)$. Another conclusion is that besides spherical or *AZ-EL*-coordinates, there is another coordinate system, u/v-coordinates, for plotting radiation patterns. This coordinate system has the advantage that the minimas in a regular array are equally spaced in the radiation pattern and steering is a matter of a linear translation. Note that the visible field in u/v-space is a circle with radius 1, i.e. $\sqrt{u^2 + v^2} < 1$. Because k is dependent on λ, each far field estimation is of course only valid for a single wavelength.

The already presented example of the piston transducer has a circular shaped aperture of radius R_p, abbreviated as $\mathrm{circ}(R_p)$. The Fourier-Transform of a circle is given by

$$\int_{-\infty}^{\infty} \int_{-\infty}^{\infty} \mathrm{circ}(R_t) e^{-jk(ux+vy)} \mathrm{d}x_q \mathrm{d}y_q = \frac{J_1(kR_t u)}{kR_t u} = \frac{J_1(kR_t \sin(\vartheta)))}{kR_t \sin(\vartheta)} = \mathrm{jinc}(kR_t \sin(\vartheta)) \tag{2.26}$$

The term jinc is used because the structure is similar to the sinc-function. Inserting $\mathrm{circ}(R_p)$ into Equation 2.24 leads to the piston transducer equation (Equation 2.23).

A phased array consisting of ideal elements, i.e. elements of zero size and, thus, elements with perfect uniform radiation, is modeled as an arrangement of Dirac pulses on the aperture plane. Again, the minimal number of elements of $n = 2$ is used as an example. Assuming a pitch of $d = \lambda/2$, the velocity distribution is then given by

$$v(x) = \delta\left(x + \frac{\lambda}{4}\right) + \delta\left(x - \frac{\lambda}{4}\right). \tag{2.27}$$

The radiation pattern is then simply calculated by assembling the Fourier transform from the known solutions of the Dirac function and the shift theorem, i.e.

$$E(u) = \int_{-\infty}^{\infty} \delta\left(x + \frac{\lambda}{4}\right) + \delta\left(x - \frac{\lambda}{4}\right) \mathrm{d}x_q = e^{-jk\frac{\lambda}{4}u} + e^{jk\frac{\lambda}{4}u} = e^{-j\frac{\pi}{2}u} + e^{j\frac{\pi}{2}u} = 2\cos\left(\frac{\pi}{2}u\right), \tag{2.28}$$

or using $u = \sin(\vartheta)$, in polar coordinates,

$$E(\vartheta) = 2\cos\left(\frac{\pi}{2}\sin(\vartheta)\right). \tag{2.29}$$

Both $E(u)$ and $E(\vartheta)$ are periodic functions. Increasing d beyond $\lambda/2$ results in multiple copies of the main lobe in the visible region of $-1 \leq u \leq 1$ (Figure 2.11).

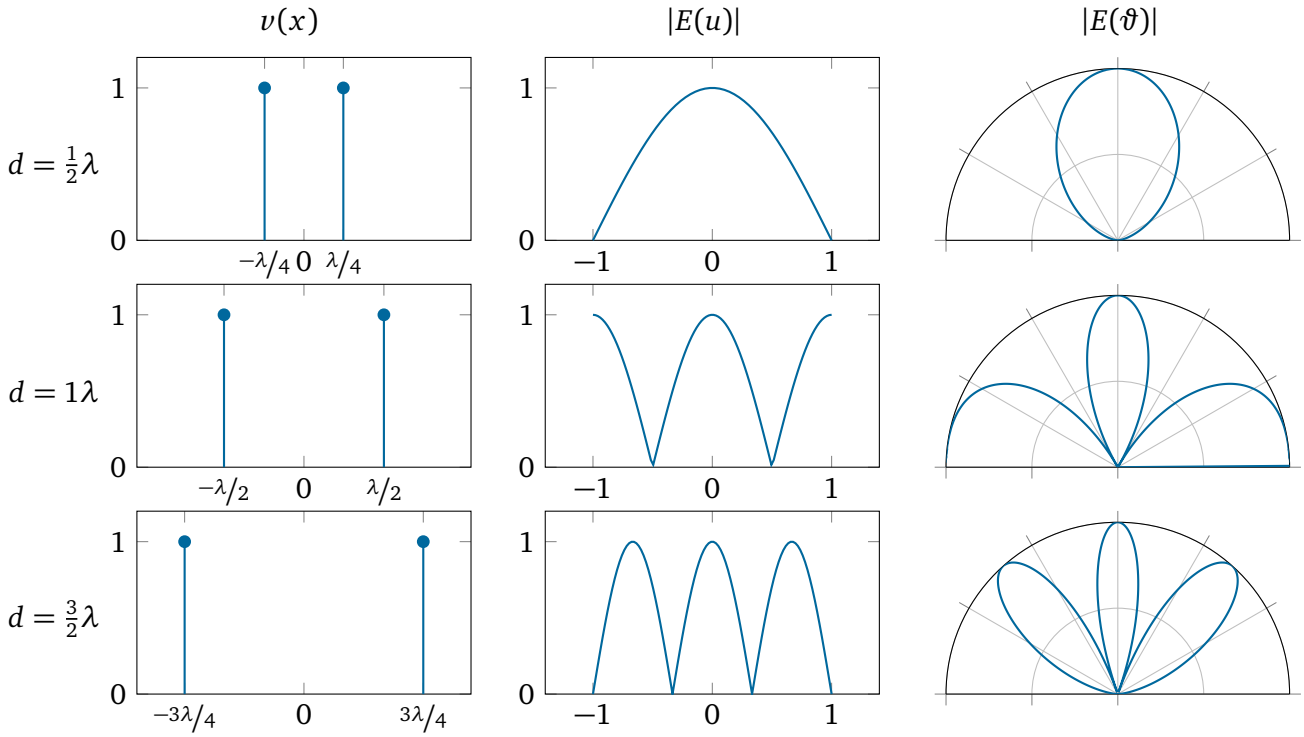

Figure 2.11.: Examples of line arrays consisting of $n = 2$ elements, radiation pattern in u-space and as polar plot. With increasing distance d between the two array elements, the radiation pattern is compressed so that copies of the main lobe enter the visible region of $-1 \leq u \leq 1$ and $-90° \leq \vartheta \leq 90°$, respectively.

The same approach applied in a 2D-setup leads to a 2x2 grid of Diracs in the xy-plane. This leads to a periodic cosine structure in the uv-plane and ultimately to a cross-like radiation pattern in spherical coordinates (Figure 2.12).

The method described here is also valid for arrays using arbitrary transducer positions, however, the individual summands can usually not be combined to cosine terms.

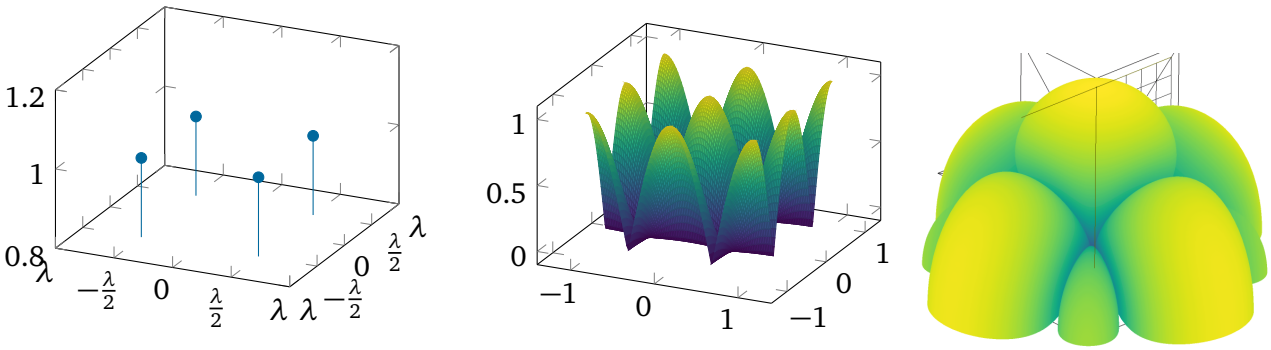

(a) (b) (c)

Figure 2.12.: Example of a 2D-aperture of four array elements arranged in a rectangular grid of $d = \lambda$. Excitation modeled as four dirac pulses in the aperture plane (a), Fourier-transform in the uv-plane (b) leads to the radiation pattern (c).

2.8 Numerically solving the Rayleigh-integral

One approach for solving the Rayleigh-integral (Equation 2.19) is the approximation of replacing the integral by a finite number of evaluation points. This means the continuously vibrating surface is replaced by a number of point sources n, each representing a part of the area $A(n)$ of the original surface and a mean velocity $v(n)$ over that area. The Rayleigh-integral then becomes

$$p_m(x,y,z) = \frac{j\omega\rho}{2\pi} \sum_{k=0}^{n} v(n) \frac{e^{-jkr}}{r} A(n). \tag{2.30}$$

The sum over all $A(n)$ has to match the area of the original vibrating surface. It is obvious that this estimation gets better, the more elements are used. Several elements per wavelength are necessary to model interference effects. Examples for suitable meshes are shown in Figure 2.13. Most meshing algorithms use triangular meshes as these are commonly used for the Finite Element Method (FEM) and required for computer graphics, however, for the approach shown here, other beneficial meshing strategies based on rectangular or hexagon grids exist [35].

The approach of numerically solving the Rayleigh-Integral is not used in this thesis as the focus are arrays operated in the far field. Here, either closed form solutions exist or can be easily obtained using the Fourier transform as shown in section 2.7.

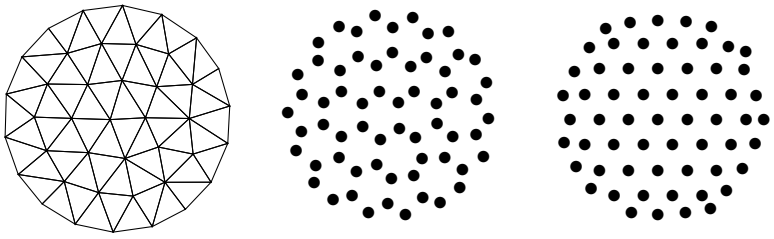

(a) (b) (c)

Figure 2.13.: Meshing of a circle using Distmesh [36] (a) and extraction of centroids (b) of each surface element. An alternative meshing strategy is a hexagonal mesh (c) where each centroid has six neighbors compared the approach using triangles.

2.9 Beamforming

Steering to a certain direction or focusing on a certain location requires a time delay Δs or phase shift Ψ for each transducer. This set of delays is sometimes called a *Focal law* in NDT. In this thesis, two algorithms for obtaining these delays are used: The geometric Delay and Sum (DS) algorithm and a method for obtaining the same delays using the angular frequency domain. The DS algorithm is discussed first.

2.9.1 Delay and sum beamforming

The individual wavelets caused by the transducers shall superimpose either to a planar or curved wavefront. This means constructive interference and thus arrival of the wavelets at exactly the same time. As the velocity of sound is constant, the calculation of delays is a matter of calculating the distance to either a plane or point and then giving the wavelets a head start according to their distance (Figure 2.14). The delays applied for a circular wavefront focusing on a location *FP* are simply the distances of the

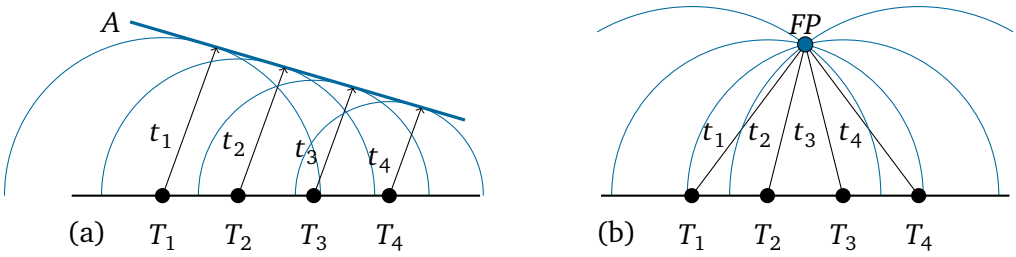

Figure 2.14.: Geometric construction of time delays for steering (a) and focusing (b). The delay between individual transducers is calculated by the euclidean distance to a plane A (a) or a focus point FP (b).

transducers divided by the speed of sound c, i.e.

$$\Delta t_i = \frac{|T_i - FP|}{c} \tag{2.31}$$

Usually the set of delays is normalized to the shortest time of flight, i.e.

$$\Delta t_{\mathrm{n},i} = \frac{|T_i - FP|}{c} - \min(\forall \Delta t_i). \tag{2.32}$$

This is similar to normalizing the accordant phase shifts to a range of $[0° - 360°]$, i.e.

$$\Psi = \left(|A - FP| \cdot \frac{2\pi}{\lambda} \right) \mod 360, \tag{2.33}$$

where mod designates the division remainder.

The same approach applied to a plane wave calculates the distance to a plane A instead of a distance to focal point FP, i.e.

$$\Delta t_i = \frac{|T_i - A|}{c} - \min(\forall \Delta t_{0-n}). \tag{2.34}$$

In a 2D-setup, Equation 2.34 can be reduced using trigonometric relations [Figure 2.15 (a)], i.e.

$$\Delta t = \frac{\Delta s}{c} = \sin(\vartheta_s) \cdot \frac{d}{c} \tag{2.35}$$

and

$$\Psi = \sin(\vartheta_s) \cdot d \cdot \frac{2\pi}{\lambda}, \tag{2.36}$$

where ϑ_s is the steering angle. The result is a sinusoidal relation between ϑ_s and the phase shift Ψ [Figure 2.15 (b)].

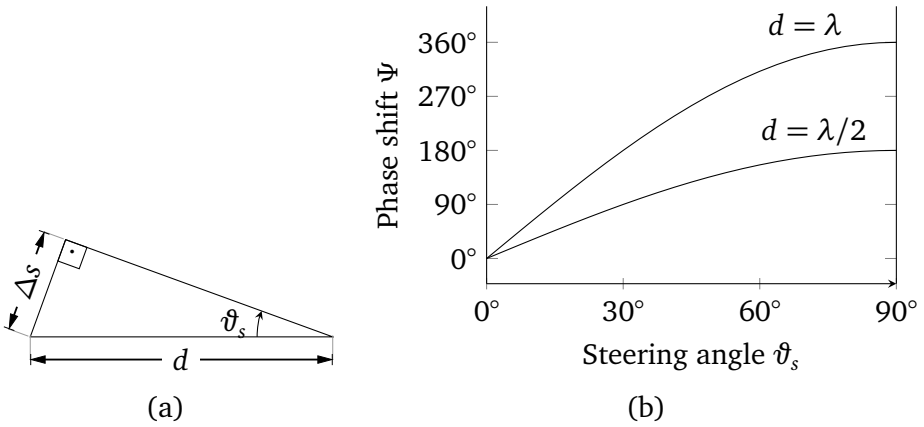

Figure 2.15.: Relationship between the steering angle ϑ_s and the difference in distance Δs that leads to a time delay Δt (Equation 2.35) (a). The time delay can also be expressed as a phase shift Ψ as a function of steering angle (Equation 2.36).

2.9.2 Beamforming in the spatial frequency domain

As shown in section 2.7, there is a direct relationship between the array directivity $E(\vartheta, \varphi)$ and the velocity distribution $v(x_q, y_q)$ of the aperture. This approach can also be used for beamforming. The method again is explained in a 2D-plane, i.e. $\varphi = 0°$. The desired beam profile is modeled in the spatial frequency domain. For a single beam steering into a certain direction ϑ_s, a single Dirac pulse is shifted to ϑ_s, i.e.

$$E(\vartheta) = \delta(-\vartheta_s). \tag{2.37}$$

As the spatial Fourier transformation requires the sound pressure to be expressed as a function of u, a coordinate transformation of $u = \sin(\vartheta)$ is applied, i.e.

$$E(u) = \delta(\arcsin(-\vartheta_s)). \tag{2.38}$$

The required velocity distribution $v(x_q)$ on the aperture is obtained by applying the inverse Fourier transform, i.e.

$$v(x_q) = \int_{-\infty}^{\infty} e^{-jkux_q} E(u) \mathrm{d}u = e^{-jk \arcsin(-\vartheta_s) x_q}. \tag{2.39}$$

This is a complex function, although in the special case of steering to $\vartheta_s = 0°$, $v(x_q)$ is constant and real, i.e. all transducers are excited using the same signal [Figure 2.3 (a) and (d)]. Calculating the phase of the complex function $v(x)$ results in a function for the phase shift Ψ as a function of x_q, i.e.

$$\Psi(x_q) = \arg(v(x_q)) = k \arcsin(-\vartheta_s) x_q. \tag{2.40}$$

Obtaining the phase shifts for each transducer is a matter of evaluating $\Psi(x)$ at the transducer positions.

Mathematically speaking, this a sampling of $v(x)$ at the transducer positions of $\pm\lambda/4$, i.e.

$$v_s(x) = \delta(-\lambda/4)v(-\lambda/4) + \delta(\lambda/4)v(\lambda/4) \tag{2.41}$$

The radiation pattern is given by the Fourier transform of the sampled velocity distribution, i.e.

$$E(u) = \int_{-\infty}^{\infty} v(x) \cdot e^{-jkux} dx = \cos[u - \arcsin(-\vartheta_s)]. \tag{2.42}$$

This entire process is shown for two different steering angles of $\vartheta_s = 0°$ and $\vartheta_s = 45°$ in Figure 2.16. The method described here is more generalized than the geometric approach. As soon as the aperture velocity function $v(x_q, y_q)$ is found, the phase shifts Ψ for any transducer arrangement are simply obtained by sampling $v(x_q, y_q)$ at the respective transducer locations. The downside is that the method does only deliver phase shifts and not true time delays. This becomes an issue as soon as the transducers are to be excited using only a few cycles and steady state conditions are therefore not met.

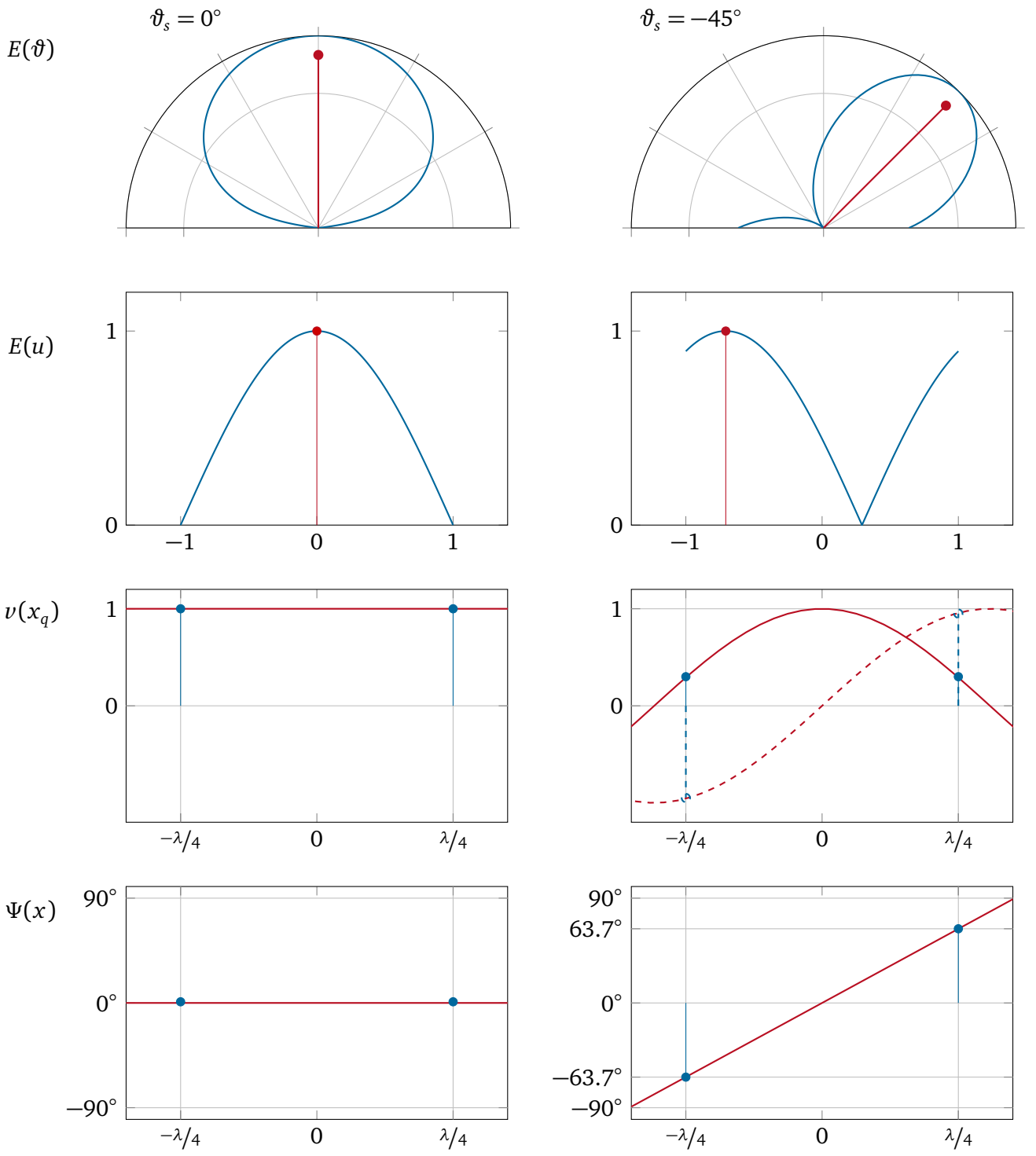

Figure 2.16.: Calculation of focal laws in the spatial frequency domain. A Dirac pulse (red) is positioned in the polar plane $E(\vartheta)$ according to the desired steering angle ϑ_s. This function is transformed to the spatial frequency domain $E(u)$ as preparation for the inverse Fourier transform to obtain the velocity distribution $v(x_q)$. This is a complex function of real part (solid) and imaginary part (dashed). The phase of this complex function is the phase shift $\Psi(x)$. Either the phase shift function $\Psi(x)$ or the velocity distribution are sampled by multiplying with Dirac pulses at the positions of the transducers (blue). The Fourier transform of these two pulses back of the $E(u)$-plane and transformation in the polar plane $E(\vartheta)$ leads to the expected radiation pattern.

2.10 Spatial filter and Direction of Arrival (DOA)

The same principal of superimposing the individual transducers also applies when operating a phased array as a receiver. In contrast to the sending case, superimposing does not happen in the medium in the physical domain but in the receiving electronics. If a sound source is located directly in front of the array in the far field, all transducers receive the same signal, similar to the case of a parallel wavefront being emitted by an array where all transducers are excited by the same signal. If the source is located off center in front of the array, the individual received signals are subject to a phase shift as the center of each transducer has a slightly different position to the signal source. When the individual signals received are summed up, constructive or destructive summation occurs, depending on the phase shift between the individual signals. For certain positions of the signal source and thus for certain receiving angles, the signals sum to zero. The received amplitude is therefore a function of the receiving angle. Due to reciprocity, this function is the same as the radiation pattern for a given array configuration and the same delays that are suitable for beamforming for transmit (TX) qualify for receive (RX) as well. By artificially delaying the signals before summing them up, the receive characteristic can be altered or *steered* into a specific direction. This behavior is called a *spatial filter*. The same methods used for digital filter design also apply to array design. The only difference is that the physical quantity used here is dimension and not time.

When a static set of delays, steering into a certain direction ϑ_s, is applied during receiving, the array is listening into the direction of ϑ_s. This is useful if a transducer is supposed to receive signals from a specific direction and there is a source of disturbance from a different direction. The amplitude of the disturbance is weighted by the radiation pattern evaluated at the direction of the source of disturbance. In a successful system design, the radiation pattern is to be designed to attenuate the disturbance.

When the individual signals are digitized and the summation takes place in a computer, a number of different delay matrices can be applied on the same data. When all possible angles are evaluated, the received amplitude can be plotted as a function of the steering angle ϑ_s. The maximum of this function is likely the direction where the signal source is located. This method is called Direction of Arrival (DOA)-estimation. Beside this simple search for a maximum, more sophisticated DOA methods exist, such as MUSIC [37] or Capon [38], however, they are not used in this thesis.

As shown in section 2.4, an inter element spacing of $\lambda/2$ is desired for the maximal grating lobe free area. To the author's best knowledge there is no air coupled ultrasound transducer commercially available that has a diameter of $\lambda/2$ or less. The ultrasound transducer used in the two arrays by Takahashi et. al. [13] and Unger et. al. [14, 15, 16] is the MA40S4S (Murata Seisakusho, Kyōto, Japan) [17] [Figure 2.17 (a)].

This part is a flexural piezo electric transducer in a cylindrical housing with a diameter of $\varnothing = 10\,\text{mm}$. A tightly packed array made up of these transducers has a pitch of 1.2λ and thus shows grating lobes even if not steered. Murata offers also offers the *MA40H1S-R*. This is a square-shaped, 5.2 mm × 5.2 mm, surface mounted transducer also operating at 40 kHz. This corresponds to a relative edge length of $0.6\cdot\lambda$ and thus allows building an array with a grating lobe free area of about 41°, see Equation 2.14. This device is not publicly available but is only sold to customers selected by Murata.

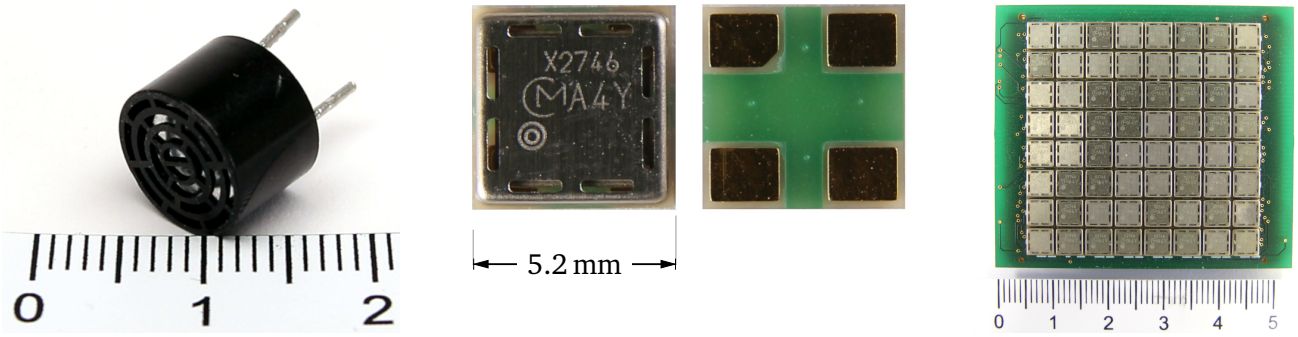

(a) Murata MA40S4S/R (b) Murata MA40H1S-R (c) 8x8 array of MA40H1S-R

Figure 2.17.: Ultrasound tranducers by Murata Seisakusho, Kyōto, Japan. The popular and widely available MA40S4S is cylindrical shaped with a diameter of $\varnothing = 10\,\text{mm}$ (a). A square-shaped, 5.2 mm × 5.2 mm surface mounted ultrasound transducer, the MA40H1S-R (b) is only available for selected customers. It allows building of a direct $\lambda/2$-array when operated at 33 kHz.

Both discussed transducers are narrow band, meaning the rated sound pressure is only available at the specified excitation frequencies. Running the transducers at lower frequencies, allowing a $\lambda/2$-spacing, results in a significant loss in sound pressure (Figure 2.18).

There are two micro electro mechanical system (MEMS) devices originally designed for audio applications that are also suitable for ultrasound applications. These are the MEMS microphone SPU0410LR5H-QB (Knowles Electronics, LLC. Itasca, IL, USA) [39] and the MEMS speaker ACHELOUS of the Ganymede product family (USound GmbH, Graz, Austria) [40]. The SPU0410LR5H-QB microphone is rated for frequencies up to 80 kHz in a surface mounted package measuring 3.76 mm × 3.00 mm [Figure 2.19 (a)]. The dimensions allow $\lambda/2$-arrays of frequencies of up to 45.6 kHz and 57.2 kHz respectively. The surface mounted package is a so called *zero-height* surface mounted device. This means the acoustic aperture is located at the bottom of the device, and, thus, requires a hole in the PCB carrying the device [Figure 2.19 (b)]. The ACHELOUS speaker is rated from 10 Hz up to 80 kHz and produces a sound pressure of up

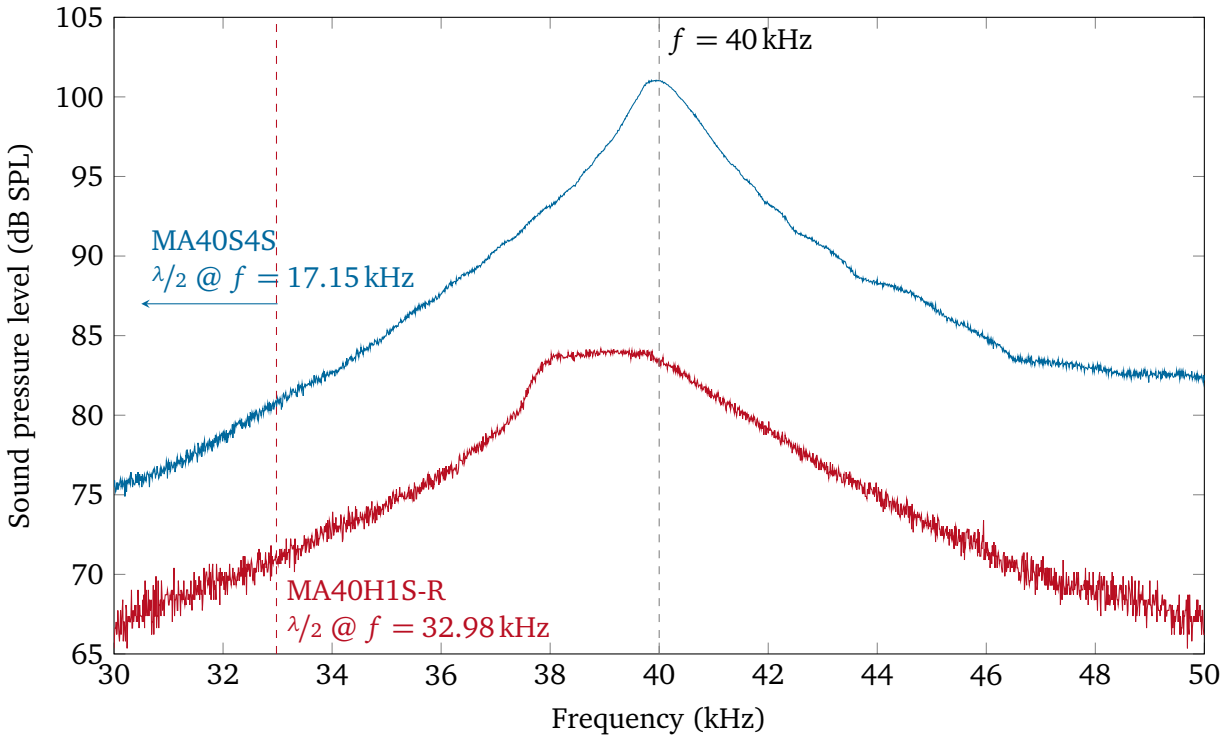

Figure 2.18.: Sound pressure of the Murata MA40S4S/R and MA40H1S-R as function of excitation frequency. Both transducers are rated for a frequency of $f = 40\,\mathrm{kHz}$. When operating the transducers at lower frequencies to match $\lambda/2$ to their dimension, only significant lower sound pressures are generated.

to 90 dB SPL at a distance of 100 mm. The device also comes in a surface mounted package measuring 4.7×6.7 mm, which corresponds to native $\lambda/2$-frequencies of 36.5 kHz and 25.6 kHz respectively. At the time of writing this thesis, October 2018, the device has not been available for testing.

The array theory presented so far assumed infinitely small array elements modeled as Dirac pulses. Such elements radiate perfectly in all directions and thus have no directivity. The available real transducers have of course a finite vibrating surface, and, thus, do not radiate equally in all directions. When a piston transducer is assumed, Equation 2.23 computes the directivity of a single transducer. Examples for radiation patterns were shown in Figure 2.10. The vibrating surface of an array, consisting of real transducers, is given by the convolution of an ideal array $v_a(x_q)$ consisting of Dirac pulses as shown before and the velocity distribution of the transducer element $v_e(x_q)$.

$$v(x_q) = v_a(x_q) * v_e(x_q), \tag{2.43}$$

where $*$ is the convolution operation. Because the far field is the Fourier transform of the vibrating surface (section 2.7), this convolution is solved in the spatial frequency domain by multiplication, i.e.

$$E(\vartheta) = E_a(\vartheta) \cdot E_e(\vartheta). \tag{2.44}$$

This is known as the *pattern multiplication theorem* (Figure 2.20, [41]). It is obvious that the larger the aperture of the transducer is, the stronger the directivity caused by the element factor $v_e(x_q)$ is. For a $\lambda/2$-array, the maximum diameter of the transducers is $\lambda/2$, which is only a barely notable effect.

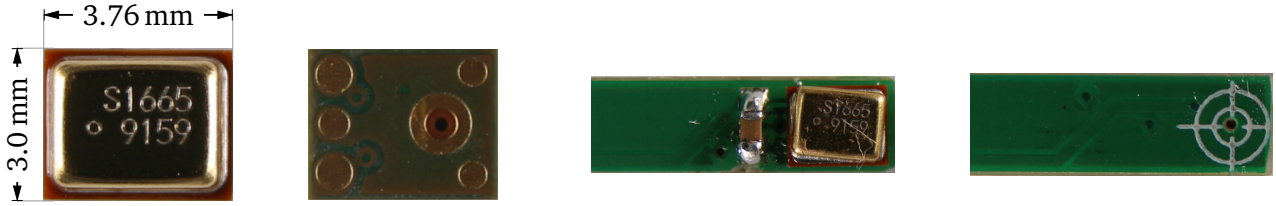

(a) Top (b) Bottom (c) On PCB (d) Bottom of PCB

Figure 2.19.: MEMS microphone SPU0410LR5H-QB by Knowles, dimension 3.76 mm × 3.00 mm with acoustic aperture on the bottom. Single device top (a) and bottom (b), Device mounted on a PCB (c) with hole for acoustic aperture (d) marked by crosshair in the silkscreen (white).

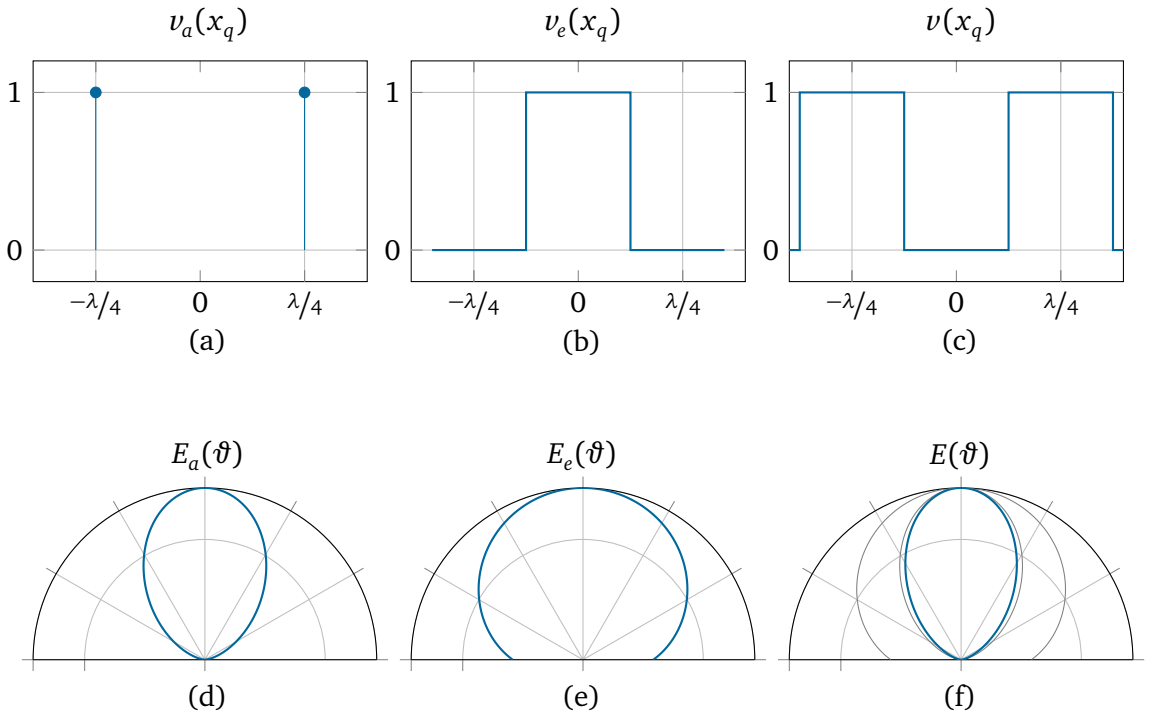

Figure 2.20.: The pattern multiplication theorem visualized. Vibrating surfaces of an array consisting of: Ideal point sources (a), single real transducer modeled as piston transducer (b), array consisting of real transducers obtained by convolution of (a) and (b). Radiation patterns of: Ideal array (d), single real transducer modeled as piston transducer (e), array consisting of real transducers obtained by multiplication of (d) and (e).

3 Waveguide design and mechanics

As shown in section 2.11, there is no ultrasound transducer available suitable for a direct $\lambda/2$-array. The approach of separating the vibrating from the acoustic aperture as shown by Unger [14, 15, 16], Takahashi [13] and proposed by Langen [12] for 1D-arrays is promising as arbitrary transducers can be retrofitted to a $\lambda/2$-pitch or, given a suitable waveguide is used, to any other desired array layout (Figure 3.1).

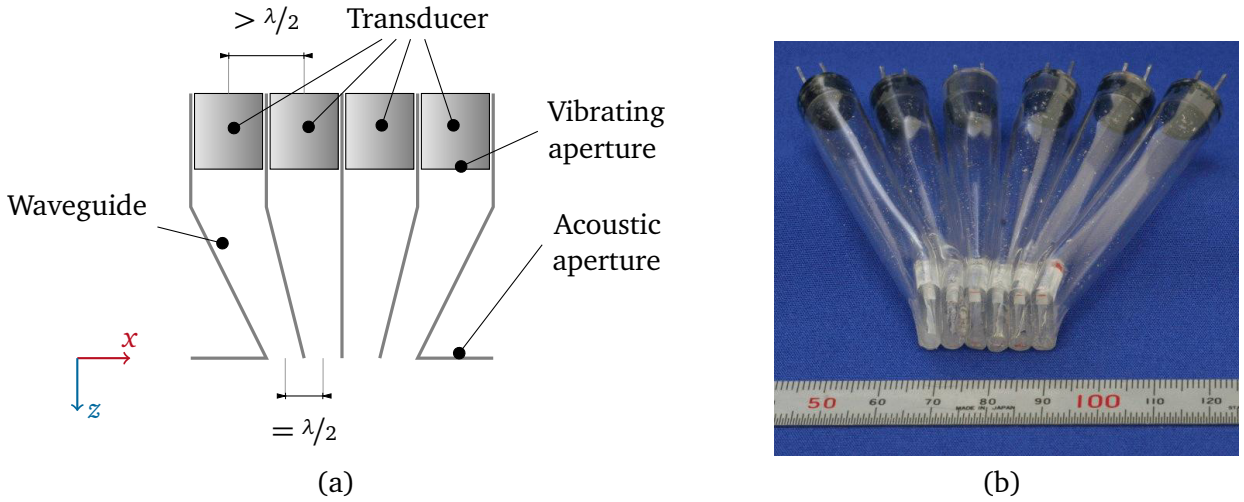

Figure 3.1.: Concept of separating the vibrating aperture and the acoustic aperture using a waveguide (a) and realization by Takahashi [13] (b). This allows building an array with a pitch of $\lambda/2$ using transducers with a diameter of $> \lambda/2$. (b) is reprinted with permission from SPIE Digital Library from T. Takahashi, R. Takahashi, S. Jeong, *Ultrasonic phased array sensor for electric travel aids for visually impaired people*, Proceedings Vol. 6794, ICMIT 2007: Mechatronics, MEMS, and Smart Materials, 2007, Gifu, Japan [13].

Beside the additional degree of freedom in aperture layout, the approach enables other benefits:

- By using the waveguide, an array of small aperture but high sound pressure can be realized: As the transducers do not need to fit into the aperture area, the transducer can consume virtually any build volume necessary to produce the desired sound pressure.

- As the transducers are separated from the aperture, the waveguide can protect the transducers from any harsh environment such as high temperature or aggressive chemical compounds.

In this thesis, waveguides are designed using computer aided design (CAD) and then fabricated using low-cost desktop 3D-printers utilizing the fused deposition modeling (FDM) method [42], as the feasibility of such parts for ultrasound acoustics has already been shown [25, 43]. Therefore, a geometrical definition of the waveguide geometry is needed. In contrast to the previous work, fully populated 2D-arrays are realized. Two different waveguide designs are used.

The first design is similar to the design presented by Unger [14, 15, 16]: A structure of channels of the same length connect the aperture openings to the transducers. This allows ultrasound waves emitted by the transducers in parallel to arrive at the aperture at the same time. The transducers are not directly

mounted on a printed circuit board (PCB) and their positions are the result from bundling the elastic channels together as close as possible. This design will be called *equal length waveguide*.

The second design acknowledges the fact that for steering, the signals need to be delayed anyway so the requirement for equal lengths of the channels is relaxed. As the transducers can now be placed freely, they are placed in a 2D-plane. This is beneficial for the fabrication as all transducers can be soldered directly onto a single PCB. This design will be called *freeform waveguide model*

3.1 Aperture design

Both designs share the same aperture design of 8×8 elements arranged in a rectangular grid (Figure 3.2). The elements are spaced $\lambda/2 = 4.3\,\text{mm}$ apart. The shape of each element is a circle with diameter of $\varnothing = 3.4\,\text{mm}$. This leaves a minimum wall thickness of 0.9 mm at the acoustic aperture between the individual elements. This value is chosen as most desktop 3D-printer use a 0.4 mm nozzle and it is desired to allow two lines of material of the FDM-process between the elements. The expected directivity pattern is calculated as shown in section 2.7.

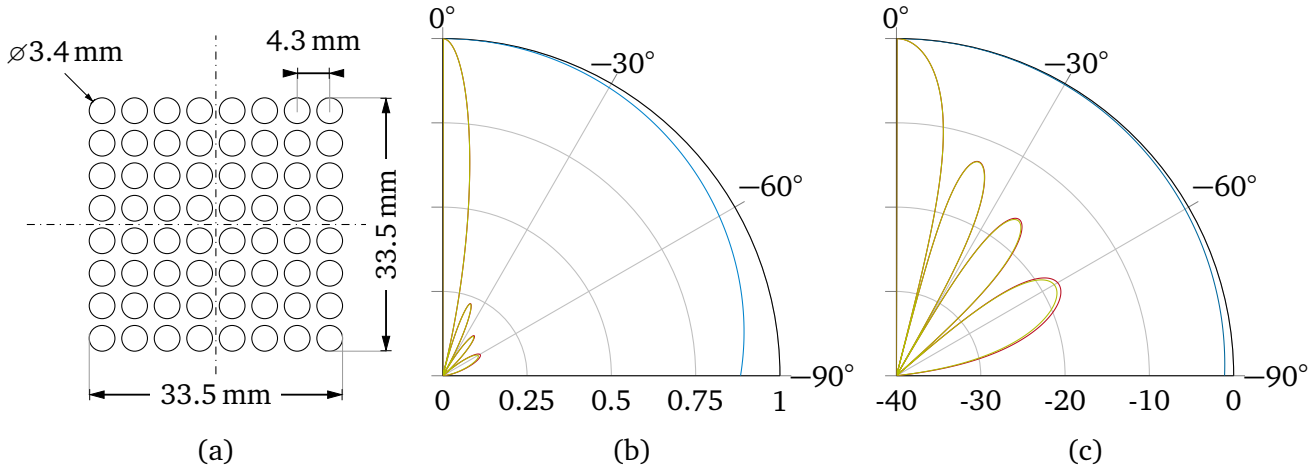

Figure 3.2.: Aperture of the two waveguides, scale 1:1. 8×8 elements arranged in a rectangular grid, spaced $\lambda/2 = 4.3\,\text{mm}$ apart (a) and the expected directional response of the array using a linear scale (b) and using a logarithmic scale (c) (red). The individual elements are modeled as piston transducer (Equation 2.23) of $\varnothing 3.4\,\text{mm}$ (blue). Including the element factor (Equation 2.44) is barely noticeable (green).

3.2 Equal length waveguide model

The equal length waveguide connects each aperture opening to an ultrasound transducer using channels of the same length. This enables exciting a plane wave propagating perpendicularly to the aperture when all transducers are excited by the same electrical signal. Additionally, the channels shall intersect the aperture plane perpendicularly to prevent any refraction on the transition from inside the waveguide channel into open air.

From these goals, mathematical descriptions for the center lines of the channels are derived. The complete channel geometry is derived from the center line afterward by adding the circular cross section.

The whole approach is first shown for a line array and then generalized for a 2D-array. Assuming that the aperture plane is the xy-plane, the construction of the center lines happens in the xz-plane. The result is a horizontal line array.

Constraining an arc to a constant arc length

Arcs of a circle are selected as the fundamental geometric primitive for the center line. Such an arc is defined by 5 degrees of freedom [Figure 3.3 (a)]: The center coordinates p_x, p_z and radius r of the corresponding circle as well as the start angle α and stop angle β or a difference angle $\gamma = \beta - \alpha$. From the design goals, 4 degrees of freedom are already set:

1. $p_z = 0$ because the channel line shall intersect the aperture plane perpendicularly;
2. p_x is linked to r because the arc shall intersect the center of one element in the aperture;
3. $\alpha = 180°$ because the channel line shall start at the aperture plane;
4. r and γ are linked by $s = \gamma \cdot r$, where s is the arc length, assuming γ is given in radians.

The remaining degree of freedom is either the radius r or the angle difference γ [Figure 3.3 (b)].

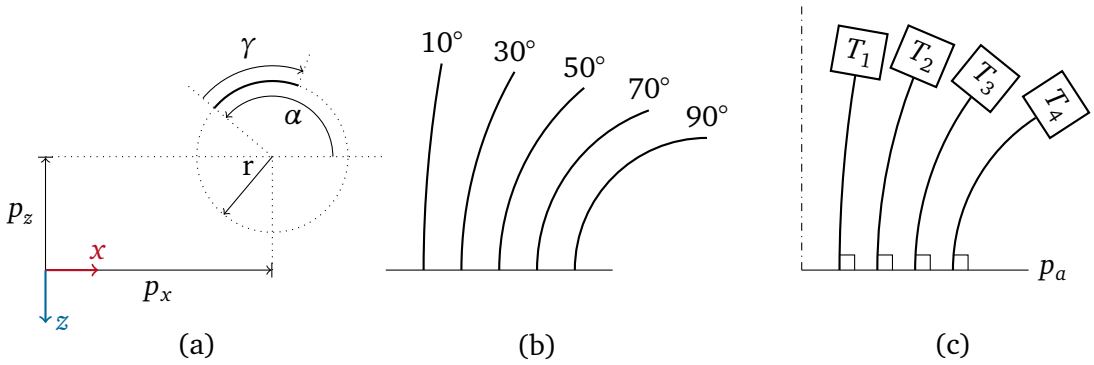

Figure 3.3.: The 5 geometrical degrees of freedom of a circular arc: Center position consisting of p_x and p_z, the radius r and the two angles α and γ defining, respectively, the start and the length of the arc (a). When constrained to a fixed length, one degree of freedom remains. Examples of such arcs for a fixed length and different opening angles γ of 10°, 30°, 50°, 70° and 90° (b). The final opening angles of the channel center lines are the result of packing the transducers close together, starting with the innermost transducer T_1 (c).

Positioning of transducers

The remaining degree of freedom is set by bundling the center lines together as close as possible, providing just enough space at the far end to accommodate the transducers, starting with the transducer closest to the z-axis.

The transducer is approximately a cylinder shaped object which is a rectangle when projected on the xz-plane. This means the space between the far end of the construction line depends on the orientation of the transducer. In order to simplify the construction, the worst case, i.e. a circle large enough to

accommodate the transducer is assumed. This is the same as requiring an euclidean distance of the circle diameter between the channel lengths. The final result constrains centerlines fully [Figure 3.3 (c)].

Generalizing to a 2D-waveguide

For a 2D-waveguide, the individual center lines are no longer contained in a plane but real three dimensional curves. However, the arc definitions from xz-plane are valid projections of these curves. Placing the same curve definitions perpendicular in the yz-plane allows reconstructing the full three dimensional curve. This is done by extruding the projected arcs and, thus, obtaining cylinder shell sections. For four arcs in both the xz- and yz-plane, respectively, the result are eight cylinder shell sections and 16 intersection curves (Figure 3.4).

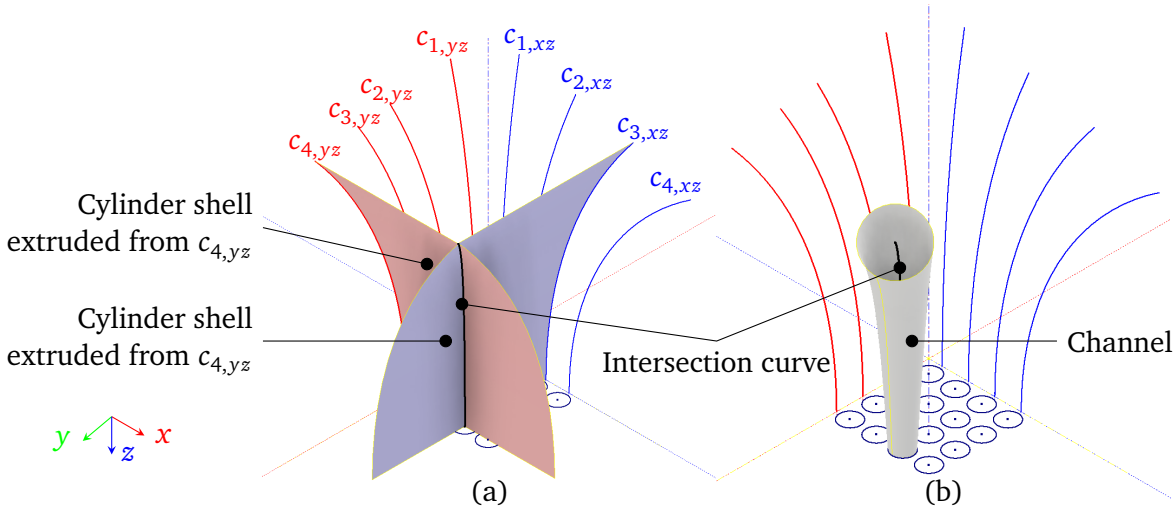

Figure 3.4.: Reconstruction of a three dimensional curve from two perpendicular projections. The center lines for a line array are positioned in both the xz-plane (blue) and the yz-plane (red). Each center line is extruded to a cylinder shell. The 16 intersections of those eight cylinder shells are the reconstructed three dimensional center lines (a). The final channel geometry is the result of combining the center line with the two circular cross sections at both ends (b).

These curves are slightly longer than the desired channel length. The reason is that the length of the projected curve is always shorter than the original curve. This is caused by the projection that removes one dimension that contributes to the overall length. The only exception to that rule is a curve that is contained in the projection plane and that is, thus, identical to the projection in the first place. Unfortunately, the calculations for the unprojected curve length include elliptical integrals and are therefore to be solved numerically. This is done using a regular CAD software (Creo, Parametric Technology Corporation, Needham, MA, USA). The CAD model features a parameter table allowing changes according to frequency, transducer diameter and acoustic aperture pitch of the array.

After the intersection curves are trimmed to the desired length, a circular cross section completes the channel geometry. Additionally, sockets matching the transducer geometry hold the ultrasonic transducers in place and allow precise mounting. Mounting points are added between the channel openings that hold an interposer PCB using conventional hex standoffs. The PCB collects the individual transducer pins to two high density connectors for easy connection to the electronics. The transducer pins need to be extended in order to reach the PCB. As they are soldered, they are not easily replaceable (Figure 3.5).

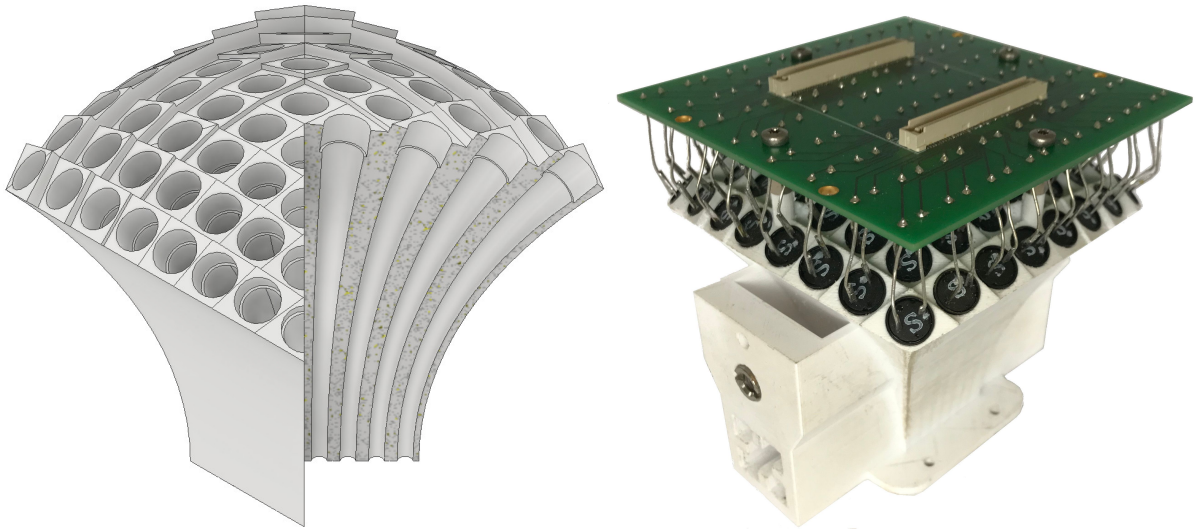

(a) (b)

Figure 3.5.: Cross section of waveguide CAD-model (a) and photo of complete waveguide assembly (b). The waveguide shrinks down the pitch between the transducers to the desired pitch of $\lambda/2$. The transducers are mounted in sockets at the channel ends and the pins are extended to reach an interposer PCB mounted above the waveguide. The interposer collects the transducer pins to a high density connector. The waveguide further features mounting points for a 1/4" tripod screw and a 20x20 t-slot profile as well as a flange for mounting a rigid baffle.

3.3 Freeform waveguide model

As steering the ultrasound beam requires delaying individual signals anyway, the freeform waveguide model does not require channels of equal lengths but requires compensation in the electronics. This allows the transducers to be mounted on a flat PCB or allows in the future transducer arrays fabricated on planar substrates.

Bezier curves

The fundamental curve primitive of this waveguide are Bezier curves [44]. Originally invented by the French automotive industry in the 1960s, Bezier curves are nowadays widely used in computer graphics to describe freeform geometry. Generally, Bezier curves interpolate between a start and an end point over a number of intermediate control points. These control points bend the curve. However, in contrast to other interpolation techniques, they usually do not intersect the generated curve. Linear Bezier curves use no intermediate control points and linearly interpolate between the start and the end point. Cubic Bezier curves use two intermediate control points. The connecting line of the start point to the first control point is the first tangent of the resulting curve while the connecting line of the second control point to the end point is the second tangent, respectively (Figure 3.6). There are two algorithms available to evaluate Bezier curves: The *de Casteljau*-algorithm which uses a number of cascaded linear interpolation steps, and the method using *Bernstein polynomials* [45]. Both result in parametrization of the curve as a

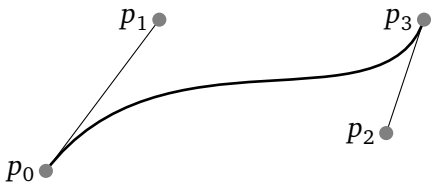

Figure 3.6.: Example of a cubic Bezier curve interpolating between the start point p_0 and the end point p_3 over the two control points p_1 and p_2. The connecting lines of p_0 and p_1 as well p_2 and p_3 are tangents of the curve.

function $x(t), 0 \leq t \leq 1$. Here, the approach using Bernstein polynomials is used. The parametrization of the curve is given by

$$x(t) = \sum_{i=0}^{n} B_{i,n}(t) \cdot p_i, \tag{3.1}$$

where $B_{i,n}$ is the group of Bernstein polynomials of the n-th order and p_i is the i-th control point. The structure of Equation 3.1 is a weighted sum of the control points where the weight of the i-th control point $B_{i,n}(t)$ is the Bernstein polynom which is a function of t. Bernstein Polynoms are a family of polynomials given by

$$B_{i,n}(t) = \binom{n}{i} t^i (1-t)^{n-i}, \tag{3.2}$$

where n denotes the order of the equation set. For $n = 1$, the resulting two polynomials are simply t and $1-t$ which is equivalent to a linear interpolation between p_0 and p_1. For the common case of $n = 3$, the resulting four polynomials are

$$B_{0,3}(t) = (1-t)^3 \qquad B_{1,3}(t) = 3t(1-t)^2 \qquad B_{2,3}(t) = 3t^2(1-t) \qquad B_{3,3}(t) = t^3. \tag{3.3}$$

The set of Bernstein polynomials for any given n is a partition of unity in the range of $0 \leq t \leq 1$. This means that the sum of all Bernstein polynomials for a certain n in the given range is always equal to one (Figure 3.7) [45].

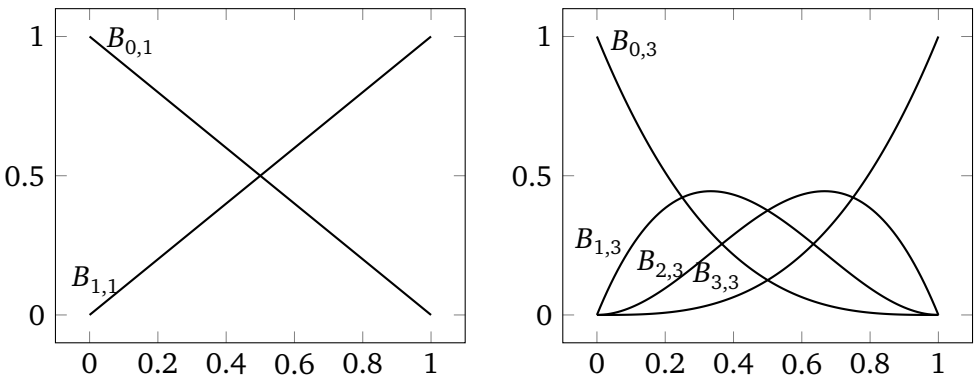

(a) Linear (b) Cubic

Figure 3.7.: Bernstein polynomials for linear (a) and cubic (b) Bezier curves. Both set of curves are a partition of one, meaning that for every t in the interval of $0 \leq t \leq 1$, $\sum_{i=0}^{n} B_{i,n}(t)$ equals one [45].

Calculation of channel lengths

In order to compensate the different channel lengths in this waveguide model, the channel lengths are calculated by the well known formula for a curve length [32, p. 480], i.e.

$$L(a,b) = \int_a^b \sqrt{\dot{x}^2(t) + \dot{y}^2(t) + \dot{z}^2(t)}\,\mathrm{d}t\,. \tag{3.4}$$

The Bernstein polynomials (Equation 3.3) are easily derived, i.e.

$$\dot{B}_{0,3} = -3(1-t)^2, \qquad \dot{B}_{1,3} = 3 - 12t + 9t^2, \qquad \dot{B}_{2,3} = 3(2-3t)t \quad \text{and} \quad \dot{B}_{3,3} = 3t^2. \tag{3.5}$$

and the resulting integral is solved by numerical integration.

Finding the control points

In order to define a cubic Bezier curve, the four control points need to be found according to the waveguide specification. The start and the end points are given by the center points of the aperture elements and the center points of the transducers arranged in a similar grid on the transducer plane. As the channels shall be normal to both the aperture and transducer planes, the direction of the vector connecting the plane and the corresponding control point is normal to the corresponding plane. The length of the normal vector is arbitrarily set to be $1/3$ of the euclidian distance d between the start and the endpoint (Figure 3.8).

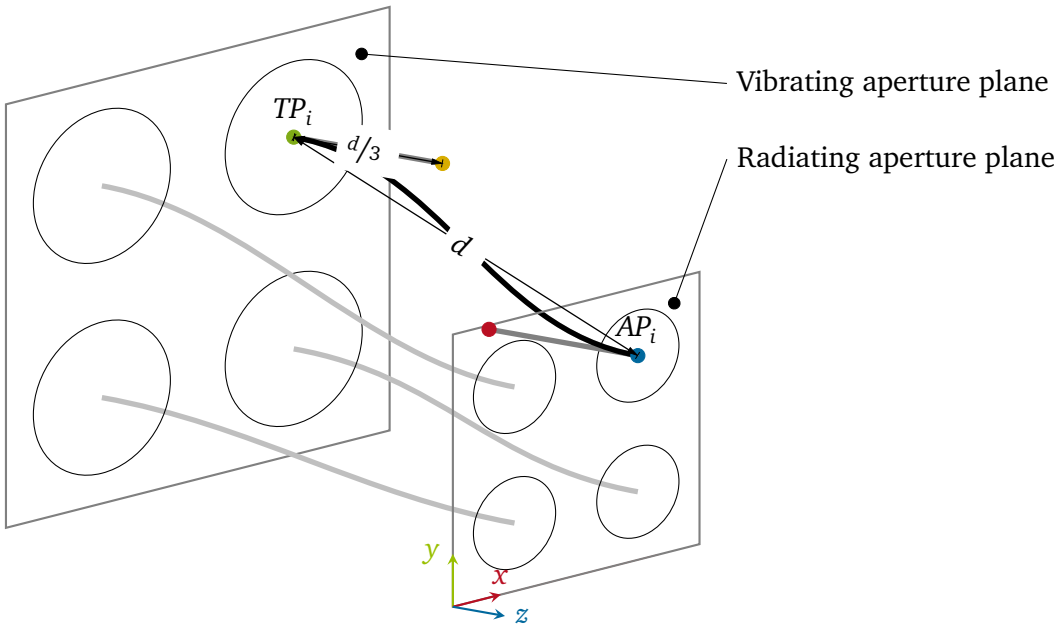

Figure 3.8.: The freeform waveguide model connects the center points AP_i of the aperture openings to the center points of the transducers TP_i using a cubic Bezier curve. The two tangent control points are obtained by a normal vector from the respective plane that has a length of $d/3$ where d is the euclidean distance between both center points.

In this thesis, a symmetrical waveguide with a distance of 80 mm between the aperture and transducer planes is used. Besides symmetrically waveguides, this model allows off-center transducer arrangements

as well as transducer planes that are not parallel to the aperture plane. The channel lengths are calculated using Equation 3.4, normalized to the longest channel length and converted to time delays. The necessary compensation delay for each channel is given by

$$t_i = \frac{s_{\max} - s_i}{c}, \tag{3.6}$$

where s_i is the length of the i-th channel, $s_{\max}$ is the length of the longest channel and c is the speed of sound (Figure 3.9).

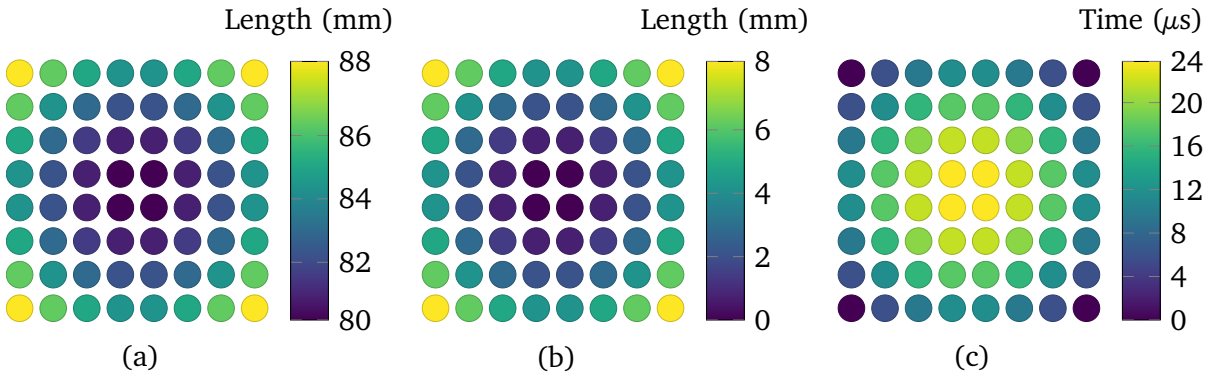

Figure 3.9.: The calculated lengths (a), lengths normalized to the shortest length (b) and necessary compensation delays (c) for a symmetric 8×8 array where the transducers are arranged on a plane, distance 80 mm in a pitch of 11.2 mm.

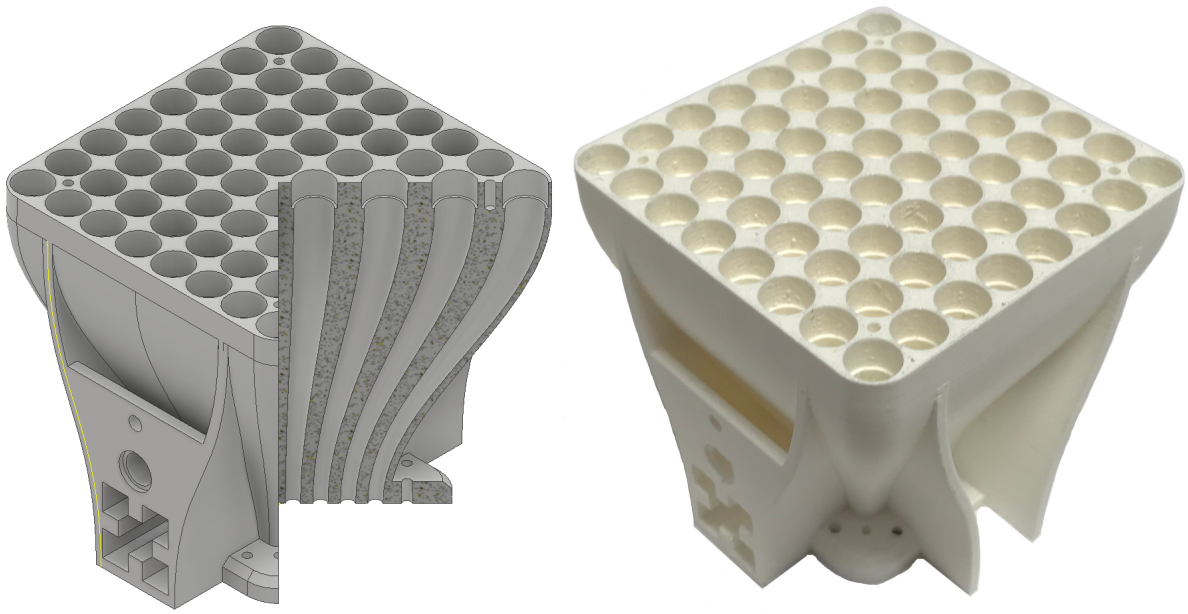

Figure 3.10.: CAD-model, three quarter view (a), and photo (b) of freeform model waveguide. The individual channels feature housings for precise mounting of the transducers. The transducers are directly soldered onto an interchangeable PCB.

3.4 Fabrication of waveguides

Both waveguide designs were fabricated using a commercial, low cost, desktop 3D-printer (Ultimaker 2, Ultimaker BV, Geldermasen, Netherlands), utilizing the FDM method [42]. An FDM printer melts plastic

supplied as filament on a spool in a heated nozzle. The nozzle is attached to a computer-controlled motion system that moves the nozzle according a pre-calculated path and deposits material along that path. The produced part is therefore made of thin strings of material that adhere to each other. As the process is rather slow, objects are typically hollow to save printing time. Common materials include acrylonitrile butadiene styrene (ABS), polyethylene terephthalate (PETG) or polylactic acid (PLA). Here, a commercial PLA blend, (Innofill PLA, Innofill 3D BV, Emmen, Netherlands), is used. The printing process for each waveguide takes about 36 hours.

After the print is finished, the waveguides are carefully cleaned of any printing artifacts. These artifacts occur because the part requires special settings during printing. Usually, when a 3D-printer moves without dispensing material, the filament is pulled back out of the nozzle by the material feeding system. This lowers the pressure in the nozzle and prevents material from oozing out of the nozzle. This process is called *retraction*. The geometry of the acoustic aperture requires the printer to retract often. The same piece of filament is moved back and forth by the material feeding system, leading to grinding of material in the feeder and ultimately in a fatal block of the feeder. Therefore, it is necessary to disable retraction and manually removing the artifacts of oozing. This is done using different hand tools such as small screwdrivers, brushes for cleaning bottles and pipe cleaners.

3.5 Waveguide characterization

Both waveguides are characterized according to their acoustic crosstalk. Also, time of flight measurements test the consistency of the equal-length design and verify the formula for the channel length of the freeform design (Figure 3.11). System level characterizations follow in chapter 5 after the electronics and signal processing are presented in chapter 4.

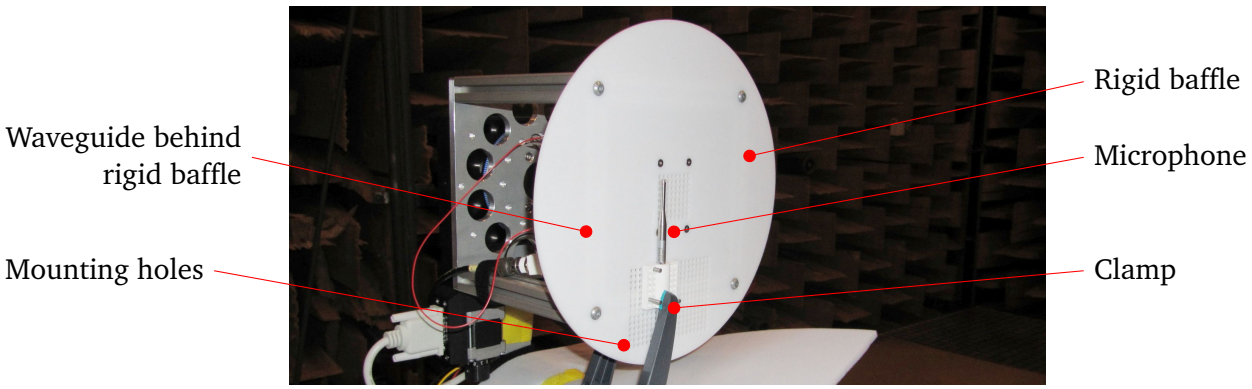

Figure 3.11.: Experimental setup for time of flight measurements. A microphone is positioned in front of the array. The rigid baffle is equipped with a second grid of holes, matching the aperture openings. The microphone holder behind the clamp locks into these holes so that the microphone is precisely positioned in front of each channel opening

3.5.1 Crosstalk

As the transducers are mounted in a waveguide, mechanical and acoustic cross talk occurs. The crosstalk between a single transducer, mounted in one channel, and the other channels is investigated.

A single transducer (again MA40S4S, Murata Seisakusho, Kyōto, Japan), is placed in the corner of the waveguide and is excited using a signal generator (33500B, Keysight, Santa Rosa, CA, USA) using a sinusodial burst of 40 cycles at an amplitude of 10 V. A second transducer, also an MA40S4S, is consecutively placed in all other waveguide channels as receiver. The voltage on the receiver is acquired using an oscilloscope (PXI-5922, National Instruments, Austin, TX, USA).

The amplitudes received are normalized to the exciting signal and shown in a matrix view that resembles the array layout (Figure 3.12). The amplitudes decrease with increasing distance to the sending element. Both waveguides show a similar result with differences of less than 5 dB beside one single data point in the corner.

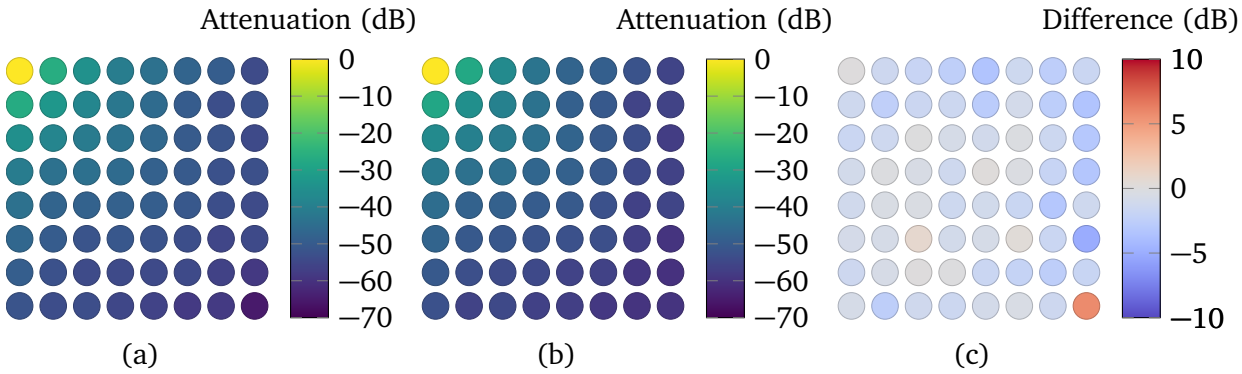

Figure 3.12.: Acoustic crosstalk between the channels of the equal length waveguide model (a), the freeform waveguide (b) and the difference b - a (c). The freeform waveguide model has a slightly lower cross talk besides the one data point in the corner.

3.5.2 Length of the channels in the equal length waveguide

For the time of flight measurements, the same transducer (MA40S4S, Murata Seisakusho, Kyōto, Japan) is placed in each channel of the equal-length waveguide. A mounting setup that resembles the grid of the aperture allows a calibrated microphone(TYPE 4138, Bruel & Kjær, Nærum, Denmark), to be placed in front of each channel opening (Figure 3.11). The time of flights are again shown as matrix resembling the array (Figure 3.13). The measured lengths are all slightly longer, however the distribution of differences is random and does not resemble a symmetric shape. As the waveguide design is symmetric to the center, any deviation in the channel lengths would also be symmetric and, thus, be visible as a symmetric pattern. The constant offset can be electronically compensated, however a constant offset has no influence on the shape of the radiation pattern. Therefore, the equal-length design is considered successful concerning the goal of channels of the same length.

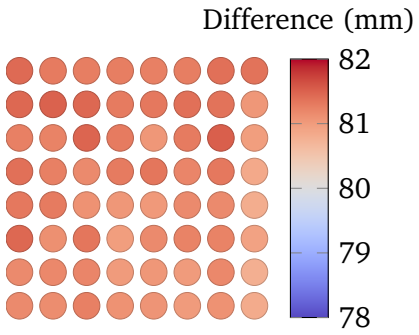

Figure 3.13.: Measured channel lengths of an equal length waveguide. The measured lengths are slightly longer than the desired length of 80 mm. The distribution of the differences shows no symmetry and therefore considered not to be caused by systematic error in the geometric model.

3.5.3 Compensation of different channel lengths

The freeform waveguide is analyzed as in the previous experiment. However, here, different time of flights are expected. The measurements are therefore compared to the calculated channel lengths (Figure 3.14). Here, the difference to the calculated lengths is in the range of 1 mm which is in the range

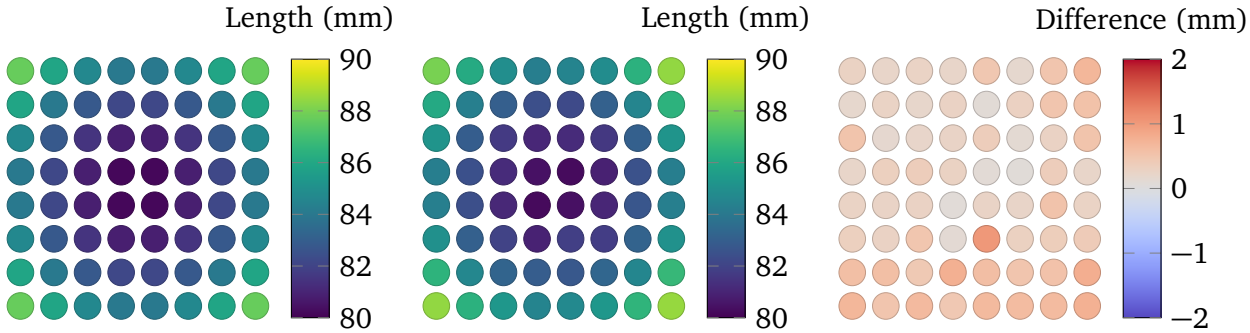

(a) Calculated channel length (b) Measured channel length (c) Difference

Figure 3.14.: Comparision of calculated channel lengths (a) and measured channel length and their difference (c). The measured channel lengths are slightly longer. The shape of the difference is random ($\sigma = 0.21\,\text{mm}$) and, thus, not symmetric.

of the accuracy of the entire mechanical setup. The differences also show no symmetric trend that matches the symmetry of the waveguide. Therefore, the formula for the calculation of channel lengths is considered sufficient to correct the time of flights.

4 Electronics and signal processing

The electronics for exciting the transducers and for digitizing and processing the received signals are a significant part of the overall system. The phased array electronics consist of a digital control integrated circuit (IC), either a micro controller or a Field Programmable Gate Array (FPGA), that receives high level control commands from a user interface and maps them to a low level sequence of send and receive actions. The two tasks of excitation and receiving are usually handled by dedicated ICs connected to the control IC. The characteristics of the excitation and receiving stages are discussed briefly.

4.1 Transmit electronics

The task of transmitting (TX) using an ultrasound transducer is a matter of providing a sinusoidal voltage source of the desired frequency and capable of driving enough current. In a phased array, each transducer in the array needs a separate source. Saving effort and components per source or using components with more than one channel is worth considering.

The general approach of generating a periodic electrical signal using a digital system is called *Direct Digital Synthesis* (DDS) (Figure 4.1): This method relies on a sampled image of the signal in memory.

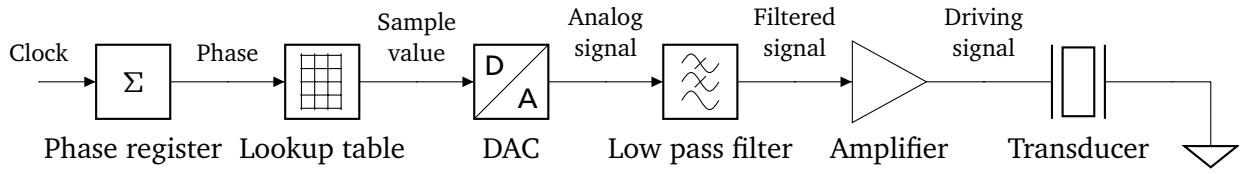

Figure 4.1.: Signal generation using the DDS method. A phase register counts clocks until one oscillation period is over. For each time step, a sample value is looked up and converted to a voltage using an ADC. An anti-alias filter removes higher harmonics caused by the time discretization. In order to drive an ultrasound transducer, an additional power amplifier is required.

One signal oscillation period T is divided into n time steps. A clock signal is set up at a frequency of n/T. The number of elapsed clock cycles is counted in a phase register until n cycles are reached. The phase register is set to zero again and the cycle starts again. For each time step, the amplitude value of the signal is looked up in the memory and then generated using an analog digital converter (ADC). An anti alias filter removes the harmonics introduced by the time discretization. In order to drive the ultrasound transducer, a power amplifier provides the necessary voltage and currents.

According to Shannon's theorem, it is sufficient to sample a signal using a frequency larger than two times the highest signal frequency. Therefore, for the excitation, it is sufficient to synthesize a signal using a minimum of three interpolation points per period of time as long as:

1. There is no amplitude discretization and

2. an ideal anti-alias filter exists.

However, the ultrasound transducer used has a number of characteristics that allow a far simpler system design that uses more time steps in favor of eliminating or replacing some of the components found in the DDS system, especially expensive and power hungry analog components.

As the base frequency of the transducer, 40 kHz, is relatively low, providing three interpolation points per period is rather easy, even with low cost micro controllers. Further increasing the number of interpolation points still is relatively easy but allows decreasing the amplitude resolution. By using the minimum number of two discretization steps for the amplitude, i.e. a resolution of 1 bit, the sine signal reduces to a square wave signal. The sample memory and the ADC are replaced by a comparator stage that divides one oscillation period by a rising and a falling edge.

Because the output signal is only one of two different voltages, a pair of transistors that switch between two different voltage levels replaces the amplifier. The result is a rectangular power signal, however, as the ultrasound transducer is narrow band, it acts itself as the low pass filter and limits the emitted ultrasound reasonably well to the signal's base frequency (Figure 4.2). This approach is common for low-cost narrow band ultrasound systems [46], although systems with more than two different excitation levels exist [47, 48, 49, 50], reducing the requirements on timing and the low pass filter characteristics of the transducers.

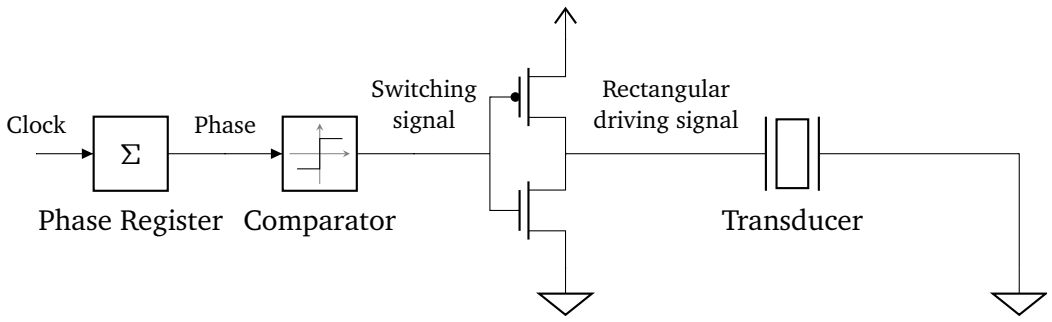

Figure 4.2.: Simplified two-stage excitation architecture suitable for narrowband ultrasound transducers. A phase register counts clocks until a full oscillation period is over and then resets. The switching signal for the power transistors goes high when half of the oscillation period is over. The transducer pin alternates between positive and negative supply, while the other pin is permanently connected to a negative supply.

When using only two excitation levels, the necessary timing resolution for a given angular resolution ϑ_{res} in radians is given by the linear approximation of Equation 2.35, i.e.

$$\Delta T = \vartheta_{\text{res}} \cdot {}^{d}/_{c}. \tag{4.1}$$

Assuming that a digital circuit can output a new digital signal every single clock and one period of time consists of two signal periods, a positive and negative half wave, the required clock frequency is

$$f_c = \frac{2}{\vartheta_{\text{res}} \cdot {}^{d}/_{c}}. \tag{4.2}$$

The required system frequencies are way higher than the base ultrasound frequencies as one signal period has to be divided into many time steps, depending on the required angular resolution (Figure 4.3).

Several companies offer so called ultrasound pulser ICs that include suitable transistors for switching high voltages usually required for the piezo electric ultrasound transducers (Table 4.1). Devices featuring up to 16 channels and up to 17 excitation levels are available.

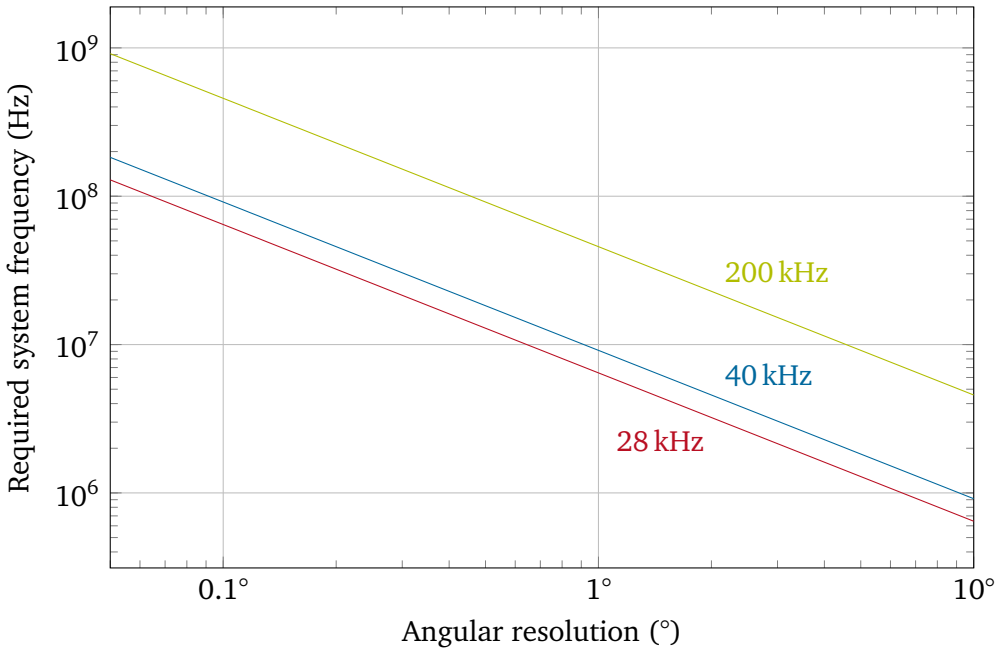

Figure 4.3.: Required system frequencies needed for common air-coupled ultrasound frequencies as function of angular resolution, assuming $d = \lambda/2$ for each frequency and air ($c = 343\,\mathrm{m\,s^{-1}}$).

Both electronics used in this thesis use the same two stage, 8-channel pulser IC (HV7355, Microchip, Chandler AZ, USA) [51]. The device offers two different interface options to the controlling IC: An 8-bit parallel interface consists of 8 digital input pins, each corresponding to one output channel, and a serial interface consuming only three input pins. Both options are interesting as the number of available pins of any micro controller or FPGA is limited. However, the use of the serial interface limits the possible angular resolution given that at least eight clock cycles are necessary to fill the output registers compared to a single clock cycle in the parallel architecture.

Table 4.1.: Commercially available ultrasound pulser ICs. This list is not complete.

Manufacturer	Product	Channels	Output voltage	Voltage levels	Notes	Source
Microchip	HV7321	4	−80 V to 80 V	5	-	[47]
Microchip	HV7322	8	−80 V to 80 V	7	(1)	[48]
Microchip	HV7350	8	−60 V to 60 V	2	-	[52]
Microchip	HV7355	8	0 V to 150 V	2	(2)	[51]
Microchip	HV7358	16	−80 V to 80 V	3	(3)	[53]
ST Microelectronics	STHV800	16	−90 V to 90 V	3	-	[54]
ST Microelectronics	STHV1600	16	−100 V to 100 V	5/3	(3)	[49]
Texas Instruments	TX517	2	200 V	17/5	(4)	[50]

[1] Integrated TX/RX-Switch.
[2] Serial interface.
[3] Integrated transmit beamformer.
[4] Differential output.

4.2 Receiving electronics

The receiving (RX) electronics samples the voltage from all transducers, and, thus, provides signals of amplitude over time. Such a signal is called an amplitude scan (A-scan). The sampling of all channels requires a common time base so that phase shifts between individual channels are precisely reproduced. The typical components of such a system are briefly discussed.

In order to support pulse echo mode, i.e. the same transducers are used first for TX and then afterwards for RX, a protection circuit for the delicate RX electronics is necessary. The typical voltages used for TX significantly exceed the expected voltages during RX and easily damage any analog input stage. Therefore, a transmit/receive switch connects the RX stage only after the excitation is finished.

After a burst is sent and the system is listening for echoes, it is expected that the later any echo arrives, the weaker the received signal is. This is caused by the damping in air that increases for larger distances. A variable gain amplifier (VGA) can increase the amplification factor with increasing time and partially compensate for that loss in amplitude.

The last step is the conversion to a digital bit stream using an ADC, usually equipped with an anti alias filter. Many multi channel ADCs only use a single converter stage combined with an analog multiplexer. This means that no truly parallel conversion is possible and that the timing behavior of the multiplexer must be known as it is necessary for signal reconstruction.

In order to reconstruct the signal, the sampling frequency has to fulfill Shannon's theorem. A similar approach of increasing the sampling frequency and reducing the amplitude resolution also is possible in the RX case: Instead of an ADC, a simple comparator detects the zero crossings in the A-scans. However, this approach results in loss of information and as soon as there is more than one source present, the individual sources are no longer separable using the DS-algorithm. It is therefore not used in this thesis but a full analog sampling of all channels and is implemented in the RX developed electronics described below.

During RX, significant amounts of data accumulate. These must be either processed or recorded in the electronics or sent to another piece of equipment for storing or processing. The downside of local recording is the limited amount of memory restricting the recording time. Typical components used for real time data processing are either FPGAs, graphics processing units (GPUs) or a combination of both. Here, an approach using a GPU is used and the FPGA does not participate in the data processing but is merely used for attaching the ADCs and pulsers to the micro processor.

4.3 Implemented electronics

Two different electronics have been designed that are later used for the experiments. The first electronics is TX only for 64 channels and uses the HV7355 in parallel mode. The second electronics combines TX and RX and is therefore suitable for pulse echo operation. It uses the HV7355 in serial mode as there are not enough pins available to connect the pulsers in parallel mode in conjunction with the ADCs. The maximum excitation voltage supported is 150 V and all pulsers share a common supply rail.

Both electronics use the Zynq 7010 system on chip (SoC) (Xilinx, San Jose, CA, USA). This IC combines an FPGA and a micro processor in a single package connected by a high speed bus. The embedded FPGA allows implementing a large number of serial interfaces supplementing the micro processor, only limited

by the total number of 100 available pins. The embedded micro processor is a Dual-core ARM Cortex-A9 running at up to 866 MHz.

The SoC is not directly designed into the two electronics but a ready made module (MicroZed, Avnet, Phoenix AZ, USA) is used that contains both this SoC and an Ethernet interface. Both electronics are directly attached at the back of the waveguide so that no cabling per transducer is needed. The only connections necessary are the power supply and an Ethernet connection. This allows cable lengths of up to 100 m to the controlling PC [55].

4.3.1 TX only electronics

The TX-only electronics implements the two-stage excitation scheme (Figure 4.2) and uses 64 of the 100 available pins to control eight HV7355 pulsers. This means for each channel, there is a dedicated connection from the FPGA to a single pulser channel. The electronics was developed during the Master's thesis of Dominik Großkurth [56] and already successfully used in two publications [1, 2].

The FPGA runs at 71.43 MHz, providing an angular resolution of 0.128° for a 40 kHz excitation. When exciting at 200 kHz, a phase resolution of still 0.642° is possible.

The PCB containing these electronics measures 100 mm × 100 mm. This matches nicely with both waveguide designs that have a similar dimensio at the side of the transducers. The MicroZed-board is attached to the top side of the PCB while the connectors to the transducers on the waveguide are located at the bottom (Figure 4.4).

The device is programmed to receive control packets on the Ethernet connection that contains a table of delays per channel and the number of burst cycles. A custom PC-based application calculates the delays based on the two steering angles AZ_s and EL_s using either method described in section 2.9.

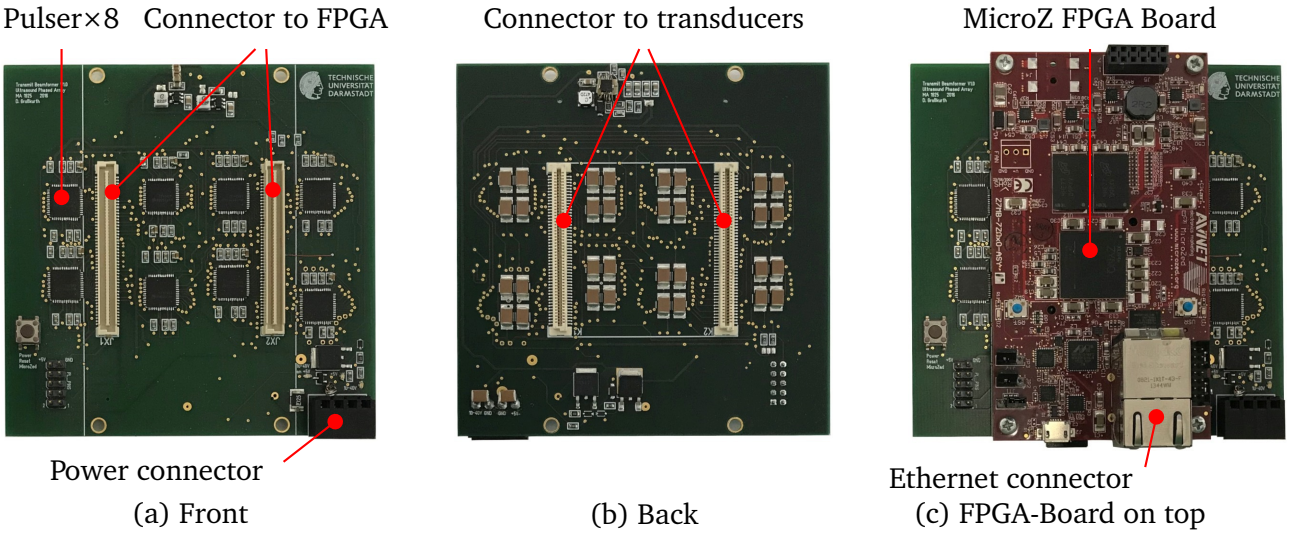

Figure 4.4.: TX-only electronics developed during the Master's Thesis of Dominik Großkurth. It uses eight HV7355 pulsers connected to the FPGA using one data line per channel (a). The board connects to the interposer PCB of the transducers (b). The MicroZed FPGA-board (red) is attached to the top (c) and supplied by a base board using the same power connector as the pulsers (a).

4.3.2 Combined RX/TX-electronics

The combined TX/RX electronics implements the two stage excitation scheme combined with RX for all 64 channels. This electronics was developed during the Master's thesis of Jan Hinrichs [57].

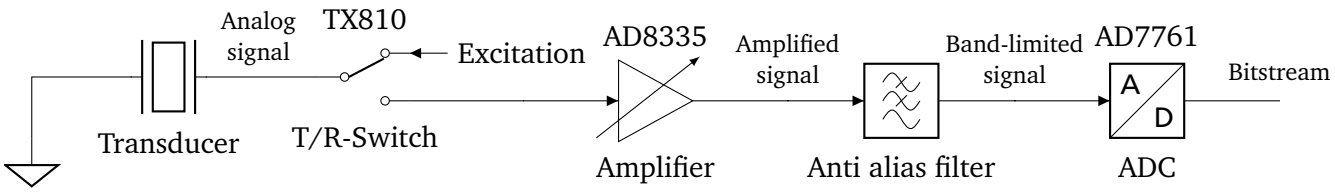

Figure 4.5.: The receiver stage consists of a T/R-Switch, a variable gain amplifier, an anti-alias-filter and an analog-to-digital converter

All components described in section 4.2 are present (Figure 4.5). A TX/RX switch (TX810, Texas Instruments, Dallas, TX, USA) disconnects the RX stage while the TX stage generates high excitation voltages. The TX810 features eight channels, so eight devices are used. As a VGA, the AD8335 (Analog Devices, Norwood, MA, USA) is used. This device features only four channels, so 16 devices are used. A differential analog low pass filter is used as an anti-alias filter for the ADC, consisting of two resistors and one capacitor. The AD7761 (also Analog Devices, Norwood, MA, USA) is used as ADC. This device is an eight-öchannel, delta sigma ADC simultaneously sampling at 256 kSps. The analog bandwidth of the device is 110.8 kHz. Compared to a signal frequency of 40 kHz, this is an oversampling by a factor of 1.375. The digitized signals are then send to a PC using an Ethernet connection.

Due to the higher component count, the dimensions of the TX/RX electronics of 120 mm × 120 mm are slightly larger than the TX-only electronics. Otherwise, the concept of directly attaching the electronics to the waveguide stays the same (Figure 4.6). Additionally, a trigger-out signal is provided to synchronize other measurement equipment such as oscilloscopes to the pulse-echo process. Further, a trigger-in allows the device to stay in an armed mode and only starts sending when triggered by other equipment.

The complete electronics including over 1000 passive components was hand soldered. During the initial operation, the significant number of 21 out of 64 receive channels where identified as none working (Figure 4.7). These channels provide no or only corrupt A-scans. Potential reasons are non-proper solder joints or components damaged during the manual soldering process. At the time of writing this thesis, October 2018, a professional assembled batch of electronics is ordered, however, not yet available for experiments. Instead, the defunct A-scans are omitted in the delay and sum calculations. The effect of the missing channels is characterized in section 5.2.

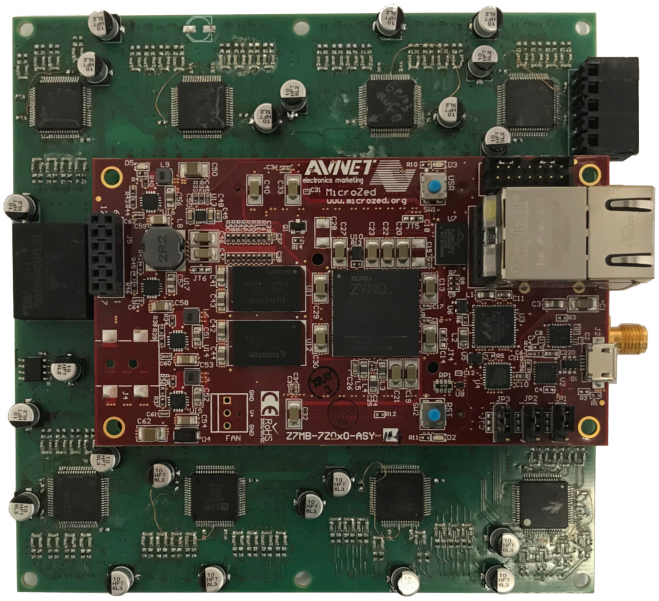

Figure 4.6.: Combined TX/RX electronics developed during the Master's thesis of Jan Hinrichs [57]. The electronics is contained on a square shaped PCB, dimensions 120 mm × 120 mm. The red PCB on top is again the MicroZed board by Avnet. Connectors to the transducers are located at the bottom side (not shown).

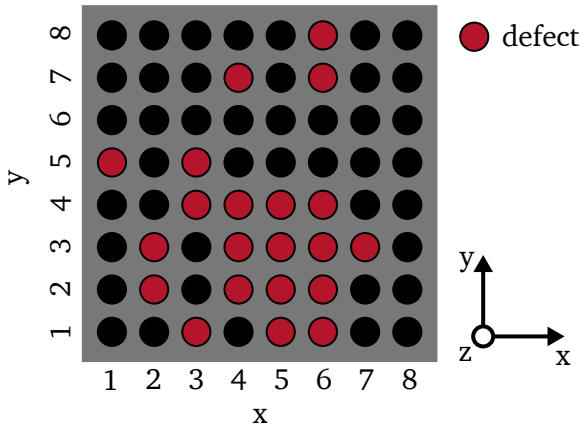

Figure 4.7.: Defect RX channels in the combined TX/RX electronics. The affected channels provide no proper A-scan. The TX functionality is not affected and works properly on all 64 channels.

4.3.3 Signal processing

The signal processing takes place on a conventional PC (Core i5 2400, Intel Corporation, Santa Clara, CA, USA, released 2011) equipped with a mid class GPU (Geforce 1050 Ti, NVIDIA Corporation, Santa Clara, CA, USA, released 2016). All signal processing algorithms are implemented in a custom, C++-based application. This application was developed during the Master's thesis of Gianni Allevato [58].

All algorithms utilize the computing capabilities of the GPU by using OpenGL compute shaders. These are small routines that run directly on the GPU, several hundred or even thousand times in parallel. This allows instantaneous processing and visualization of the received data. During the experiments conducted in this thesis, the signal processing is faster than the data acquisition as the system needs to wait for echoes, depending on the configured maximum distance. An A-scan view, plotting the raw data for each channel and the sum signal is available as well a brightness scan (B-scan).

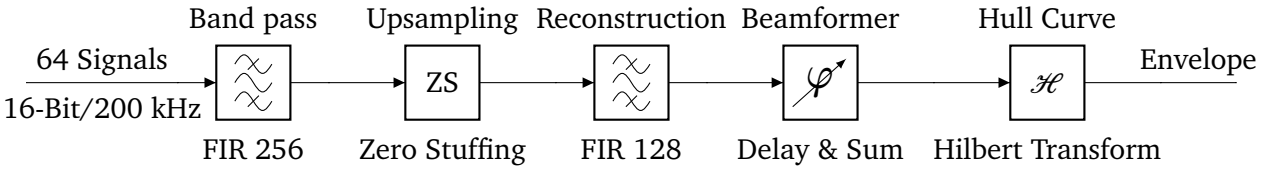

Figure 4.8.: Signal processing chain (a) and resulting signal (b)

The signal processing chain consists of several blocks (Figure 4.8), starting with a band pass filter, limiting the raw received signal to the primary frequency of 40 kHz. The filter is implemented as a finite impulse response (FIR)-filter of order 256 due to the linear phase response. The next step is an upsampling by the factor of 25 using the method of zero stuffing. This method scales the amplitudes of the actual samples by a factor of 25 and inserts 24 zeros between them. A subsequent reconstruction filter distributes the signal energy across all samples while maintaining the original amplitude shape. This upsampling is necessary as the raw data from the RX-electronics provides only few data points per signal period and beam forming can only be evaluated at the discrete data points. The delay and sum beam forming methods described in section 2.9 is further implemented, providing spatial filtering. The last block is the extraction of the hull curve using the absolute value of the analytical signal, reconstructed from the real signal using the Hilbert transform.

The signal processing system is the last block needed to bring the phased array into operation. The next step is a thorough system characterization.

5 System characterization

All characterizations in this chapter are performed in the acoustic anechoic chamber of the measurement and sensor technology group at the Technische Universität Darmstadt. The chamber has been originally designed for the audible frequency range and is, thus, equipped with sound absorbing wedges. The absorbers are wedge-shaped and made of synthetic mineral fibers, covering all four walls as well as on the bottom and the ceiling. An acoustic transparent floor made from wire mesh allows people to walk above the bottom wedges.

The chamber is equipped with a motorized goniometer capable of rotating a device under test (DUT) around two axes. Further, a motorized linear rail positions either a microphone or a second DUT in front of the primary DUT in a range of 0 m to 6 m (Figure 5.1). This allows positioning the microphone or the secondary DUT in a volume of a hemisphere with a radius of up to 6 m in front of the primary DUT. The goniometer consists of commercial motion components that allow angular resolutions up to 60 µrad and resolutions along the z-axis of up to 0.2 mm (Table 5.1).

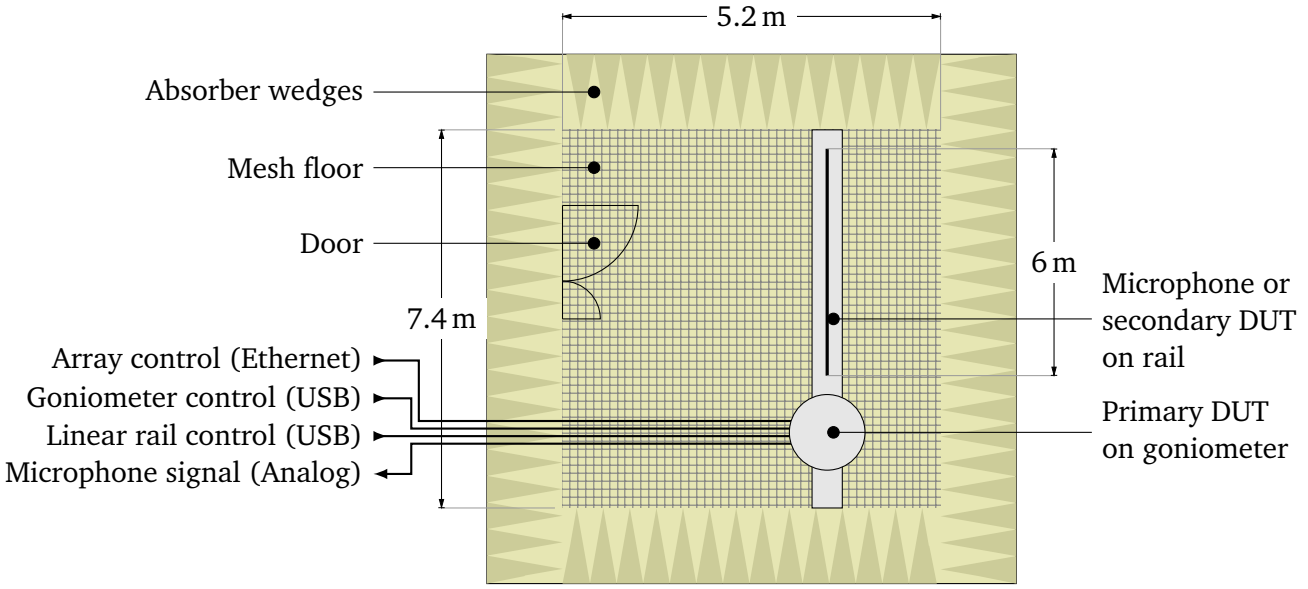

Figure 5.1.: Overview of anechoic chamber. The anechoic chamber is equipped with a goniometer capable of rotating a device under test (DUT) around two axis and a microphone or second DUT along a beam in front of the primary DUT. Electrical connections are passed to the outside next to the door on the left side.

Table 5.1.: Motion components and controllers used in the acoustic goniometer.

Axis	Manufacturer	Product	Controller	Repeatability	Source
α	PI Karlsruhe	M-061.2S	C-663.11	50 µrad	[59]
β	PI Karlsruhe	M-062.2S	C-663.11	60 µrad	[59]
z	Isel	LEZ 1 L5998 mm	IT116 Flash	0.2 mm	[60]

When performing a microphone measurement, a calibrated microphone(TYPE 4138, Bruel & Kjær, Nærum, Denmark), is used [61]. The microphone requires a primary amplifier (TYPE 2670) and a power supply (TYPE 2829), both Bruel & Kjær as well. Data acquisition is done using a 24-bit oscilloscope (type NI PXI-5922, National Instruments, Austin, TX, USA) [62]. Motion- and array control is done using a regular PC running an application developed using LabVIEW, National Instruments. The overall noise level is determined to 60 dB SPL while the overall amplitude uncertainty is determined to ± 1 dB SPL.

The kinematic structure of the goniometer does not match any coordinate systems introduced in section 2.1 (Figure 5.2). Therefore, the axes are labeled α and β. The relation between the axis coordinate system and Cartesian coordinates is given by

$$\begin{pmatrix} x \\ y \\ z \end{pmatrix} = z \begin{pmatrix} -\cos(\alpha)\sin(\beta) \\ \sin(\alpha)\sin(\beta) \\ \cos(\beta) \end{pmatrix}. \tag{5.1}$$

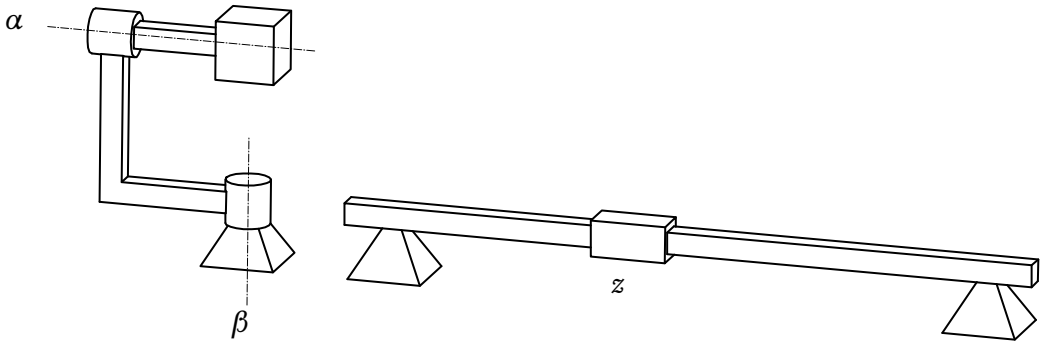

Figure 5.2.: Kinematic structure of the goniometer. Two rotational axes α and β rotate a primary DUT. A second DUT or microphone is positioned in front of the primary DUT using a linear rail.

5.1 TX Characterization

The first step in the system characterization is the comparison of emitted ultrasound against the analytical models described in chapter 2. Different combinations of waveguides and electronics are mounted into the goniometer as primary DUT. The goniometer orients the DUT and positions the microphone according to a predefined list of positions, sampling the volume. At each position, the array emits a burst of 40 cycles. The microphone receives the bursts and from that measurement, the sound pressure level is calculated.

First, a 2D slice of the sound field is sampled. The resolution is set to 10 mm in z-direction and 1° in $AZ = \vartheta$-direction. This is done for the combination of the equal-length waveguide combined with the parallel electronics for steering angles of $AZ = \vartheta_s = 0°$ and $AZ = \vartheta_s = -45°$ (Figure 5.3). Both

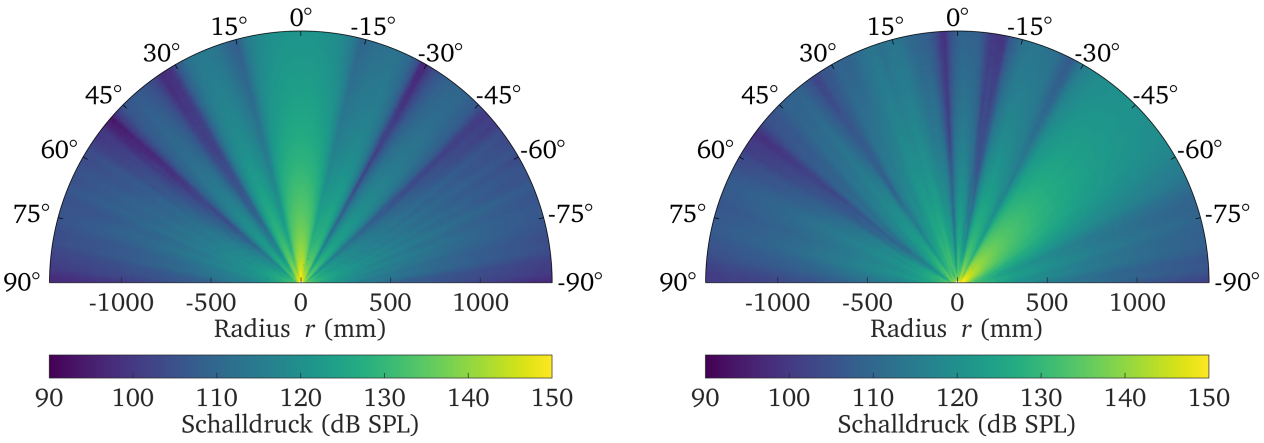

(a) $AZ = \vartheta_s = 0°$.

(b) $AZ = \vartheta_s = -45°$.

Figure 5.3.: Slice of a volumetric measurement of an equal length waveguide combined with the parallel electronics, sending in both $AZ_s = \vartheta_s = 0°$ and $AZ_s = \vartheta_s = -45°$ direction, respectively. No averaging was used during the measurement. False color plot of sound pressure level (SPL) as function of position. Both measurements show a distinct main lobe in the respective direction and a monotonic decrease in sound pressure in r-direction as expected in the far field.

measurements show a distinct main lobe in the steered direction of $\vartheta_s = 0°$ and $\vartheta_s = -45°$. The main lobe is surrounded by several side lobes as expected from the calculated radiation pattern (Figure 3.2). For each direction, the received amplitude monotonically decreases with increased radius as expected for any sound field caused by a transducer in the far field. Sound pressure levels (SPL) up to 150 dB occur close to the array aperture in the main steering direction. The ripples visible in both third main lobes to the left and to the right are caused by the finite rigid baffle of $\varnothing = 250$ mm. Sound waves traveling along the rigid baffle are reflected by the abrupt transition to free space. Although visually pleasing, visualizing the sound pressure using a color map makes quantitative analysis hard.

Radiation patterns

Radiation patterns show the sound pressure as a function of angle, sampled on a fixed radius of $r = 300\,\text{mm}$ (Figure 5.4). The first series of radiation pattern compares the two different electronics using

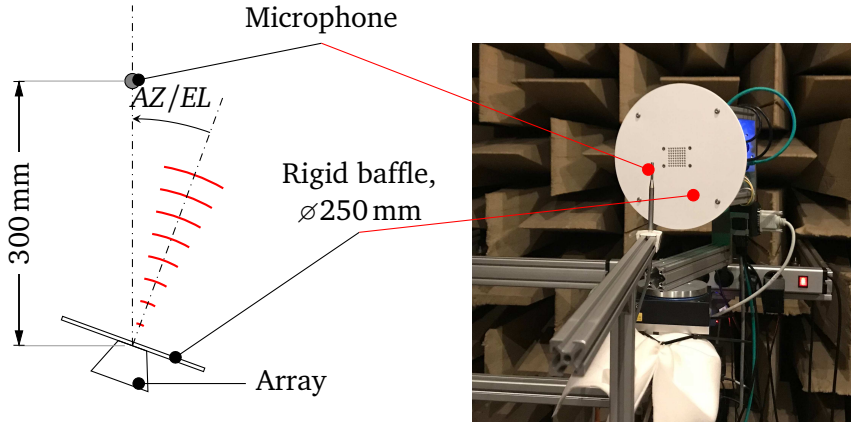

Figure 5.4.: Schematic view (a) and photo (b) of the experimental setup for obtaining the radiation pattern. The microphone is positioned at a fixed distance of 300 mm. The array itself is rotated around the $AZ = \vartheta$-axis. The photo shows the array rotated by 20°.

an equal-length waveguide. The two angles of $AZ = \vartheta_s = 0°$ and $AZ = \vartheta_s = 45°$ are used (Figure 5.5 and Figure 5.6). Both measurements show a distinct main lobe that matches the configured direction. Also, in both cases, the main lobe is slightly wider than expected and the first side lobe is higher than expected. A possible reason for this difference are manufacturing tolerances of the transducers that do not guarantee a uniform amplitude distribution over the array aperture. Another reason are mechanically imperfect mounted transducers due to the manual assembly of the waveguide.

Compensation of channel lengths

One key question is the feasibility of the compensation of different channel lengths in the free form waveguide model (section 3.3). A symmetric free form waveguide is equipped with the TX only electronics (subsection 4.3.1) and the radiation pattern is again obtained for both $AZ = \vartheta = 0°$ and $AZ = \vartheta = 45°$ with compensation enabled and disabled (Figure 5.7 and Figure 5.8).

Both measurements show a pronounced main lobe at an amplitude of about 135 dB matching the steering direction when the compensation is enabled but only a diffuse main lobe and no pronounced side lobes when the compensation is disabled. Also, the height of the main lobe reaches only about 123 dB when compensation is disabled. Both measurements show that the compensation of different channel lengths using delays during sending is feasible.

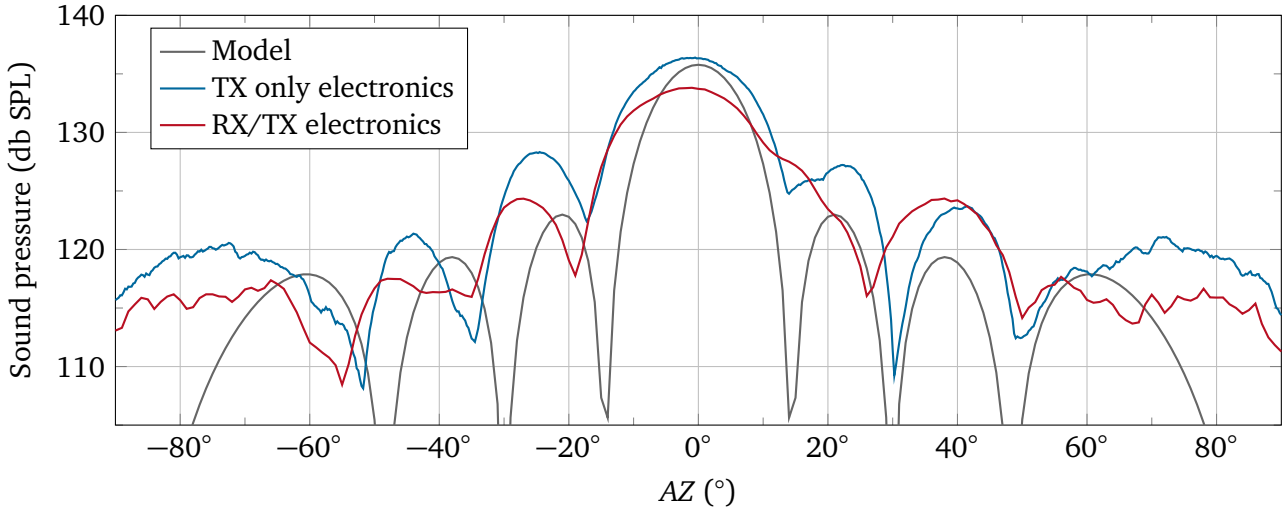

Figure 5.5.: Comparison of model and measurement of an equal length waveguide equipped with the TX-only electronics (subsection 4.3.1) and the combined TX/RX electronics (subsection 4.3.2) sending bursts in the direction of $AZ = EL = 0°$. Both configurations lead to similar results: A distinct main lobe around 0° is visible. The main lobe is slightly asymmetric and wider compared to the model. Therefore the measured minima do not match the calculated minima.

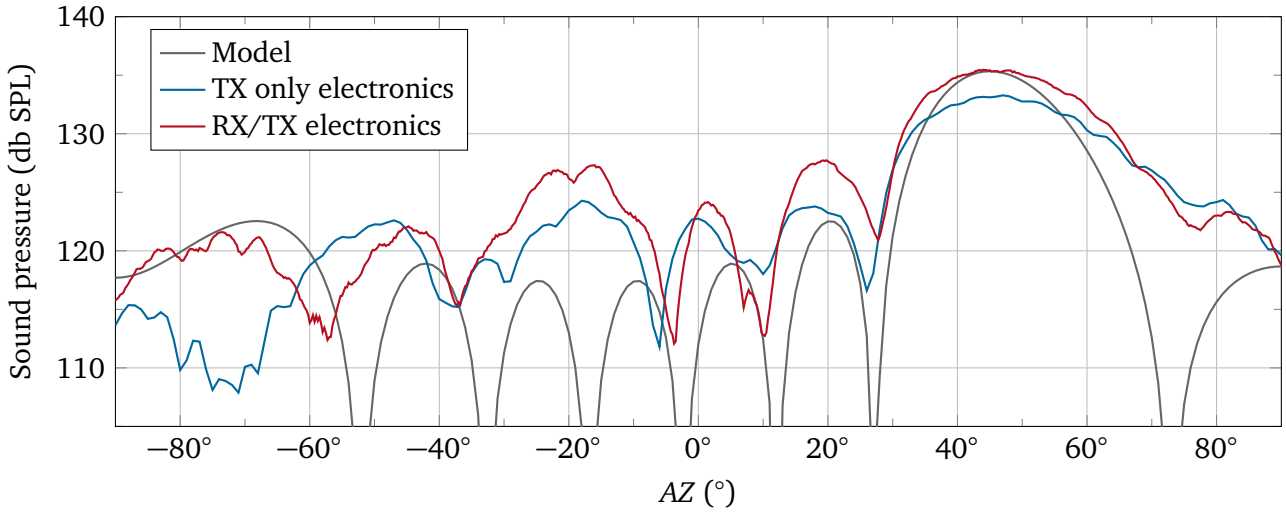

Figure 5.6.: Comparison of model and measurement of an equal-length waveguide equipped with the TX-only electronics (subsection 4.3.1) and the TX/RX electronics (subsection 4.3.2) sending bursts in the direction of $AZ = EL = 45°$. Again, both configurations lead to similar results: A distinct main lobe around 45° is visible. The expected main lobe is asymmetric, however the asymmetry is more pronounced in both measurements. Again, the measured minima do not exactly match the calculated minima.

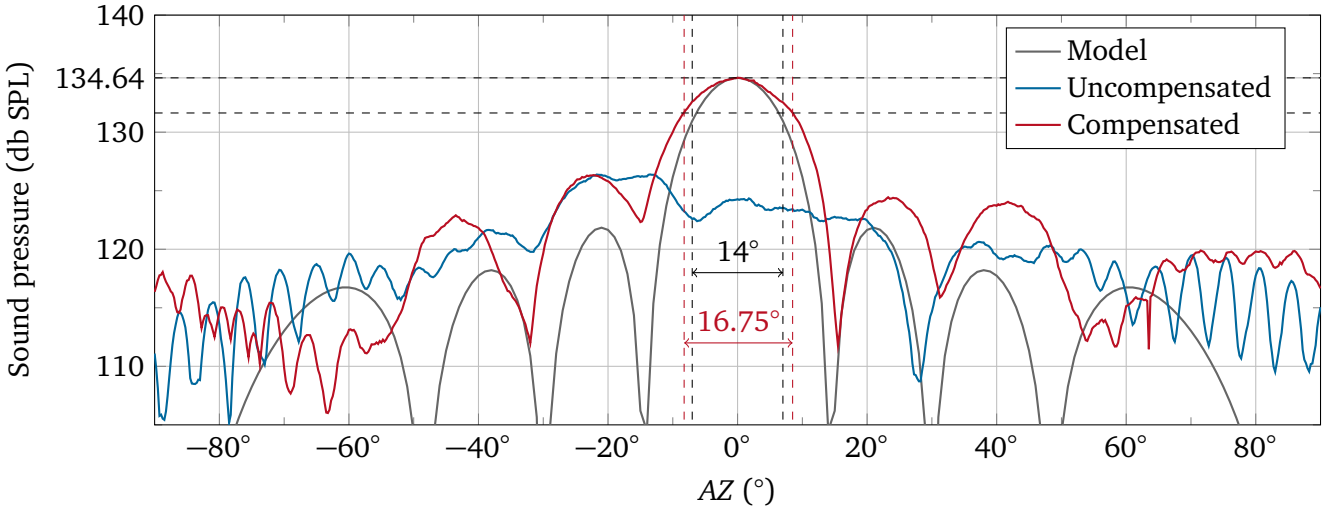

Figure 5.7.: Array consisting of the free form waveguide model and the parallel electronics configured to send in $AZ = \vartheta = 0°$-direction. Comparison of compensation of the channel lengths enabled and disabled. With compensation enabled, a distinct main lobe at the expected angle of 0° is visible. The main lobe again is slightly wider than in the model and again, the side lobes are slightly higher. Without the compensation, only a diffuse maximum at about 19° is visible that matches the first side lobe to the left of the compensated configuration in both shape and amplitude.

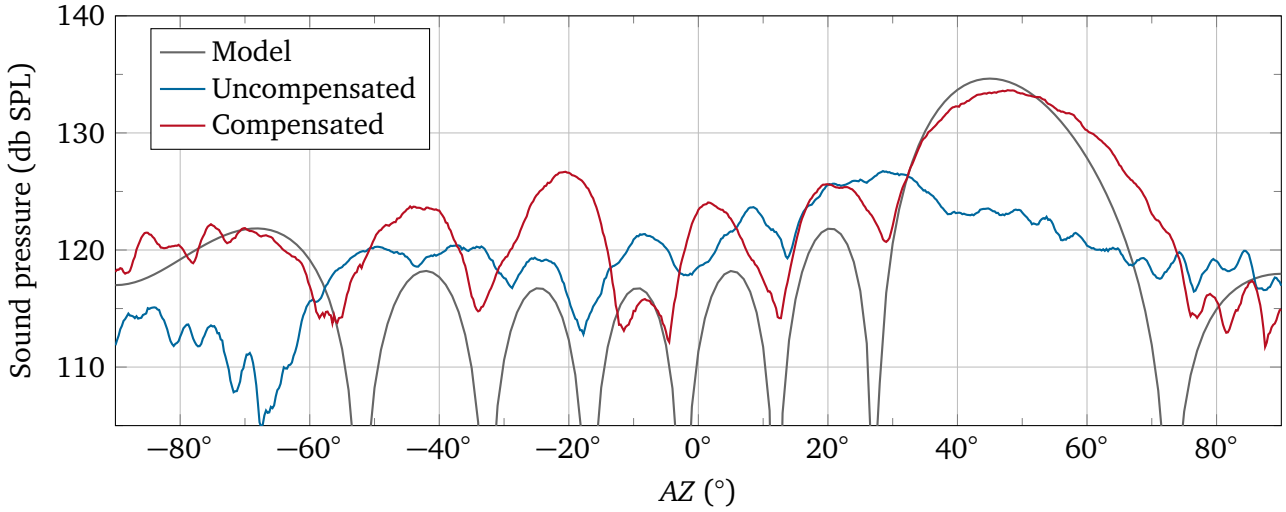

Figure 5.8.: Array consisting of the free form waveguide model and the parallel electronics configured to send in $AZ = \vartheta = 45°$-direction. Comparison of compensation of the channel lengths enabled and disabled. With compensation enabled, a distinct main lobe at 47° is visible. The main lobe again is slightly wider than the model and again, the side lobes are slightly higher. Without the compensation, only a diffuse maximum at about 38° is visible.

5.2 Receive characterization

The receive characterization verifies that the angular filter behaves as described in section 2.10. A known ultrasound sender is used as secondary DUT(MA40S4S, Murata Seisakusho, Kyōto, Japan, [17]). The sender is positioned in front of the array at a distance of 3 m (Figure 5.9). The transducer is excited using a signal generator (type 33500B, Keysight, Santa Rosa, CA, USA), using a continuous sinusoidal signal of $V_{pp} = 10\,V$.

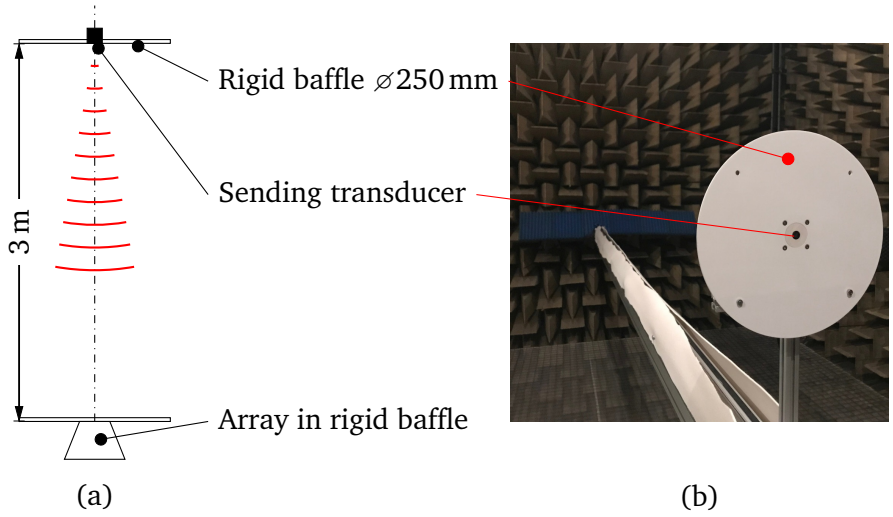

Figure 5.9.: Experimental setup for obtaining the spatial filter characteristic. An ultrasound transducer is positioned in front of the array at a distance of 3 m and excited using a continuous wave signal. The array is configured to receive continuously.

The received signals are delayed and summed using steering matrices for all combinations of $AZ = -50°$ to 50° and $EL = -50°$ to 50° in steps of 2°. The maximum amplitude of each signal is then plotted as a 2D-function of *AZ* and *EL*.

The expected spatial filter characteristic for an ideal array is identical to the radiation pattern when sending. However, as the characterization of the receiving electronics showed (subsection 4.3.2), 21 receive channels are not working. These channels are missing in the calculation of the DS-signal. The expected receiving characteristic is therefore different to the radiation pattern, however, it can be estimated by modeling the array using Dirac pulses only for the working channels.

The ideal array spatial filter is a symmetric cross like shape made up of the main lobe and side lobes centered around $AZ = EL = 0°$ [Figure 5.10 (a)]. The expected spatial filter, missing the defect channels, is no longer symmetric as the shape of the defect channels is also not symmetric [Figure 5.10 (b)]. The shape of the main lobes is no longer a regular pattern. The actual measurement shows an irregular pattern as well, partially matching the pattern of the simulation. The maximum of the main lobe is slightly shifted towards the positive *EL*-direction and *AZ*-direction.

A slice of these plots at $EL = 0°$ is further investigated (Figure 5.11). First, the ideal receive characteristics is compared to a calculated receive characteristic missing the defect channels. The main lobe maximum is reduced by 3.5 dB while the side lobes are larger by 1.73 dB. The minimum around −30° is less pronounced and increased by 10.2 dB. The shape of the data points, however, suggests a lower value between the data point at −30° and −28°. The 3 dB-width of the main lobe is reduced from 14° down to 12°, while the width of the side lobes increase from 8° to 10°. The overall shape shows a scaling down

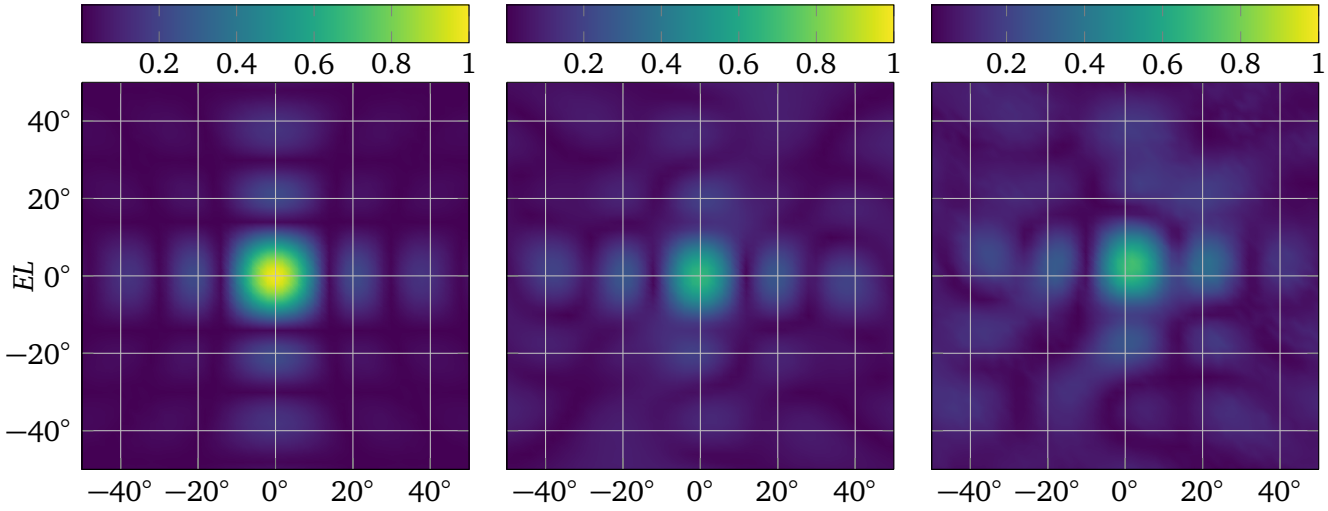

(a) Model full array *AZ* (b) Model missing channels *AZ* (c) Measurement *AZ*

Figure 5.10.: Spatial filter characteristics for an ideal array of 8×8 elements spaced $\lambda/2$ apart (a), expected filter when omitting the missing channels (b) and measured filter characteristics (c).

by about 2°. It is expected that the defect channels result in a less pronounced spatial filter behaviour because the main lobe is reduced while the side lobes are increased.

Comparing the actual measurements against the simulation, while taking the defect channels into account, shows an identical main lobe width of 12° (Figure 5.11). In this picture, the curve of the actual measurement is shifted by −2° to compensate for the shift already noticed in Figure 5.10. This makes comparing the width of the side lobes and the distance between the minima easier. After the shift, the positions of the minima match in the measurement match the simulation taking into account the defect channels. As expected, the overall curve shape is asymmetric. In the negative sector, the measured amplitudes of both sidelobes almost match the simulation by a difference of only 0.6 dB. The minima are less pronounced compared to the simulation. The first minimum is higher by about 7 dB while the second minimum is still about 6 dB higher. In the positive sector, the first minimum is more increased by 24 dB and only slightly below the first side lobe amplitude. However, the shape suggests a lower value between the data points at 10° and 12°. The first side lobe is only slightly increased by 2.32 dB. The second minimum is reduced by −5.34 dB while the second side lobe is reduced by −1.84 dB.

There are two possible reasons for these differences. The effect of the waveguide was not included in both simulations and the transducers were not binned. As the transducers are subject to manufacturing tolerances, they carry a slight difference in sensitivity that is not included in the model either. Further measurement are necessary as soon as an RX electronics is available where all receive channels are working properly.

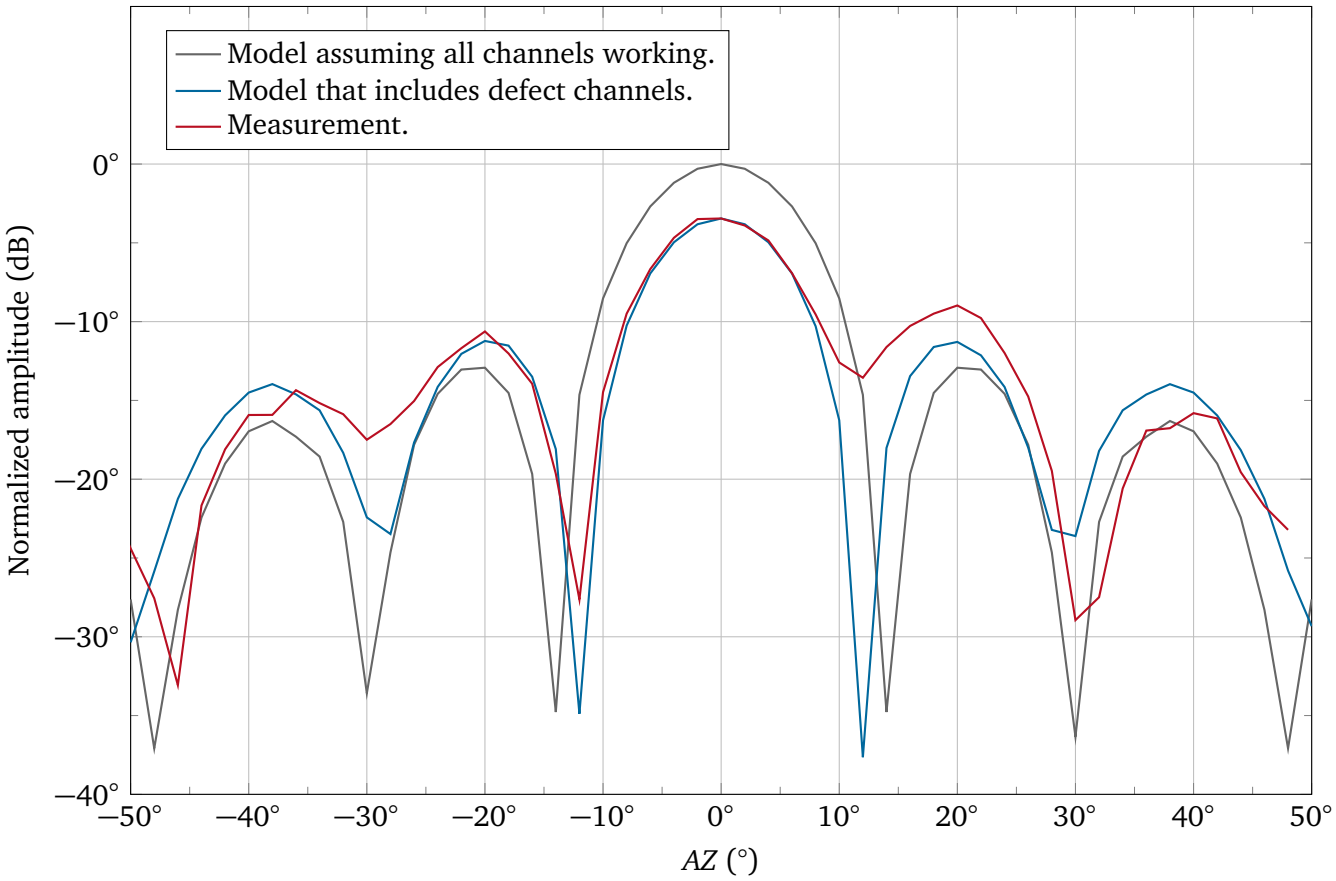

Figure 5.11.: Comparison of ideal model, model omitting defect channels and actual measurement. The reduced model is normalized to the ideal model to reflect the expected loss in amplitude and the measurement is normalized to the defect model.

5.3 Pulse/Echo characterization and range finding

After the characterization of the individual building blocks, the complete sequence of the pulse echo operation is characterized. Several experiments are conducted. Defined objects are placed at distinct positions in front of the array. The object size and position detected is compared to the actual setup.

The signal processing chain is configured according to Table 5.2 if not otherwise mentioned. Compared to normal operation, the VGA is set to relatively high fixed gain of 46 dB that does not increase with increased time, and, thus, distance. This is done to see the loss in amplitude in the received A-scan.

The mapping of amplitude values to the color table is different for each image and given below the plot.

Table 5.2.: System parameters used during the pulse echo characterization.

Parameter	Value	Comment
ROI		
Vertical field of view	−50°:2°:50°	51 measurements
Horizontal field of view	−50°:2°:50°	51 measurements
Range	7.09 m	8000 samples
Excitation		
Signal frequency	40 kHz	
Signal shape	Square wave unipolar	
Pulslänge	40 Perioden	
VGA		
Base gain	46 dB	
gain incremement	0 dB/ms	
ADC		
Sampling rate	200 kSps	
Amplitude resolution	16 Bit	
Voltage reference	5 V	
Band-pass filter		
Filter order	255	
Lower cut-off frequency	39 kHz	
Upper cut-off frequency	41 kHz	
Interpolation		
Upsampling factor	25	
Order of reconstruction filter	127	
Cut cut-off frequency of reconstruction	100 kHz	
Envelope		
Order of Hilbert-filter	201	
Decimation factor	25	200 kHz sampling

5.3.1 Empty measurement

Although the experiments take place in an anechoic chamber where the walls are equipped with sound absorbing wedges, several mechanical features exist that might be detectable. Especially sphere- or cylindrical-shaped objects cause visible echoes as these geometries do not need proper alignment to the phased array. Care has been taken to cover all acoustically visible features by acoustic absorber foam. However, there are still several echoes that are easily mapped to existing structures within the chamber, such as poles in the door frame or the mounting of the goniometer (Figure 5.12).

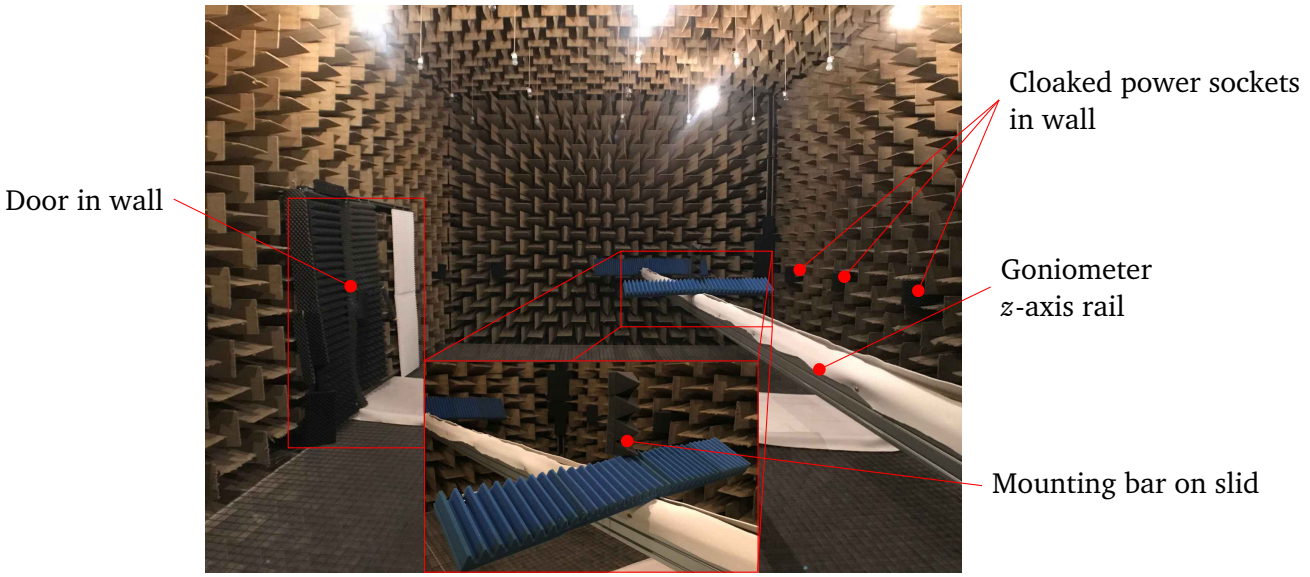

Figure 5.12.: Photo of the anechoic chamber. The frame of the door as well as all power sockets within the field of view of the array are coated using absorber foam (black: aixFoam SH003, Schaumstoffe Helgers GmbH, Eschweiler, Germany, blue: Classic Wedge, EQ Acoustics, Stockbridge, United Kingdom). The z-axis rail is covered to the left and to the right using sound absorbing felt (Designfilz, M&K Filze GmbH, Spalt, Germany).

The door, the mounting bar for the second DUT as well as the walls of the anechoic chamber are still visible (Figure 5.13). The amplitudes of these objects are below the amplitudes of actual objects used in the later experiments. When adopting the brightness to the echo amplitudes caused by the objects to detect, the features of the room are still visible, but easily distinguishable from the echoes of interest. Also, in a blind zone of about 1 m, no targets are detectable as the transducers ring after the switch from TX to RX and the ringing signal still received is higher than the target echoes in this area.

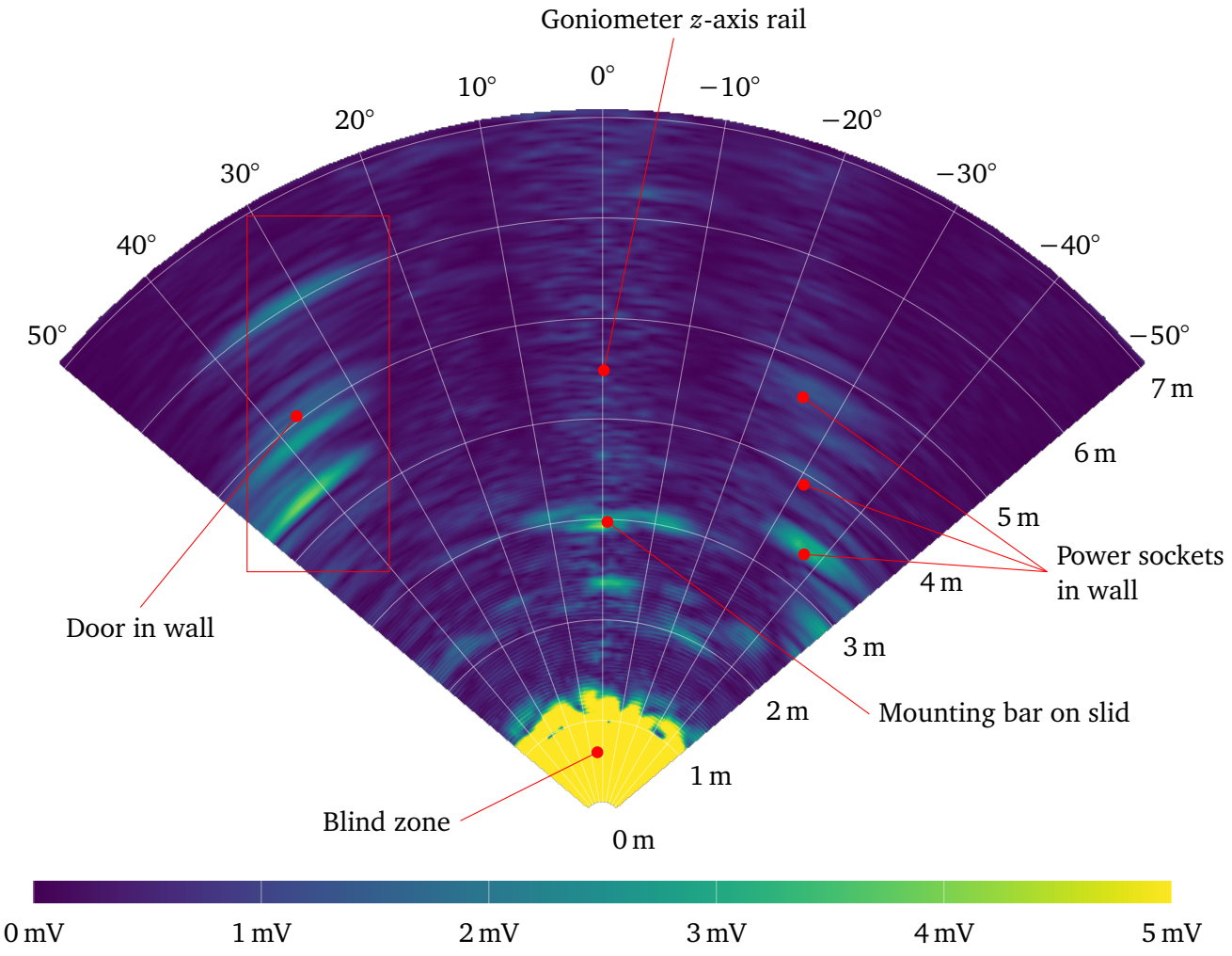

Figure 5.13.: B-scan image of the anechoic chamber. Although all mechanical features in the room were cloaked using absorbing materials, several unwanted echoes are still visible. The system suffers from a blind zone of about 1 m caused by the time needed to switch between TX and RX of the transducers.

The first series of experiments is the detection of a single sphere. The sphere is selected as test object as its cross sectional area is independent of its orientation relative to the array. The expected echo strength is lower than for most objects of a similar size as most of the acoustic wave that hits the cross sectional area of the sphere is scattered into other directions. The sphere is therefore rather difficult to detect and if its detection is possible, the results are transferable to objects of comparable size but different shape. The amplitude received also depends on the acoustic mismatch between air and material of the sphere. Here, only materials with an acoustic impedance significantly larger than air are used so total reflection and no penetration of the sphere is assumed.

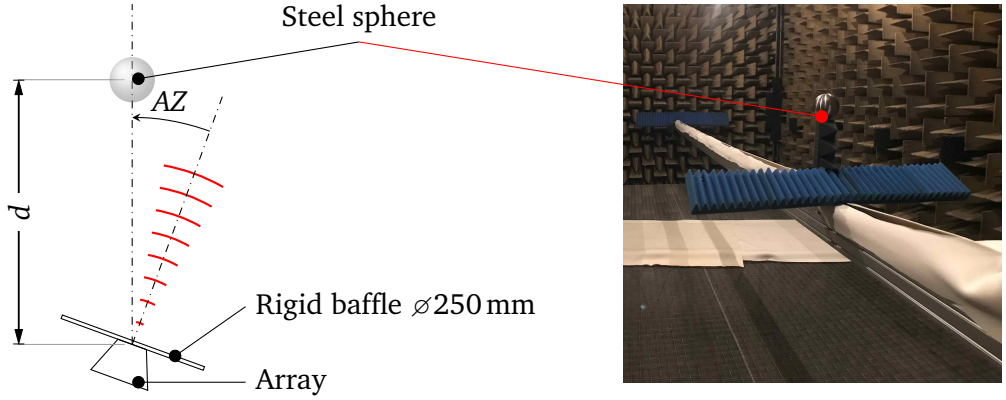

Figure 5.14.: Experimental setup for detection of a single object for different directions and distances, schematic view (a) and photo (b). A steel sphere is mounted on the slid of the z-axis that is used to change the distance to the array. The goniometer rotates the phased array so that the direction of the sphere relative to the array changes.

A hollow steel sphere of $\varnothing = 100\,\text{mm}$ is mounted on the slid of the z-axis (Figure 5.14). The height is adjusted so that the center of the sphere aligns with the center of the array aperture. By rotating the array in the goniometer and moving the sphere along the z-axis, the sphere can be moved in the coordinate system of the array. The goal of this series of measurements is the relationship of the echo amplitude as a function of direction and distance.

Varying the object direction

The position of the sphere is varied in the AZ/EL-cordinate system. The first series varies the AZ-angle in a range of $-50°$ to $50°$ in steps of $5°$ while keeping the EL angle fixed to $0°$. The second series varies the EL-angle over the same range while keeping the AZ angle fixed at $0°$. This is the equivalent to positioning the sphere in front of the array along a cross shape. The average value of the maximum amplitudes for each measurement is determined and plotted as function of either AZ or EL (Figure 5.15).

The measurement uncertainty is $\pm 27\,\text{mV}$ for a normal distribution, an expansion factor of $k = 2$ (95 % confidence interval) and $N = 5$ samples [63].

Both data series show a similar shape: The maximum amplitude decreases from above 1.3 V when the sphere is located directly in front of the array to below 1 V for an angle of 50°. The slope of decrease is

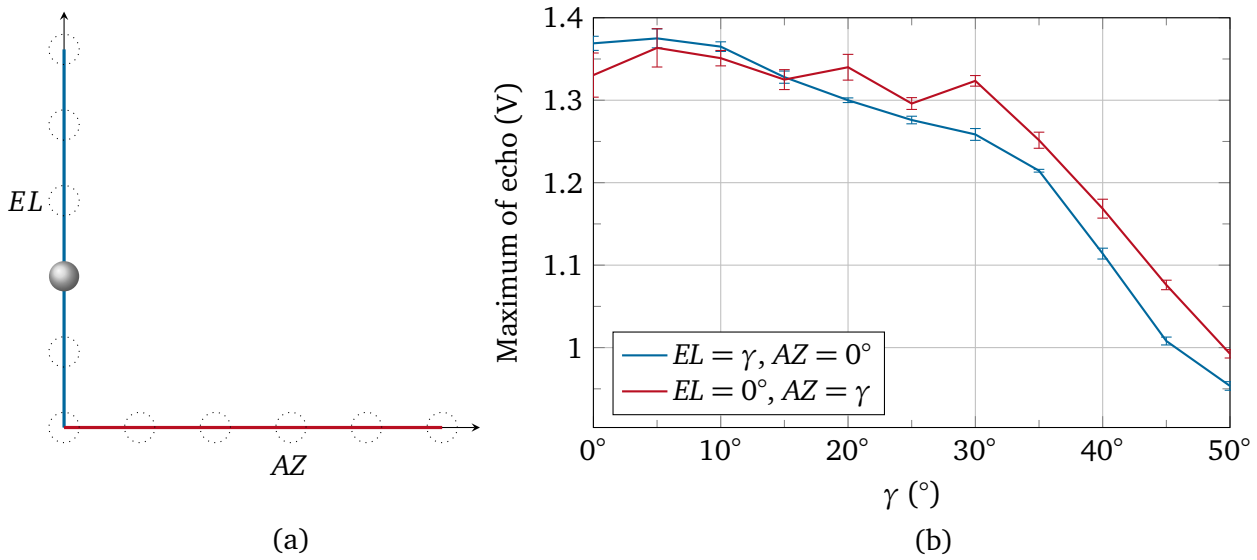

(a) (b)

Figure 5.15.: Single sphere positioned along the AZ- and EZ-axis (a) and received amplitudes (b) at a fixed distance of 3 m. In both directions, the amplitude decreases with increasing angle.

not constant but follows roughly a cosine shape. The reason for this behaviour is the width of the main lobe that increases with higher steering angles and, thus, distributes the energy over a wider spatial angle (section 5.1). The amount of acoustic energy that hits the sphere surface, and, thus, is reflected back to the array, is decreased.

During the measurement, an interesting effect happened: The sphere is positioned by rotating the array, meaning the anechoic chamber including all features rotates around the array. As long as the walls perfectly absorb any acoustic energy emitted by the array, this is not an issue. However, the empty measurement showed that several objects are still detectable, despite being cloaked by absorbing materials.

While rotating the array, an uncloaked power socket moves into the array's field of view (Figure 5.16). The socket is approximately cube shaped with an edge length of $a = 50\,\text{mm}$. At an axis rotation angle of $AZ = -30°$, meaning the z-axis rail is oriented at 30° in the field of view of the array, the socket generates a strong echo located at a distance of about 2 m at a direction of $-55°$. This strong echo causes two kinds of visible artifacts: Matching the side lobes of the radiation pattern of the array, multiple artifacts are visible at the same distance as the power socket at about 2.25 m. A second artifact is visible at the same direction of about 55° but at twice the distance of about 4.5 m. This is caused by a double reflection between the power socket and the array's rigid baffle. The echo of the sphere is clearly distinguishable from these artifacts as the distance is different. However, the data plot of the received voltage amplitudes along the direction of the sphere of $AZ = 30°$ shows the respectable amplitude of about 0.5 V at the distance of the power socket at 2.25 m, while the sphere's echo causes a voltage of 1.32 V at a distance of 3 m (Figure 5.17).

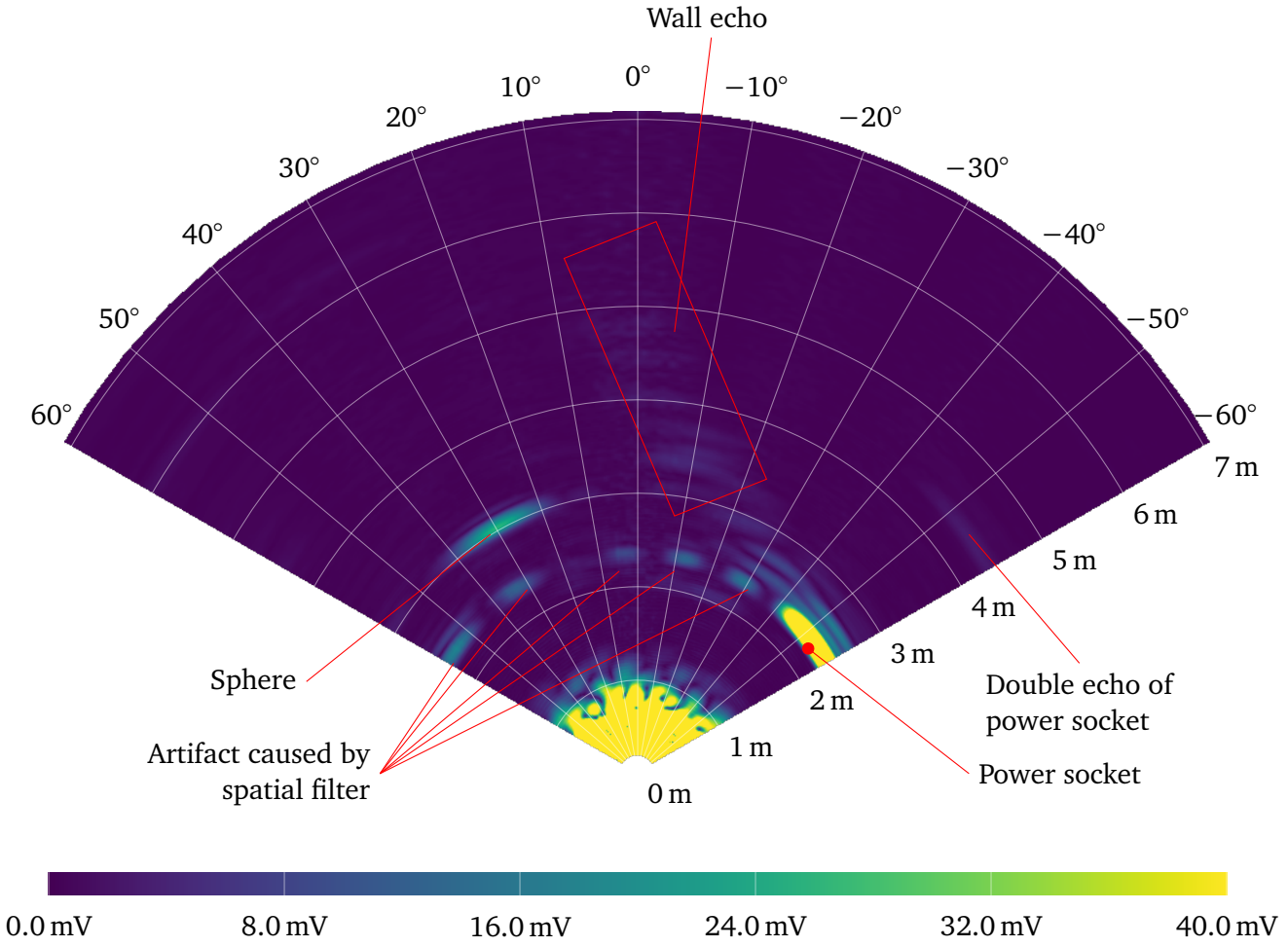

Figure 5.16.: B-Scan image of single sphere, positioned at ($r = 3\,\text{m}$, $AZ = 30°$, $EL = 0°$). Beside the echo of the sphere, a significant echo of an uncloaked power socket is visible, including artifacts matching the radiation pattern of the array. Also, a weak echo at twice the distance is visible caused by a double reflection between the socket and the array. Another very weak echo matches the wall of the anechoic chamber.

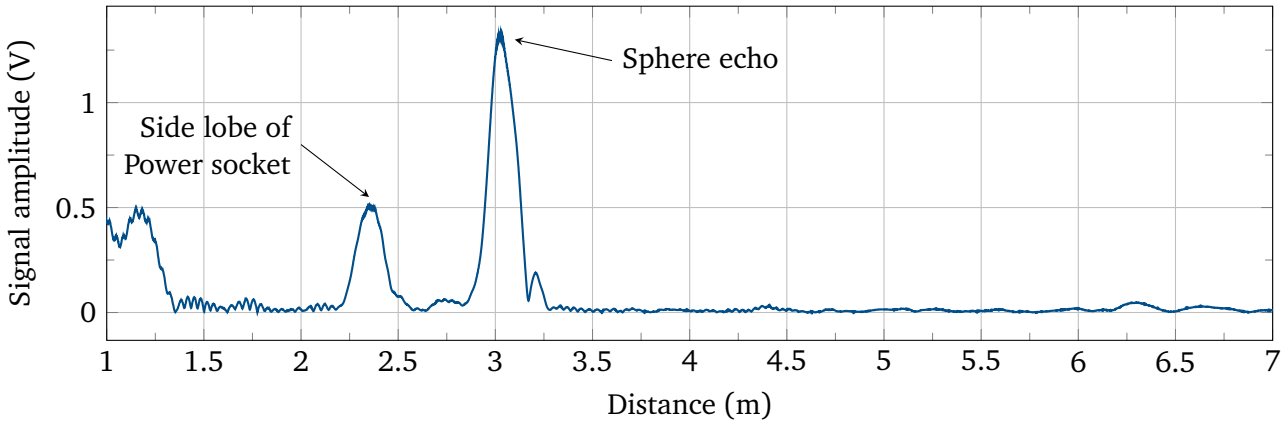

Figure 5.17.: Slice of B-scan image (Figure 5.16) in the direction of the sphere echo at an angle of 30°. Besides the echo of the sphere located at 3 m with an amplitude of 1.32 V, a second echo is visible, caused by a side lobe of the power socket at 2.25 m with an amplitude of still 0.5 V.

Varying the object's distance

It is expected that the echo received for any object decreases with larger distances. The same setup as in the previous experiment is used (Figure 5.14). Instead of the direction, the distance of the sphere is varied in a range of 1 m to 6 m in steps of 0.5 m. The measurement is done for different directions of the sphere [Figure 5.18 (a)]. Additionally, the effect of the sphere diameter is investigated by comparing the echo amplitudes of two different diameters [Figure 5.18 (b)]

The amplitude of all echoes drops exponentially with increasing distance. This drop is caused by the diffraction loss. The amount of acoustic energy that bypasses the sphere increases with increasing diameter and, thus, less acoustic energy is reflected back. The average damping is $-9\,\mathrm{dB/m}$. The uncertainty is $\pm 22\,\mathrm{mV}$ at maximum.

The base amplitude of the direction of ($AZ = 40°, EL = 40°$) is significantly lower than the other data series. This is consistent to the 2D-radiation pattern of the array [Figure 5.10 (a)] where the amplitude is significantly reduced compared to the main lobe and also to the side lobes on the AZ and EL axes.

The same behavior is true for different diameters. Both amplitudes decrease while the lager sphere of $\varnothing = 100\,\mathrm{mm}$ causes an echo generally 30 % higher compared to the smaller sphere of $\varnothing = 50\,\mathrm{mm}$. A larger difference is expected as the echo amplitude should be proportional to the cross sectional area. As the diameter of the larger sphere is twice the diameter of the smaller sphere, the cross section of the larger sphere is four times the cross section of the smaller sphere, the increase in amplitude is expected to be a factor of four. The next experiment shows the compensation of this loss in amplitude by the VGA.

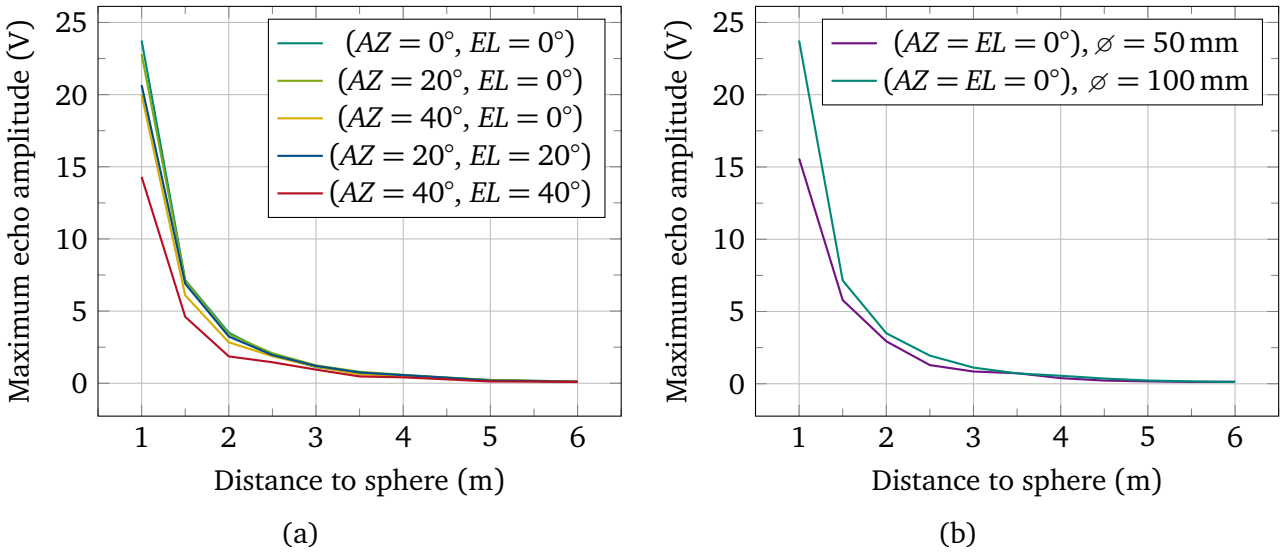

Figure 5.18.: Amplitudes of echoes of a sphere, $\varnothing = 100\,\mathrm{mm}$, as a function of distance for different directions (a) and two different sphere diameters of $\varnothing = 50\,\mathrm{mm}$ and $\varnothing = 100\,\mathrm{mm}$ (b). The decrease in amplitude with increasing distance is caused by diffraction.

Compensating amplitude loss using the VGA

The base gain of the VGA is set to 0 dB. Further, the gain increase is set to 1.5 dB/ms, i.e. 8.754 dB/m. The echo amplitudes with and without gain increase are compared to a constant base line. The goal is to keep the amplitude at a constant level and compensate for the diffraction loss (Figure 5.19).

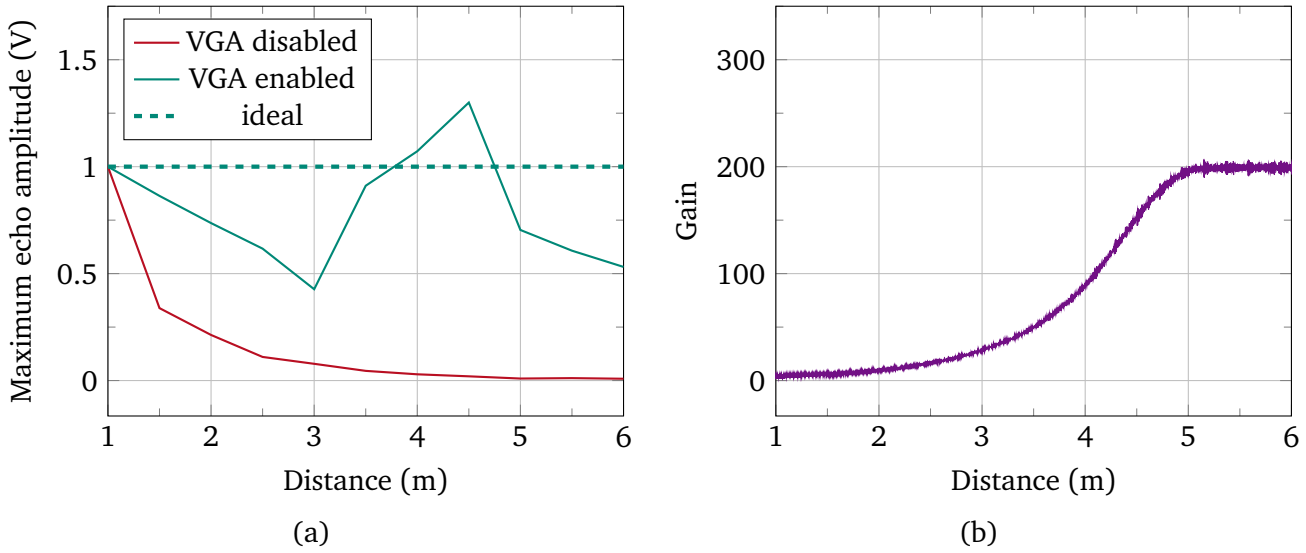

Figure 5.19.: Compensation of loss in amplitude using the VGA. An increasing gain factor (b) can only partially compensate the loss in received amplitude caused by diffraction (a). The maximum possible gain factor is 200 that is reached at a distance of 5 m.

The comparison of both curves show that the VGA can only partially compensate the drop in amplitude with increasing distance. In the range of 1 m to 3.5 m, the drop in amplitude is less pronounced compared to the uncompensated signal, however the amplitude still drops by a factor of 2 at a distance of 3 m. Between 3 m up to 4.5 m the amplitude is overcompensated up to a factor of 1.28 at 4.5 m. The VGA reaches its maximum gain at 4.5 m of $200 = 46\,\text{dB}$. From this distance on, no further compensation is possible and the amplitude decreases again. In summary, the course of the VGA amplification must be further adjusted in order to optimally compensate the diffraction loss. The signal-to-noise ratio is not improved by the increasing gain amplification, since noise is amplified as well.

The total field of view and range covered by the phased array system is composed of the results from Figure 5.15 and Figure 5.18 and the environmental noise level. When the received amplitudes fall under a certain signal-to-noise-ratio (SNR), no detection of objects is possible. The noise level here is always below the received echo maximum, therefore range finding is possible in the entire room.

5.3.3 Accuracy of position detection

The next quantity of interest is the accuracy when measuring the position of the sphere. The echo maximum is used to estimate the position of the sphere. The measurement accuracy is composed of the measurement error and the measurement uncertainty. To determine these parameters, $N = 5$ measurements are performed for each position. The measurement error is calculated with the set measurement position s_{act} and the averaged measured sphere position μ_{Pos} using the formula

$$\Delta F_{\text{Pos}} = s_{\text{act}} - \mu_{\text{Pos}}. \tag{5.2}$$

The measurement uncertainty u_{Pos} is an indicator for the variance around the average measured positions. Assuming an expansion factor of $k = 2$ and assuming a Gaussian distribution, the uncertainty is given by

$$u_{\text{Pos}} = k \cdot \frac{\sigma_{\text{Pos}}}{\sqrt{N}}, \tag{5.3}$$

where σ_{Pos} is the experimental standard deviation [63]. The measured distances are compared to the actual positions (Figure 5.20). There is a linear relationship between the echo distance and the actual distance. This relationship is independent of both the direction and the diameter of the sphere.

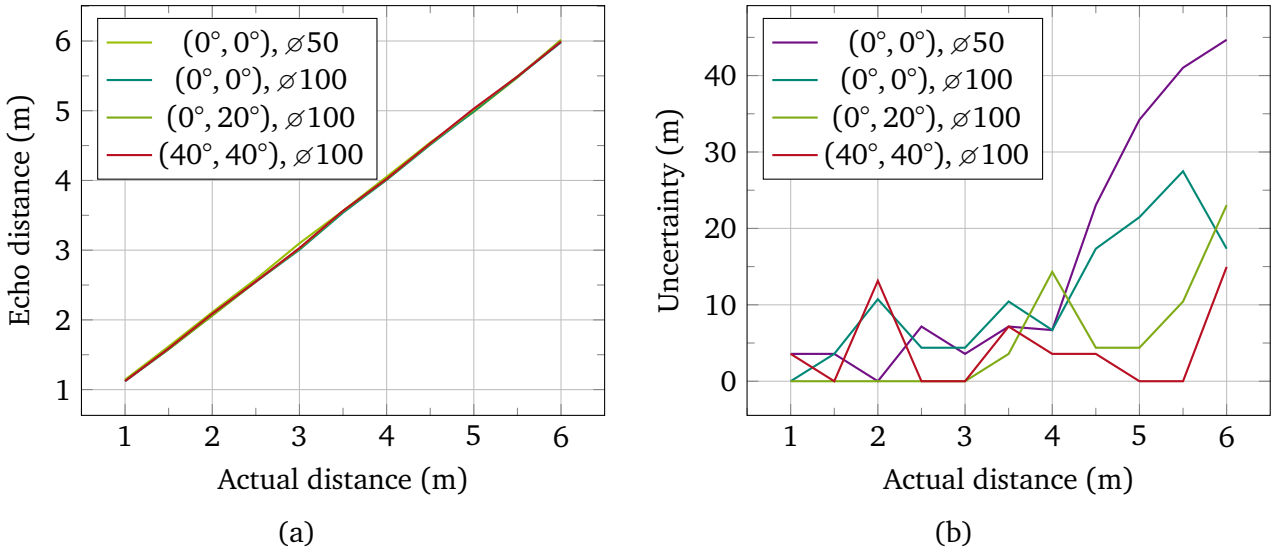

(a) (b)

Figure 5.20.: Accuracy of distance measurement for different directions and diameters. Average echo distances of each $N = 5$ measurements (a) and the measurement uncertainty according to Equation 5.3 (b) of different sphere directions and diameters. ⌀50 designates a sphere of $\varnothing = 50\,\text{mm}$ whereas ⌀100 designates a sphere of $\varnothing = 100\,\text{mm}$. The echo distances carry an offset and a slope error. Both are correctable. The uncertainty increases with increasing distance and the smaller sphere leads to a larger uncertainty.

The measurement error at the minimum distance of 1 m is $\Delta F_{\text{Pos}} = 0.012\,\text{m}$ whereas it is $-0.04\,\text{m}$ at the maximum distance of 6 m. This means, the measurement error consists of a static offset and a slope error. The reason is that the method used to obtain the sphere position from the measurement carries an offset and therefore, the maximum of the echo amplitude is not an ideal estimator for the sphere position.

The slope error is caused by an incorrect velocity of sound c when converting time to distance. The values for the offset error is $\Delta s_{\mathrm{Off}} = 0.152\,\mathrm{m}$ and for the slope error $\Delta m_{\mathrm{s}} = -0.032$. The equation for determining the distance s as a function of the time t is therefore given by

$$s(t) = \frac{342,064\frac{\mathrm{m}}{\mathrm{s}}}{2} \cdot t - 0,152\,\mathrm{m}. \tag{5.4}$$

This formula enables a correction of both systematic errors, however, all further measurements in this chapter show the uncorrected data.

The uncertainty u increases with increasing distance [Figure 5.20 (b)], as less acoustic energy is reflected back. This increases the SNR, and, thus, makes identifying the echoes harder.

The maximal value is $u = 14\,\mathrm{mm}$ up to a distance of 4 m and then increases up to a maximum of $\pm 27\,\mathrm{mm}$ for the sphere of $\varnothing = 100\,\mathrm{mm}$ and up to $\pm 45\,\mathrm{mm}$ for $\varnothing = 50\,\mathrm{mm}$. The uncertainty is not correctable, and, thus, limits the accuracy of the distance value.

After the accuracy of the distance measurement, the directional accuracy is investigated. Again, the sphere is positioned at different positions on the *AZ*- and *EL*-axis and the maximum echo in either direction is plotted against the actual direction (Figure 5.21). Both the *AZ*- and the *EL*-direction carry an

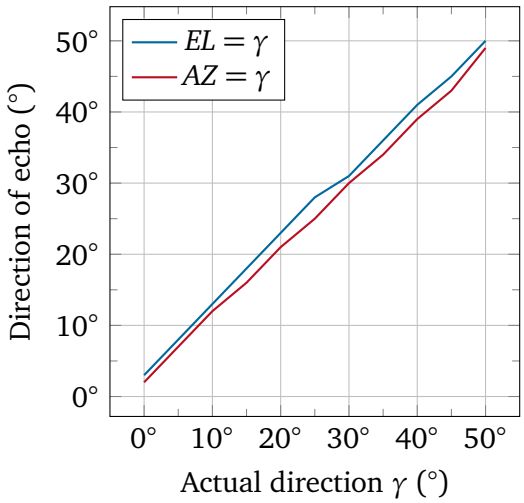

Figure 5.21.: Echo direction versus actual direction for a sphere positioned at a distance of 3 m. Both curves show a different offset and a similar slope error. Both errors are correctable.

offset and a slope error. These are $\Delta F_{AZ} = 2°$ and $\Delta F_{EL} = 3°$. Both directions are subject to the same slope error of -0.06. Similar to the error of the distance measurement, these errors can be corrected. Again, the correction is not done for the other results shown in this chapter.

The uncertainty of the direction u_{Dir} is limited by the smallest possible beam forming increment $\Delta\vartheta_{\mathrm{min}}$ and is therefore

$$u_{\mathrm{Dir}} = k \cdot \frac{\Delta\vartheta_{\mathrm{min}}}{\sqrt{3}} = 1,65 \cdot \frac{1°}{\sqrt{3}} = 0,95°. \tag{5.5}$$

using an expansion factor of $k = 1.65$, (95 % confidence interval) and again assuming a uniform distribution [63].

5.3.4 Axial resolution

Positioning two objects in the field of view of the array leads to the question of axial resolution. The axial resolution is the smallest distance of two objects that can be detected as separate echoes. Moving the objects closer together results in a merge of both echoes. It is then no longer possible to distinguish the common echo from an echo caused by single object of similar size.

The experimental setup is altered by mounting a horizontal bar on the slid of the z-axis (Figure 5.22). This is an aluminum extrusion, t-slot profile, length 1 m. Two spheres of $\varnothing = 100\,\text{mm}$ are mounted to this profile. The heights of the spheres are adjusted to match the center of the array's aperture.

The distance between the center points of the two spheres and the array is set to 3 m. The distance between both spheres is set to the minimum of 100 mm where the spheres touch each other. Subsequently, the distance between the spheres is increased in increments of 50 mm. This is done by moving the first sphere by 25 mm closer to the array and the second sphere further away by the same 25 mm. For each distance, the B-scan-image is inspected for echoes. Once two distinct echoes become visible, the corresponding distance is declared as the axial resolution. Using an excitation signal with 40 cycles, the

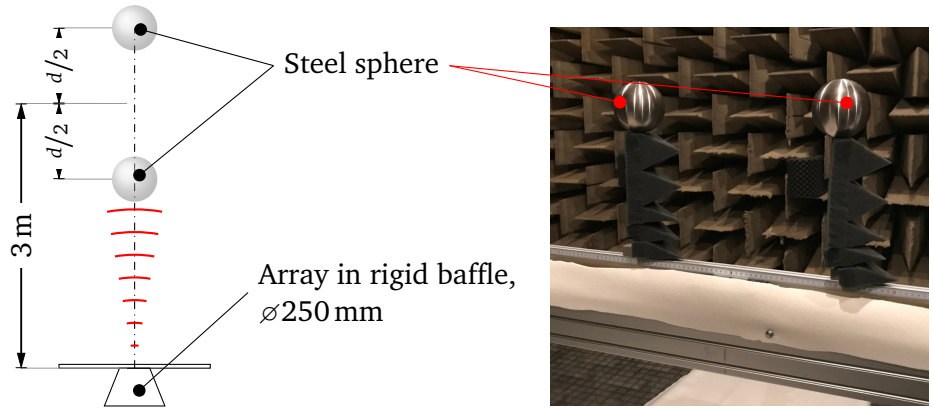

Figure 5.22.: Experimental setup for identifying the axial resolution. The z-axis slid is positioned at a distance of 3 m. The gap between both spheres is kept balanced around 3 meter by moving both spheres in opposite directions (a). Photo of experiment at an inter sphere distance of 400 mm.

minimal detectable distance was found to be 200 mm (Figure 5.23). The amplitude of the second echo is reduced to 67 % compared to the first echo. Two reasons account for this reduction: The first reason is that the first sphere blocks most of the the acoustic energy along the path from the array to the second sphere so less acoustic energy is available at the second sphere. The second reason is that after the reflection occurred at the second sphere, the path back to the array is also obscured by the first sphere. Another good amount of acoustic energy is lost on the way back to the array. This is called acoustic shadowing. The effect is less pronounced when the distance between the spheres is increased. Using an inter sphere distance of 400 mm leads to a significant stronger second echo of 88 % compared to the first echo (Figure 5.24). Compared to an optical system, the second sphere can be detected although it is completely hidden behind the first sphere from the array's point of view.

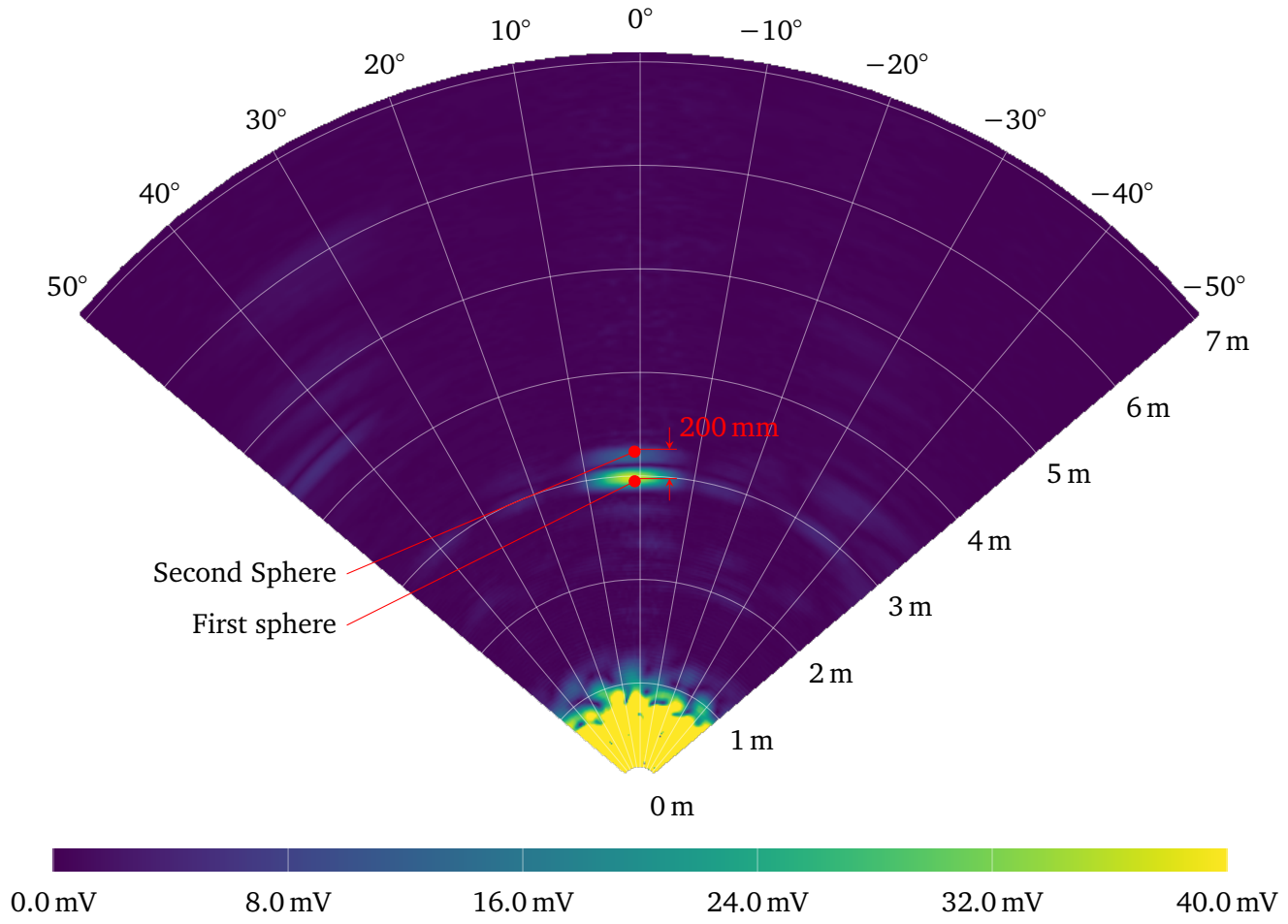

Figure 5.23.: B-scan image of two spheres positioned in front of the array at a distance of 3 m spaced 200 mm apart. There are two separate echoes, however, the second echo is weaker due to acoustic shadowing caused by the first sphere.

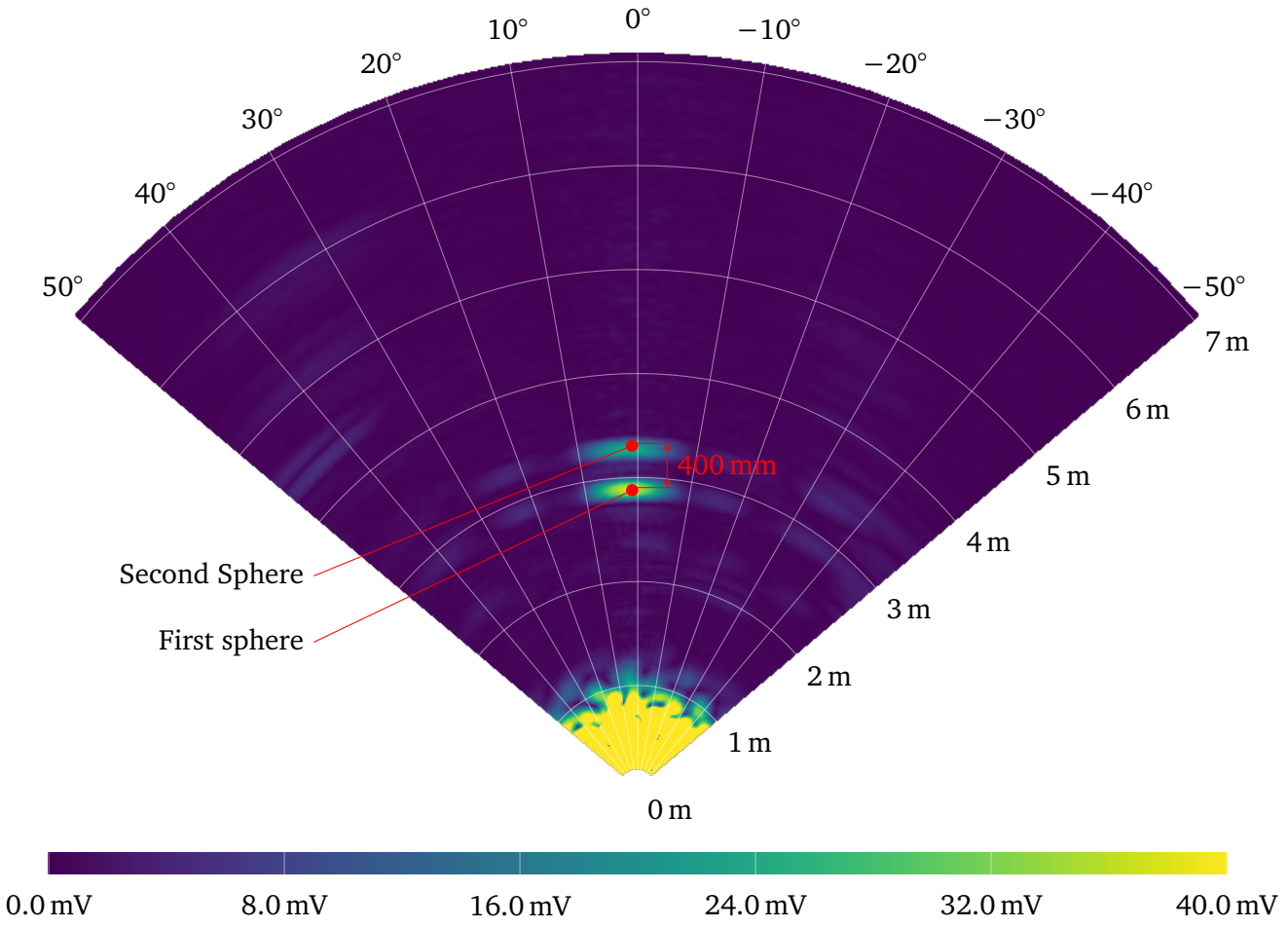

Figure 5.24.: B-scan image of two spheres positioned in front of the array at a distance of 3 m spaced 400 mm apart. The second echo is stronger compared to the B-scan with shorter intersphere spacing of 200 m (Figure 5.23). The effect of acoustic shadowing reduces with increasing intersphere distance.

Adapting the excitation cycles

Reducing the number of excitation cycles increases the axial resolution (Figure 5.25). Using a cycle count of only 10 reveals the two separate spheres at distance of 150 mm. This is closer than the previous minimum distance of 200 mm. The downside is a decrease in transmitted amplitude as the transducers need a minimum of 40 cycles to reach the full amplitude, leading to a reduction of the overall SNR. The narrow band behavior of the transducers therefore limits the axial resolution of the overall system.

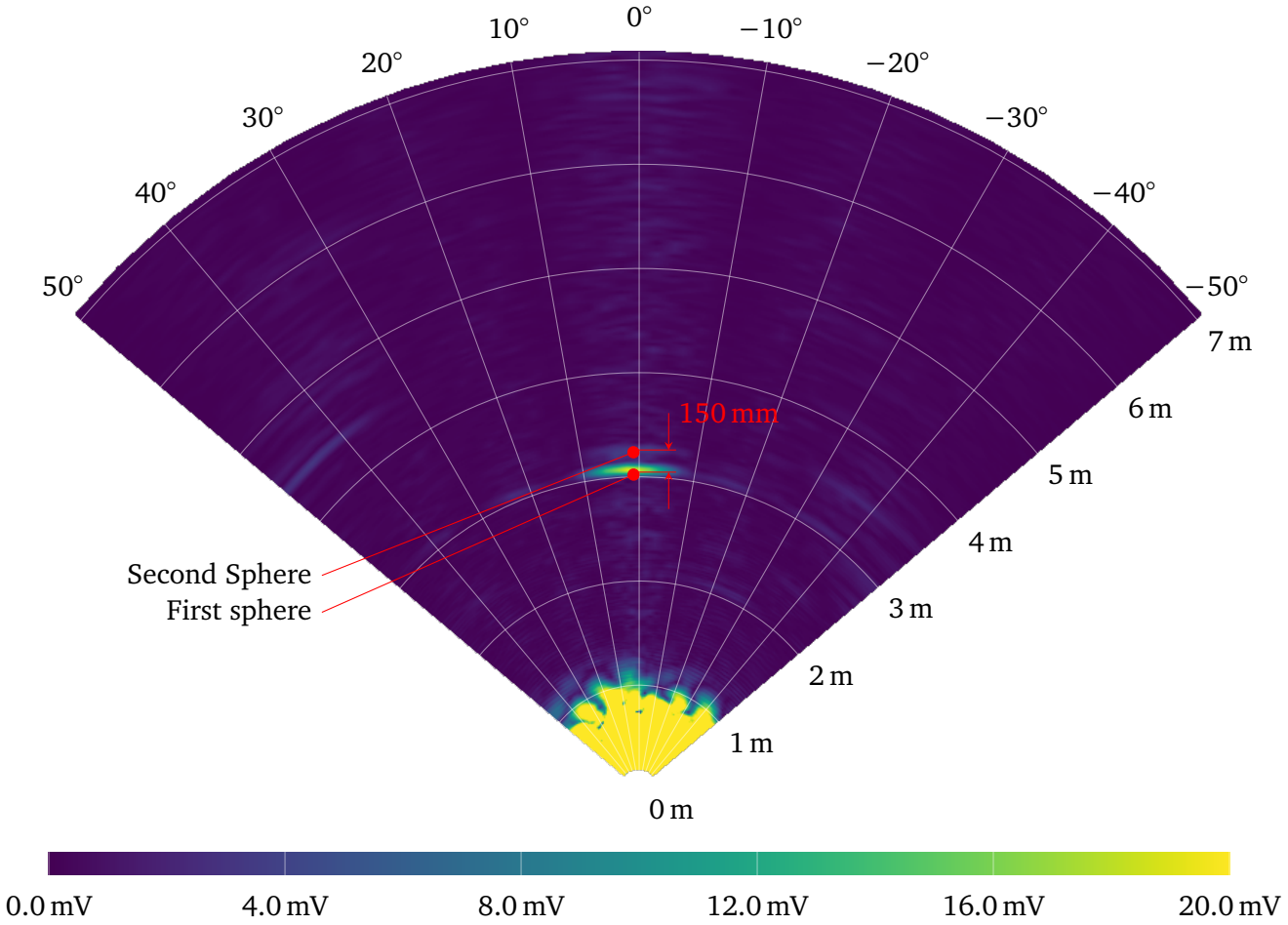

Figure 5.25.: B-scan image of two spheres positioned in front of the array at a distance of 3 m spaced 150 mm apart. The cycle count is reduced to 10 compared to the 40 cycles in Figure 5.23 where the minimum detectable distance is 200 mm. The axial resolution is increased while the amplitude is decreased.

The envelopes of the delay and sum signal in the direction of $AZ = 0°$ using excitations of 40, 20 and 10 cycles are compared (Figure 5.26). Reducing the excitation from 40 to 20 and 10 cycles reduces the amplitude of the echo maxima by 16 % and 58 %, respectively. The individual sphere echoes merge to a single echo for 40 and 20 cycles and are only clearly separable for 10 excitation cycles. The distance between the echoes' maximum is 200 mm, i.e. the second echo is shifted by 50 mm further away than expected. The explanation is that the sound has to travel around the circumference of the first sphere, which a longer path compared to the straight line.

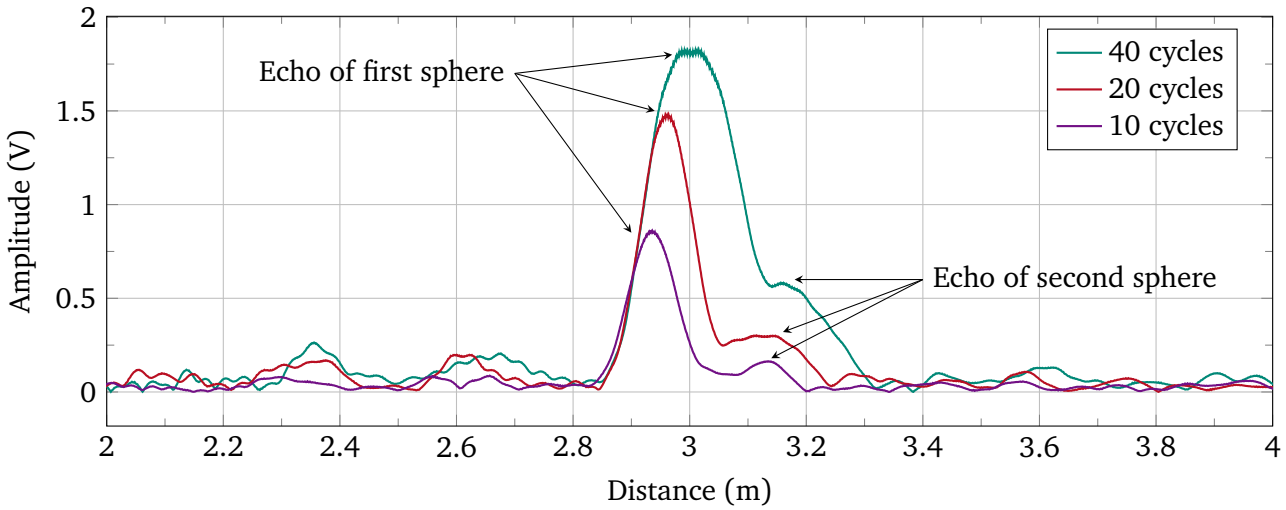

Figure 5.26.: Comparison of the signal envelopes of echoes of different cycle counts for an intersphere distance of 150 mm. Reducing the number of excitation cycles also reduces the echo amplitudes. Only using a cycle count of 10 leads to two distinct echo maxima.

5.3.5 Lateral Resolution

Similar to the axial resolution, the lateral resolution is the minimum angle ϑ_{res} where two objects result in two separate echoes in the B-scan. The experimental setup is adopted so that the mounting bar is now parallel to the aperture of the phased array. The position of the mounting bar remains at a distance of 3 m, however the spheres are now moved to the left and to the right, i.e. in *AZ*-direction, while adopting their distance (Figure 5.27).

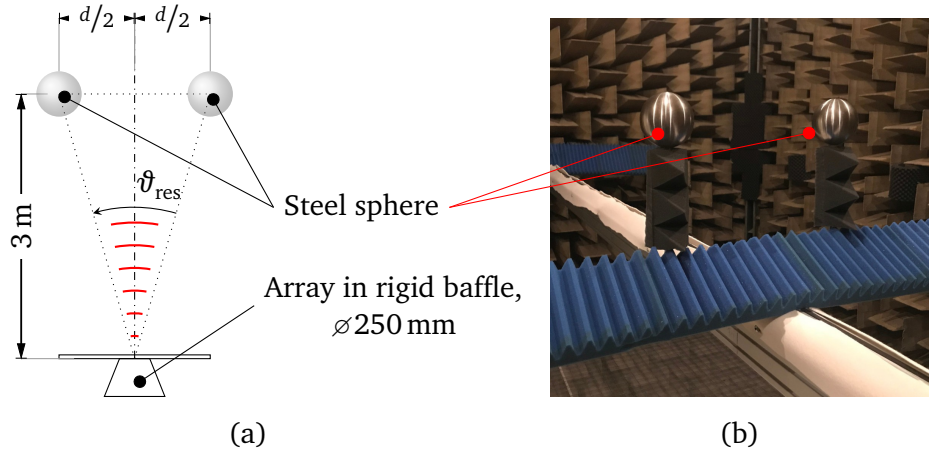

Figure 5.27.: Experimental setup to determine the lateral resolution. A mounting bar is oriented parallel to the array's rigid baffle at a distance of 3 m. The distance between the spheres is equally distributed to both sides. The array may be rotated using the goniometer so that the pair of spheres moves to the left and right within the field of view (a). Photo of experimental setup showing a distance of $d = 400\,\text{mm}$ (b).

For simplicity in the experimental setup, the spheres are not moved along a circular path of constant radius r but on a straight line. The minimum distance d_{min} is converted to the lateral resolution ϑ_{res} by

$$\vartheta_{\text{res}} = 2 \cdot \arctan\left(\frac{d_{\text{min}}}{2 \cdot r}\right), \tag{5.6}$$

where r is the distance of the mounting bar to the array and d is the distance between the spheres.

The lateral resolution is obtained for different sectors in the field of view. The array is rotated by the goniometer in a range of $AZ = 0°$ to $-50°$ using increments of 10°. This moves the pair of spheres within the field of view to the respective angles of $AZ = 0°$ to 50°.

First, two B-scan images are discussed in detail. These are the images of the two view directions of $AZ = 0°$ and $AZ = 20°$.

When the spheres are located at $AZ = 0°$, separate echoes are visible for a minimum distance of 650 mm, which is equivalent to a lateral resolution of $\vartheta_{\text{res}} = 12.36°$. The section view shows a difference in amplitude of both maxima of 2 % (Figure 5.30).

When the spheres are located at $AZ = 20°$, separate echoes are only visible for a minimum distance of 750 mm, which relates to a lateral resolution of $\vartheta_{\text{res}} = 14.25°$. The reason for the increase in distance required is the wider main lobe of the radiation pattern for larger steering angles. The section view shows a difference in amplitude of both maxima of 2 % (Figure 5.30). The amplitudes of the maximum located at 29° is 15 % smaller compared to the maximum located closer to the center at 15° (Figure 5.30). This behavior makes separating the echoes harder as the decrease in amplitude might hide the second maximum.

The trend of increasing resolution for increased angle of view is true for the whole series (Figure 5.28). The maximum resolution of $\vartheta_{\text{res}} = 16.13°$ is reached at 40°. This corresponds to a distance of 850 mm at a radius of 3 m. This means, the distance of separation needs to be higher for outer angles in the field of view.

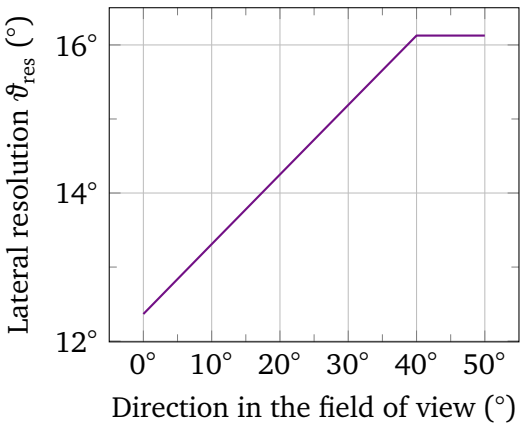

Figure 5.28.: Lateral resolution ϑ_{res} as a function of direction in the field of view. The lateral resolution increases towards the outer region of the field of view. This means objects must be further apart in order to be separable compared to the center of the field of view.

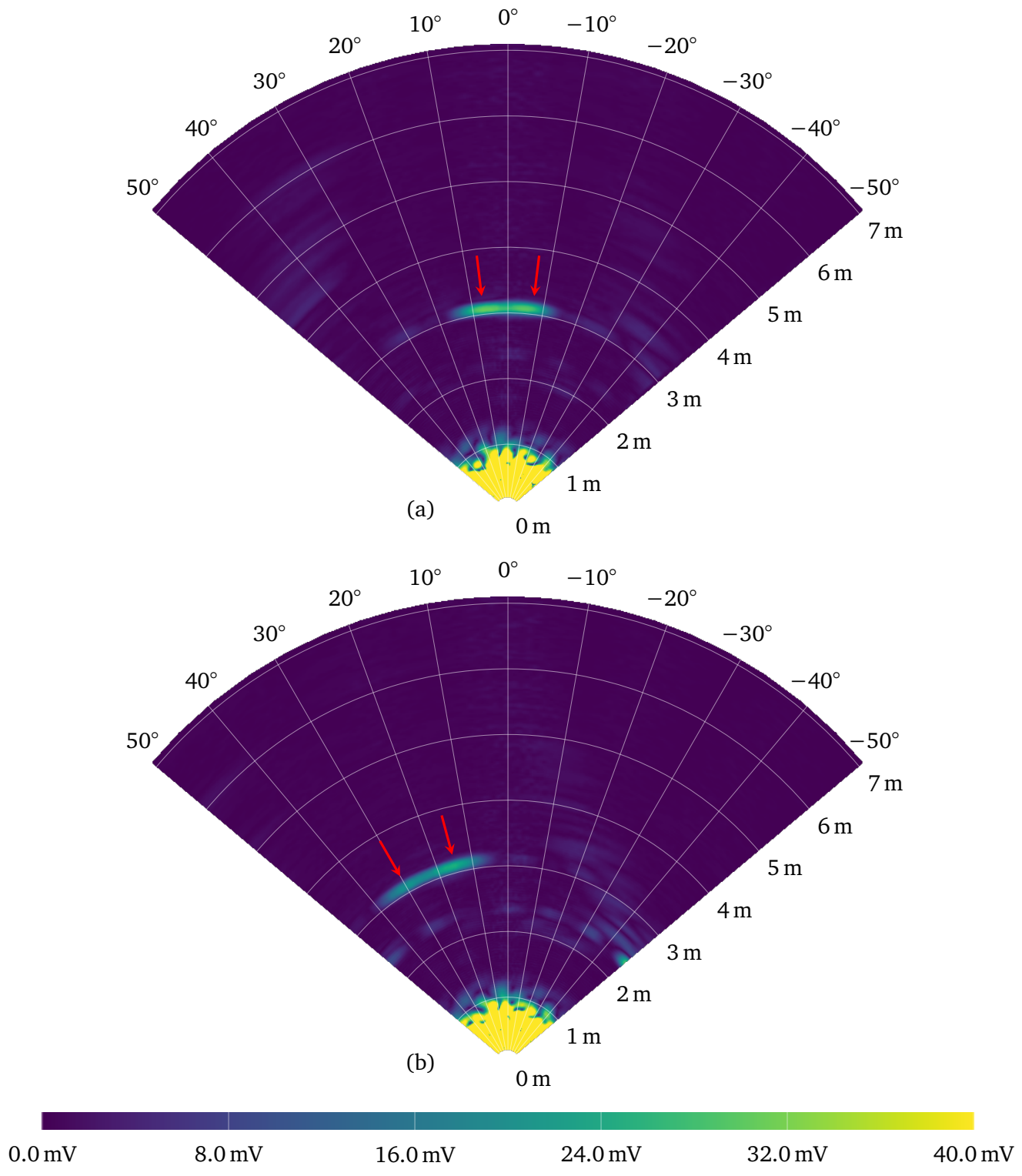

Figure 5.29.: B-scan images of two spheres located at different directions. The center of the spheres are located at a distance of 3 m in the direction of $AZ = 0°$ (a) and $AZ = 20°$ (b). When oriented to $AZ = 0°$, a distance of 650 mm is required to separate the echoes. For the direction of $AZ = 0°$, a distance of 750 mm is required. The echo of the the outermost sphere is weaker compared to the echo closer to the center.

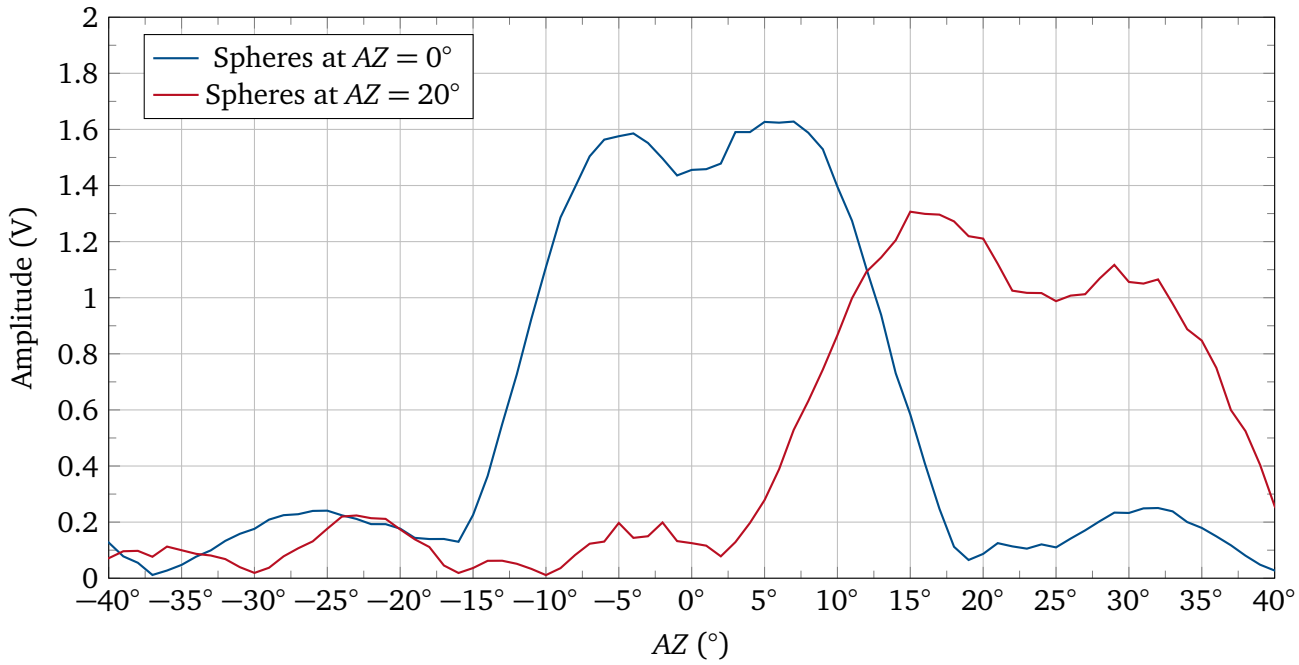

Figure 5.30.: Slices of B-scan images of two spheres. When the spheres are centered in front of the array, the maxima are equal and separable by an angle of about 12°. When the spheres are located at $AZ = 20°$, the maxima are separable by an angle of about 14°, however, the amplitudes of the maxima are no longer equal, and, thus, harder to separate.

5.4 Datasheet

Summarizing the system characterization, a datasheet of all parameters determined is given (Table 5.3).

Table 5.3.: Summary of characteristic values

Parameter	Value		Unit	Notes
	min	max		
TX characteristics				
Main lobe width	20	27	°	
First Side lobe level	−9.5	−9	dB	
RX characteristics				
Main lobe width	12	16	°	
First Side lobe level	−5.6	−5.5	dB	
Range				
Distance	0.5	>6	m	1)
AZ	−50	50	°	
EL	−50	50	°	
Uncertainty				
Distance		± 27	mm	2)
Direction		± 0.95	°	2),3)
Resolution				
axial	150	200	mm	2)
lateral	12.36	16.13	°	2),3)
B-scan				
Duration per frame		3.5	s	4)
Frame rate		0.285	s^{-1}	4)

Notes

1) No range limit was obtained as the range is limited by the SNR and during the characterization, the SNR was sufficient everywhere in the anechoic chamber. Therefore, the given value is only a lower limit.

2) Using steel spheres of $\varnothing = 100\,\text{mm}$ as target.

3) Obtained at a distance of 3 m to target.

4) The duration per frame is limited by the speed of sound. The system has to wait for the echoes for a certain set distance to arrive. Here, a distance of 6 m was used. This means, any echo caused by an object farther away is ignored as the next pulse is already sent.

5.5 Transmit Characterization using Schlieren Optics

Although the characterization using the calibrated microphone and the goniometer provides absolute high resolution images of the sound field, the method has two disadvantages: The microphone is an object of finite size within the measurement volume that reflects soundwaves, and, thus, changes the soundfield itself. Further the measurements are time consuming from several minutes up to several days. As an alternative method, schlieren optics is evaluated.

Schlieren optics is an optical imaging technique that visualizes inhomogeneities in an optical medium, usually a gas or liquid [64]. Such inhomogeneities are caused by temperature, streams of fluids, supersonic shockwaves and sound waves. Schlieren imaging is widely used in aeronautics research and for water-coupled ultrasound. Advanced topics include the 3D-reconstruction of a sound field using the inverse radon-transformation, similar to a computed tomography scan (CT scan) [65], color images [66] or complex optical filters utilizing Fourier optics [67].

The challenge in adopting Schlieren optics for air-coupled ultrasound is the small change in the refractive index caused by the sound pressure, i.e. the *Gladstone-Dale*-constant K_{air}. However, an online video visualizing the acoustic field in an acoustic levitator [68] using Schlieren imaging proved the feasibility of displaying air-coupled ultrasound. This has been the motivation for building a Schlieren setup for air coupled ultrasound during the bachelor's thesis of Yannick Bendel (Figure 5.32) [69].

A Schlieren optics setup consists of a point light source, mapped to an optical filter using either a lens or a parabolic mirror. A camera captures the image of the light source from the optical filter. The optical filter blocks about half of the light from the light source. A ray of light traveling from the light source to the optical filter is refracted by any gradient of the refractive index along its path (Figure 5.31). An

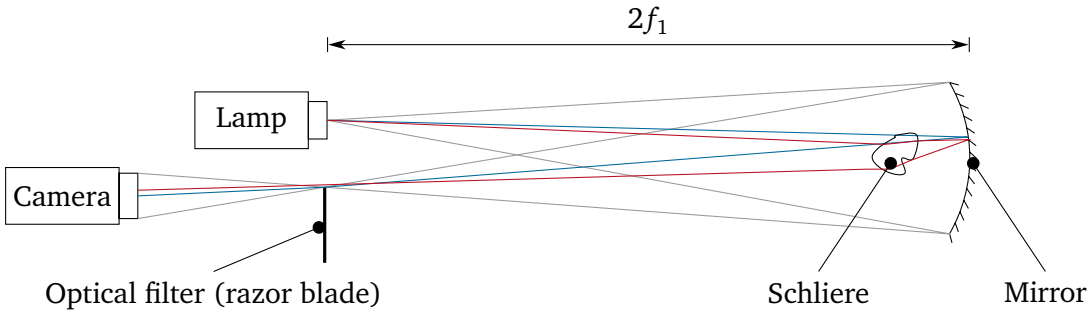

Figure 5.31.: Schematic of a single mirror Schlieren setup. When no Schlieren are present, a ray emitted by the lamp (blue) passes the mirror and optical filter to the camera. When a Schliere is present, the same ray is refracted at the boundary of the Schliere and possibly blocked by the optical filter (red).

ultrasound wave consists of regions with lower and higher pressure compared to ambient pressure, and, thus, causes such refraction. Some rays that pass the filter are blocked when traversing a refractive region, other rays that were previously blocked pass the filter only after traversing such a refractive region. The result is a tomographic image of the refractive index gradient. The longer the distance between the refraction to the optical filter is, the greater is the deflection upwards or downwards on the optical filter. Thus, the longer the distance between the mirror and optical filter is, the greater is the sensitivity of the complete setup.

The total refraction of any ray is the integral over the complete optical path and might be zero. This happens in two cases: A complete sound wave consisting of positive and negative regions passes or the exposure time exceeds half the time of oscillation of the sound wave and the camera integrates over time over a brighter and darker pixel to ambient brightness. The signal frequency of 40 kHz exceeds the shutter speed of conventional digital single-lens reflex (DSLR)-cameras. Thus a pulsed light source synchronized to the ultrasound signal is used. This makes the exposure time independent of the ultrasound process. The system consists of conventional low cost components: A signal generator (type 33500B,

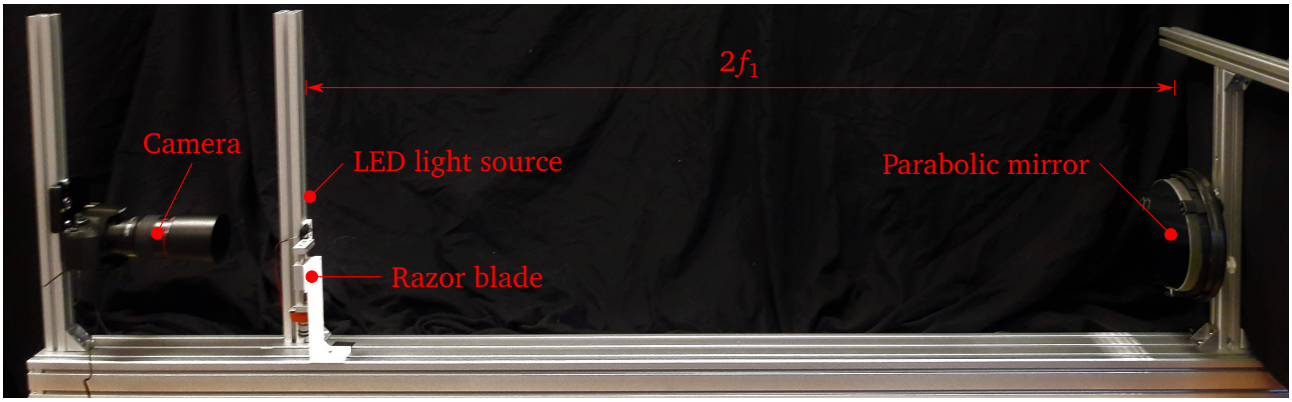

Figure 5.32.: Schlieren imaging setup consisting of a DSLR-camera, an LED as light source, a parabolic mirror and a razor blade as optical filter. All components are mounted on a 120 mm × 80 mm t-slot profile.

Keysight, Santa Rosa, CA, USA) powers a white LED of $\varnothing = 3\,\text{mm}$ as light source. The main optical component is a parabolic mirror, type AD048 (Guan Shen Optical, Qionglin, Taiwan), $\varnothing = 200\,\text{mm}$, focal length $f_1 = 800\,\text{mm}$. Both the light source and the optical mirror are placed at a distance of $2f_1 = 1600\,\text{mm}$. A DSLR, type EOS 1300d combined with a macro lens, (type ET-73), both Canon, Ōta, Japan, captures the image. A simple razor blade is used as optical filter. The blade is mounted on a precise manual operated linear stage. This simplifies the positioning of the blade edge relative to the image of the light source.

For all Schlieren images, the TX-only electronics (subsection 4.3.1) is used. The phased array electronics triggers the signal generator that generates pulses of $T = 25\,\mu\text{s}$, i.e. half of the oscillation period of 40 kHz. The camera is activated using a camera remote (URS-7000, Shenzen DBK Electronics Co.,Ltd, Shenzen, Peoples Republic of China). The remote is capable of activating the camera several times at a programmable interval.

5.5.1 Image processing

The camera captures images of 8-bit per channel, i.e each pixel consists of three integer values between 0 and 255 for the color channels of red, green and blue where 0 is full dark whereas 255 is the brightest possible value. The direct image obtained from the camera shows the expected sound wave pattern. However, the contrast is rather low (Figure 5.33): The difference between peaks and troughs in the camera image is only in the range of 4 to 8, thus only using a $1/32$-th to a $1/64$-th of the visible brightness range. The absolute difference of the background brightness between the top and the bottom of the image on the mirror is about twice as large (10-15) as the difference between peaks and troughs in either region. As the difference between peaks and troughs contains the information of interest, enhancing this difference is desired without enhancing the background gradient. This is achieved by subtracting the background gradient before enhancing the contrast.

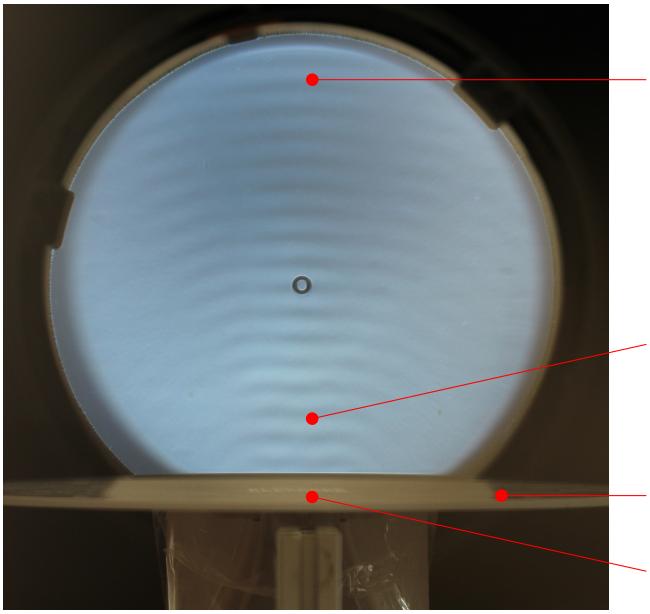

	R	G	B
Peak	46	58	67
Trough	44	51	60

	R	G	B
Peak	60	72	77
Trough	54	66	70

Figure 5.33.: Schlieren image of the equal-length waveguide. The schlieren pattern shows a focused sound beam. The difference in brightness between a peak and trough is smaller (4 to 7) than the difference in brightness of the background (10 to 15). The array is located at the bottom of the image radiating upwards.

For this, a stable image of the background without any Schlieren, neither caused by acoustic waves nor by thermal convection is required. The acoustic waves are removed by disabling the TX electronics. It is important, however, to power the light source by a similar brightness as during the operation with the array. Assuming thermal convection is a stochastic process, the average of multiple background images eliminates images of thermal Schlieren. As the acoustic field is a periodic process, multiple images of the soundfield are averaged as well, also removing any thermal Schlieren. The final difference image between Schlieren image averaged and background averaged is then mapped to the visible brightness range from 0 to 255 (Figure 5.34). The entire image processing chain is done using 8-bit arithmetics using the *GNU image manipulating program* (GIMP).

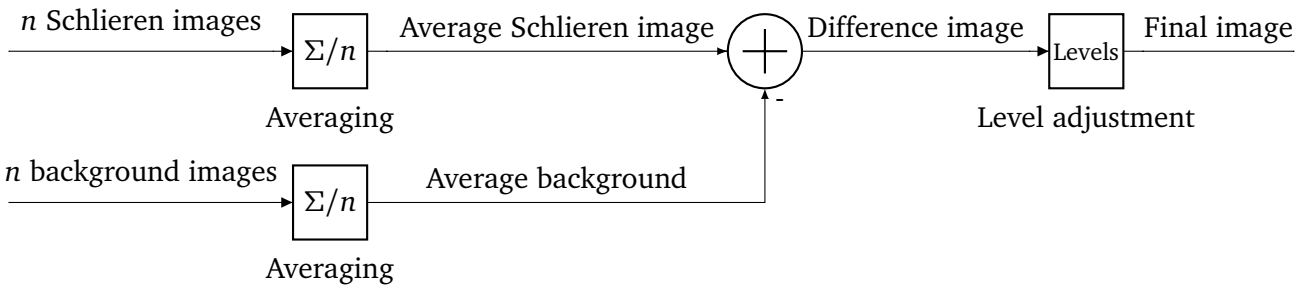

Figure 5.34.: Image processing chain. The final image is composed of the difference between an average schlieren image and an average background image. The difference image is mapped to the visible brightness level using level adjustment.

5.5.2 Results

Schlieren images of both waveguide designs are taken. Images of the equal length waveguide show a clearly focused soundbeam in the three different directions of $\vartheta_s = 0°$, $\vartheta_s = 30°$ and $\vartheta_s = 45°$, respectively (Figure 5.35). Images of the freeform waveguide feature a clear difference with and without active channel length compensation enabled (Figure 5.36). Steering using this waveguide also shows a clearly focused sound beam at different angles (Figure 5.37).

In all images a distinct phase jump between the main and side lobe is visible, as expected. The images of the equal-length waveguide show an almost black background, meaning that the subtraction of the background was successful. The images of the freeform waveguide show a brighter background. The reason is that the averaged background image differs from the averaged Schlieren images. This is most likely caused by a brightness drift between taking the background and the actually Schlieren images.

Compared to the microphone measurements, the Schlieren image is an instant snap shot of the sound wave. The positions of peaks and troughs along the propagation path of the sound wave depend on the delay between the trigger signal of the array electronics and the light pulse. Artificially changing this delay results in the impression of a moving sound wave, although the effect is comparable to the well known stroboscopic effect.

While the image processing chain clearly increased the visual effect of the Schlieren image, several possibilities for improving the image quality remain: A digital camera taking raw pictures uses up to 14 bits per color channel, and, thus, allowing more different brightness levels to be acquired in a single image. The signal processing chain was limited as not only 8-bit arithmetics was used but also no negative brightness was supported. This means negative values where cropped to 0. If an image with negative brightness values was available, a mapping to a visible color range using false color maps such as diverging color maps [30] is required.

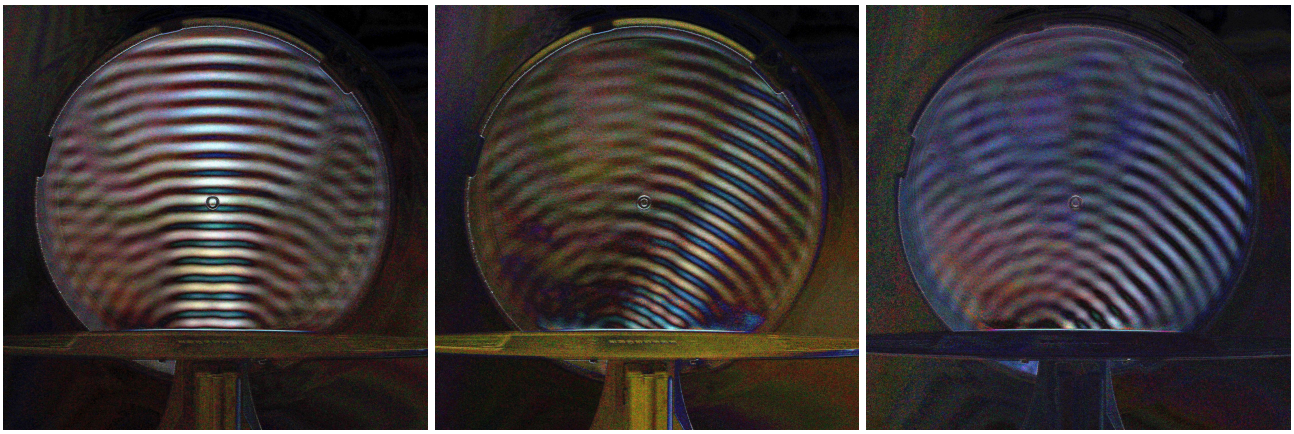

(a) 0° (b) 30° (c) 45°

Figure 5.35.: Schlieren images of the equal length waveguide. Steering to 0° (a), 30° (b) and 45° (c), respectively.

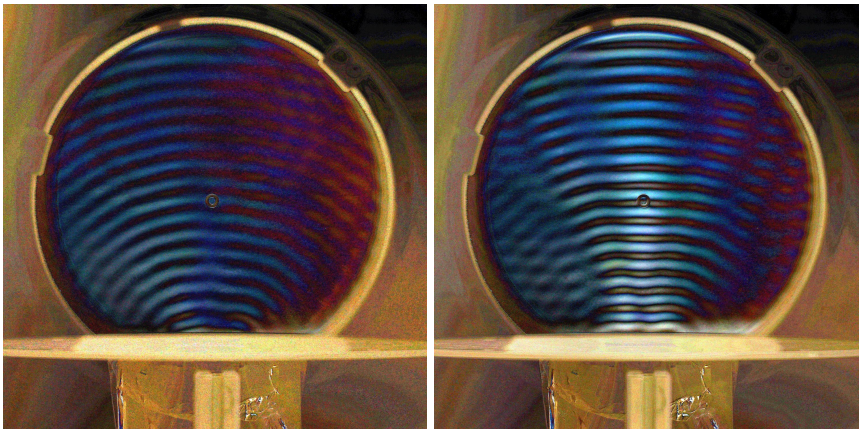

(a) A (b) B

Figure 5.36.: Schlieren images of the freeform waveguide. (a) No compensation of the different channel lengths, (b) Compensation of different channel length active. (b) shows parallel wavefronts in the main lobe and increased contrast and presumably increased sound intensity compared to (a).

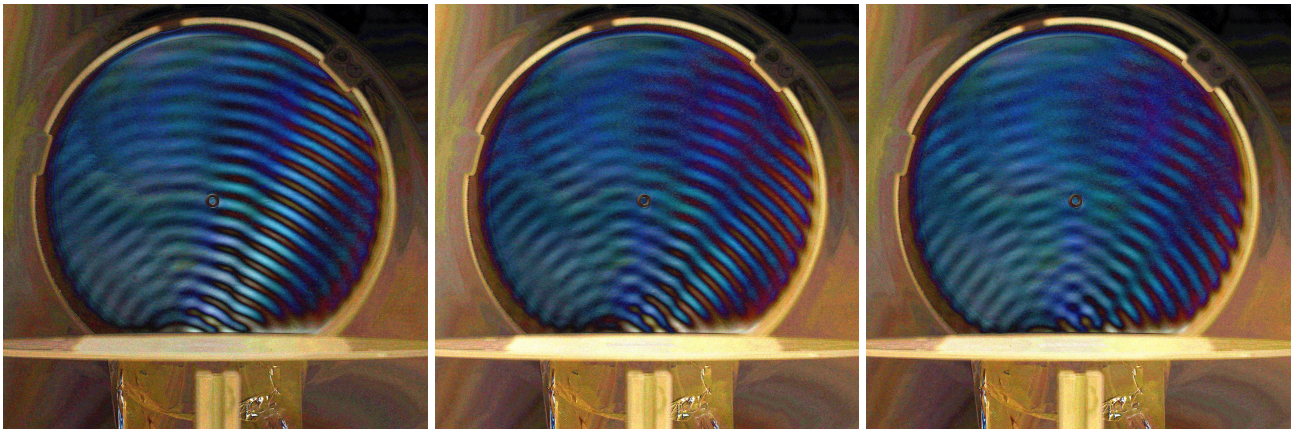

(a) 30° (b) 45° (c) 60°

Figure 5.37.: Schlieren images of the freeform waveguide for steering angles of 30° (a), 45° (b) and 60° (c).

6 Evaluation of air-coupled ultrasound applications

After the characterisation, the system is evaluated in two mature air coupled ultrasound applications. The first application is park distance control where a system of multiple ultrasound transducers operating in pulse-echo mode to assisting drivers of vehicles during low speed maneuvering. The second application is gas flow metering using the transmit time method where a pitch-catch configuration of multiple sender and receiver pairs measure the velocity of a flowing medium in order to obtain the total amount of gas passing pipe per time. Both applications are well established and could potentially benefit of using phased arrays in the future.

6.1 Park distance control

Park sensors or park distance control (PDC) is a driver assistance system that monitors the surrounding area of a vehicle for obstacles, especially in areas that are difficult to see for the driver [70]. Such obstacles might damage the vehicle during parking. A number of ultrasound transducers is placed inside the front and rear bumpers, each measuring the distance to the nearest obstacle. Numbers range from three transducers on the rear bumper only in small, inexpensive cars, such as the Volkswagen *VW120* (Volkswagen Up!, Figure 6.1), up to 12 transducers in premium cars such as the *BMW G31* (BMW 5 Series from 2017 on, Figure 6.2). Four transducers are mounted in both the front and rear bumpers, facing forwards and backwards, respectively. They detect obstacles in front of and behind the car during low speed maneuvering. The remaining transducers face the left and right side of the car, mainly for detecting possible parking spots while driving by. When the PDC system is enabled, one transducer

Figure 6.1.: Three park sensors on the rear bumper of a Volkswagen VW120.

after the other sends bursts and all transducers listen for echoes. Compared to a system where only the senders listen for echoes, it is more likely to detect objects that scatter the ultrasound waves into different directions and, thus, do not reflect back to the sending transducer. As the dimensions of the acoustic aperture built up from all transducers in the bumper together are up to 2 m and the relevant distance for parking maneuvers is less than 2 m, the whole arrangement can be interpreted as a near field array with a large distance of several tens of λ between the array elements. Triangulation is possible as

soon as two transducers receive an echo. From the received signals, distance values for angular sections around the car are obtained, displayed in a top view of the car, optionally combined with camera images. From the six sensors in the front part of the G31, a total of ten distance sectors are obtained (Figure 6.3). Assuming a field of view of 180°, this corresponds to a lateral resolution of 18°.

(a) (b) (c)

Figure 6.2.: Park sensors on a BMW G31. Overview of car (a), Front camera (b) and ultrasound sensors (c)

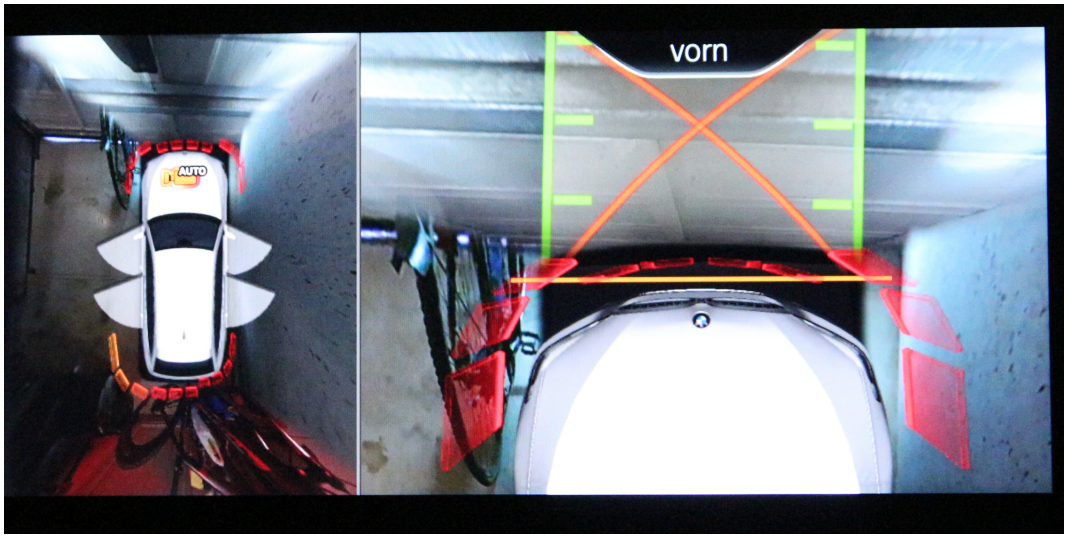

Figure 6.3.: The G31 shows a total of ten distance sectors for both the front and the rear region of the car. Here the car is parked in a garage, providing obstacles to detect in all directions.

A challenge in detecting obstacles using this approach are the echoes caused by the surface of the road. The dominant material for road construction is asphalt. This is a mixture of an organic binder and small stones that causes a surface roughness comparable to the wavelengths of air-coupled ultrasound. Therefore, the road surface scatters ultrasound in all directions and causes immediate echoes. One solution for this problem are transducers featuring an asymmetric beam profile, reducing the amount of ultrasound emitted towards the road. One example of such a transducer is the *MA58MF14-7N*(Murata Seisakusho, Kyōto, Japan, [71]). It operates at 58 kHz and radiates ultrasound in a horizontal angle of 80° but only in a vertical angle of 35°. Matching electronics are for example the *PGA450-Q1* by *Texas Instruments*, Dallas, TX, USA [72].

The experimental setup for evaluating the phased array in a PDC situation consists of the equal length waveguide (section 3.2) combined with the TX/RX-electronics (subsection 4.3.2). The array is mounted at a height of 340 mm. This is a comparable to the heights of the transducers in the BMW G31 between

405 mm for the innermost two transducers next to the license plate up to 540 mm for the outermost sensor next to the front tire.

Poles made of steel, ⌀48 mm, and a height of 1.07 m are used as obstacles. The poles usually used for traffic signs have a slightly larger diameter of about 60 mm, and are, thus, easier to detect. The experiment took place on the park deck of the *Hans-Busch-Institute*, a building of the Technical University of Darmstadt, Germany. It is covered by asphalt. However, compared to an average road surface, it was in rather bad shape: Beside the expected surface roughness of several mm, the surface is partially covered by bumps of up to 20 mm. This means that the measurement conditions are considered worse than an average road and that the results are easily transferable to public road conditions.

The BMW G31 is used as a reference implementation. However as the internal sensor data is not accessible, only screenshots of the dashboard showing both the top view and the driver's view, augmented with the distance sensor data, are available for comparison.

Detection of single object

A single pole was positioned at a distance of 2 m centered in front of the car. The pole is visible in both the top view and the driver's view, however, no distance warning occurred as the obstacle is too far away to cause any harm during a parking maneuver (Figure 6.4).

(a) (b)

Figure 6.4.: Single pole positioned centered in front of car at a distance of 2 m. Outside view of experimental setup (a) and screen shot of the central display (b). The driver's view is augmented with bars indicating distances of 0.5 m, 1 m, 1.5 m and 2.0 m in green and possible tracks of the car when fully steered in red. The pole was visible in both camera views and matched the green bar in the driver's view at 2 m. However, the distance warning did not occur as the obstacle is too far away.

The car was then replaced by the array (Figure 6.8). The array was able to detect the pole at 2 m (Figure 6.6). Compared to the detection of the steel sphere in the anechoic chamber, several weak echoes are visible surrounding the echo of the pole. These echoes are presumably caused by reflections from the ground or ambient noise.

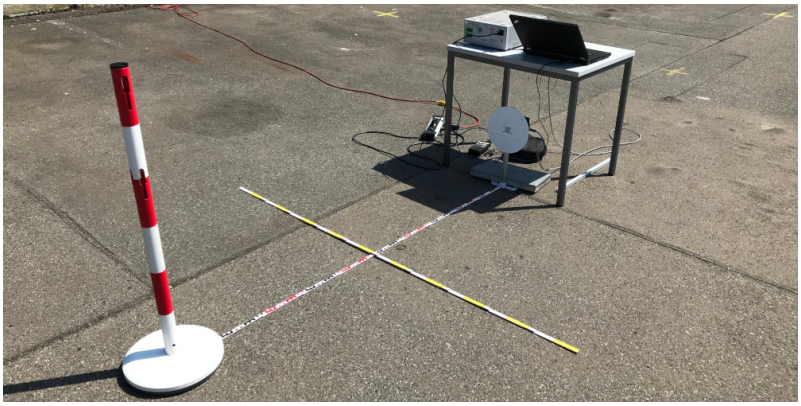

Figure 6.5.: Phased Array on parking deck with pole as obstacle, ⌀48 mm, height 1.07 m at a distance of 2 m. The array was mounted at a height of 340 mm. Supplementing the array, a power supply and a laptop computer were placed on a table above the array. The laptop computer was used for controls and data acquisition. Note that the position of the array does not exactly match the position of the car on the park deck as both experiments where conducted on different days.

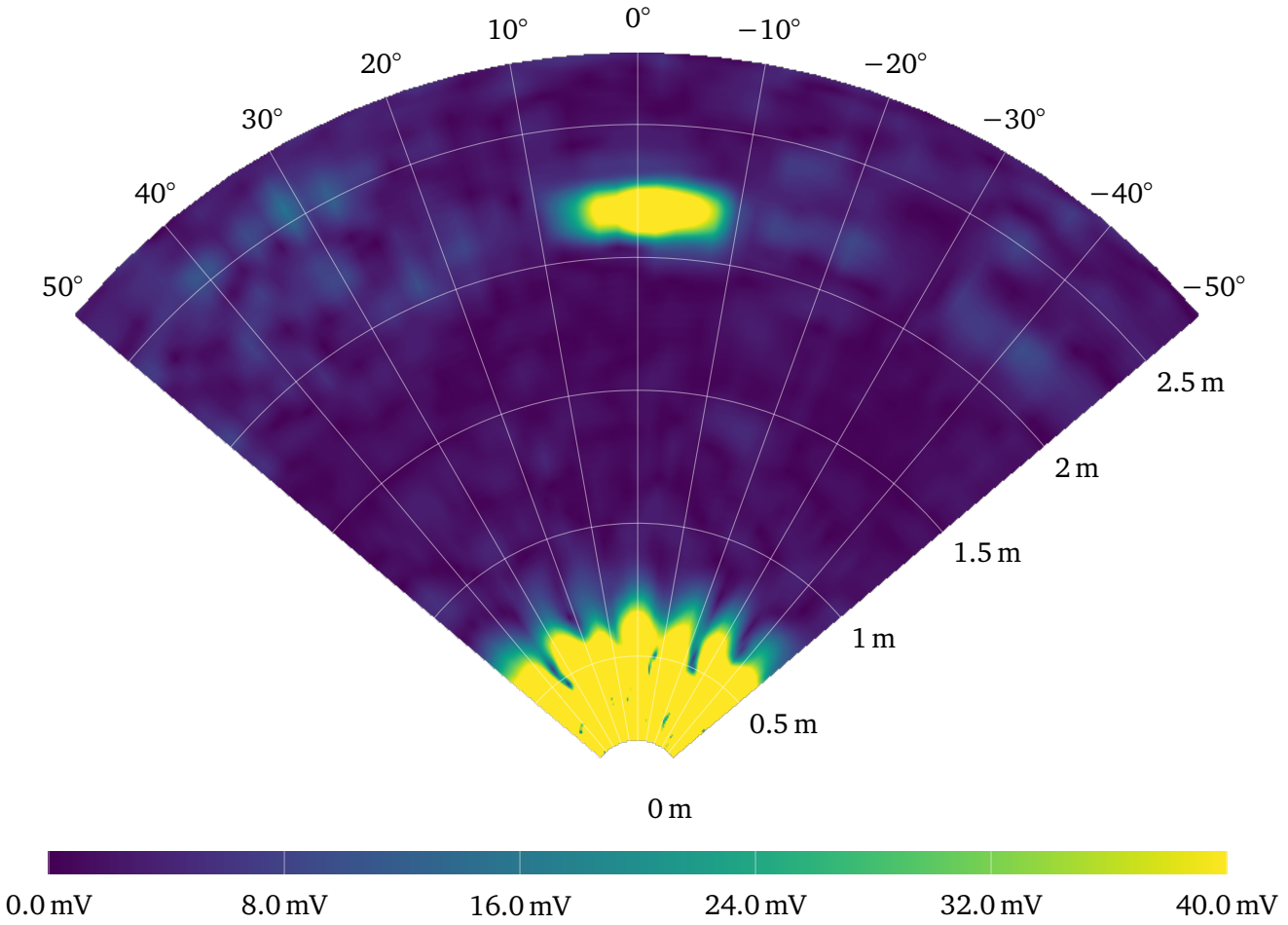

Figure 6.6.: B-Scan-image from the the array showing a single obstacle centered at a distance of 2 m. Several weaker echoes surround the main echo, presumably caused by ambient noise and surface reflections. Note that the maximum of the echo is again not a good estimator for the actual distance of the echo.

Detection of two obstacles

As the experiments in the anechoic chamber demonstrated (subsection 5.3.4), the phased array is able to detect objects that are located behind each other. It was interesting to repeat this experiment under real world conditions and to see how the implementation in the G31 would handle the situation.

Two poles were positioned in front of the car, the closer one at a distance of 1 m, the second one at a distance of 2 m (Figure 6.7). The car again detects an obstacle in the two center sectors but an additional obstacle in the second sector to the left. The screenshot does not provide enough information to find the reason for the third obstacle. It is further unclear whether the car is able to distinguish the second pole behind the closer pole as this information is not necessary for the parking maneuver.

The array is able to detect both poles at their respective positions of 1 m and 2 m. The poles are detected as wider echoes due to the receive main lobe width.

(a) (b)

Figure 6.7.: Two poles centered in front of car at distances of 1 m and 2 m, respectively. The distance warning engaged and shows three orange bars highlighting three sectors. As there is no central section the two innermost sections are highlighted. However, the third section to the right was highlighted although no obstacle was present.

Conclusion

The array has a field of view of about 100° at an angular resolution between 12° and 16°. This allows the field of view to be divided into about 8 sectors. The G31 has a field of view of 180° divided into 10 sectors, resulting in an angular resolution of about 18°. The array has only a slightly better lateral resolution at the current state. For covering the same field of view as the G31, two arrays are necessary. The array is potentially capable of eliminating ground reflections using an angular filter in the vertical direction, however, further experiments are necessary to identify situations where the phased array is truly beneficial. However, at the time of conducting the experiment, only 60 % of the receiving channels are functional and no advanced signal processing algorithms are used that include a model of the array characteristics to further enhance resolution. Both fixing the non functioning channels as well as including more sophisticated signal processing is expected to improve the overall lateral resolution.

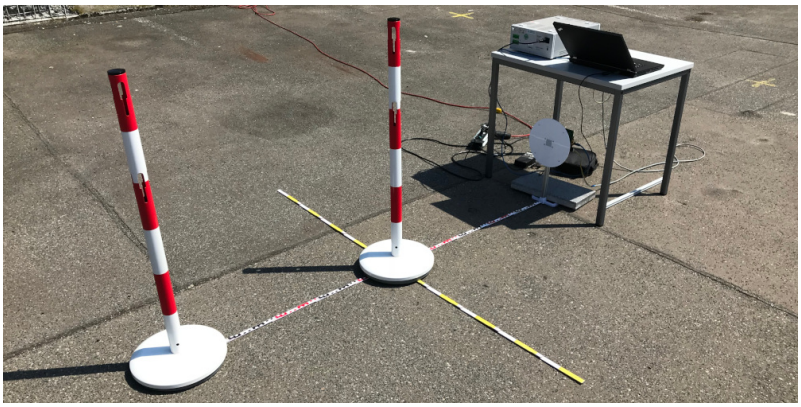

Figure 6.8.: Phased array on parking deck two poles as obstacle, positioned at 1 m and 2 m, respectively.

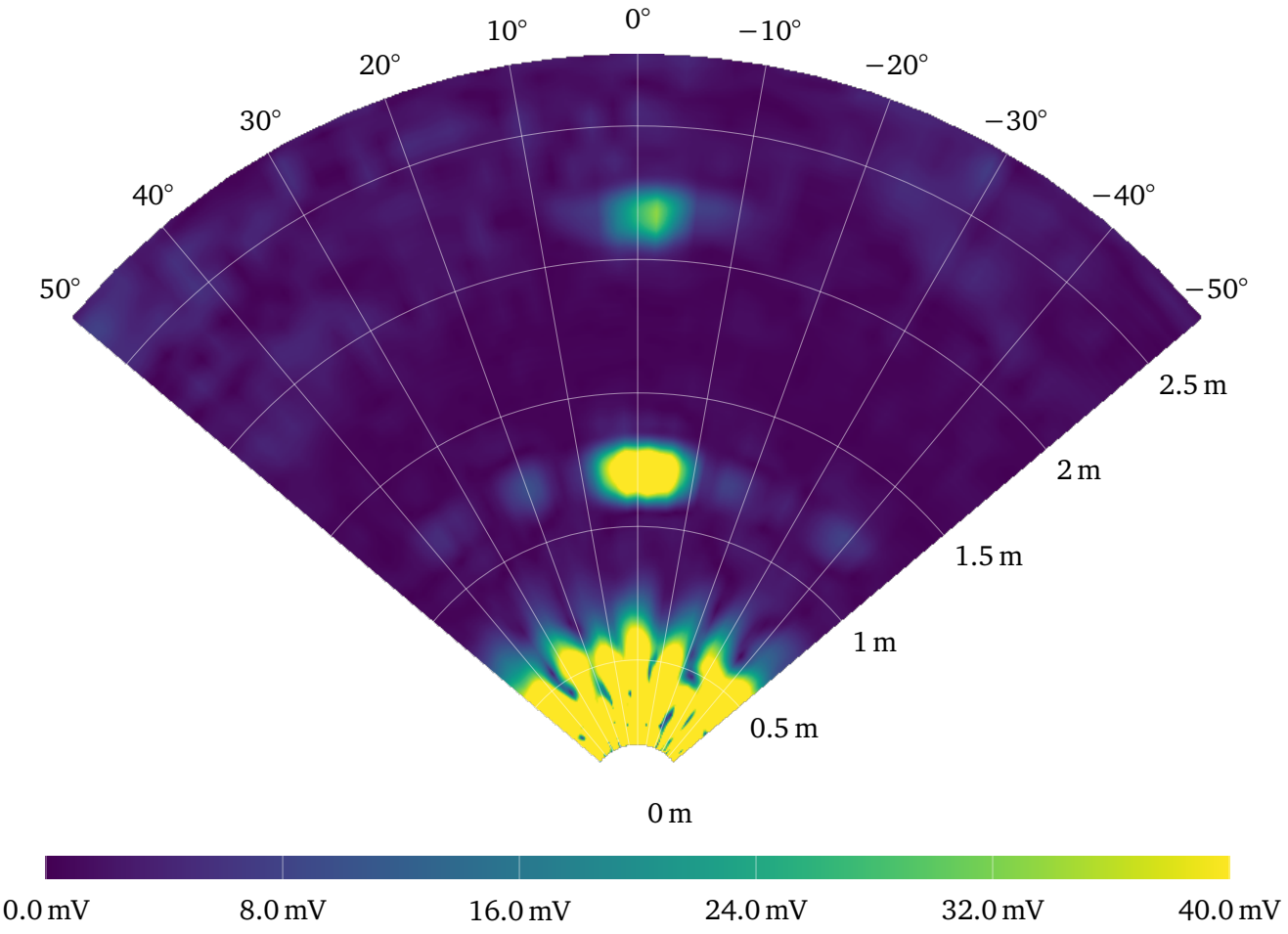

Figure 6.9.: B-Scan-image from the the array showing a single obstacle in centered at a distance of 2 m. Several far weaker echos surround the main echo, presumably caused by ambient noise and surface reflections. The second echo is weaker compared to the first echo, presumably due to acoustic shadowing. The first echoes also cause side lobe artifacts.

6.2 Gas flow metering using the transit-time method

The array developed here is suitable to be used in a transit time flow meter for gases in a pitch catch configuration. First, the principle and its challenges are described; Later on, an experiment utilizing the array in a real world flow meter situation is described. The results where published in 2017 [2].

Measuring the amount of a liquid, gas or bulk good passing through a pipe per unit of time is called flow metering. Whenever such goods are processed or sold, it is necessary to determine the amount of goods transfered.

Ultrasonic transit-time gas flow meters consist of at least two or more sound paths inclined with respect to the gas flow direction. The propagation direction of one sound path is oriented towards the direction of flow, while the other sound path is oriented more against the flow direction. When the velocity of the medium to measure across the sectional area of the pipe is $v_A = 0\,\mathrm{m/s}$, both transit times t_{up} and t_{down} are equal. With increasing flow velocity v_A, the travel speed of the sound waves in downstream direction is increased because the flow velocity adds up to the speed of sound. The travel speed of the sound wave in upstream direction decreases. The increased speed in downstream direction leads to a shorter travel duration t_{down} and to a longer travel duration in upstream direction t_{down}. With increasing flow velocity, the difference $t_{\mathrm{up}} - t_{\mathrm{down}}$ time-of-flight (TOF) increases (Figure 6.10) [73]. From the difference of both

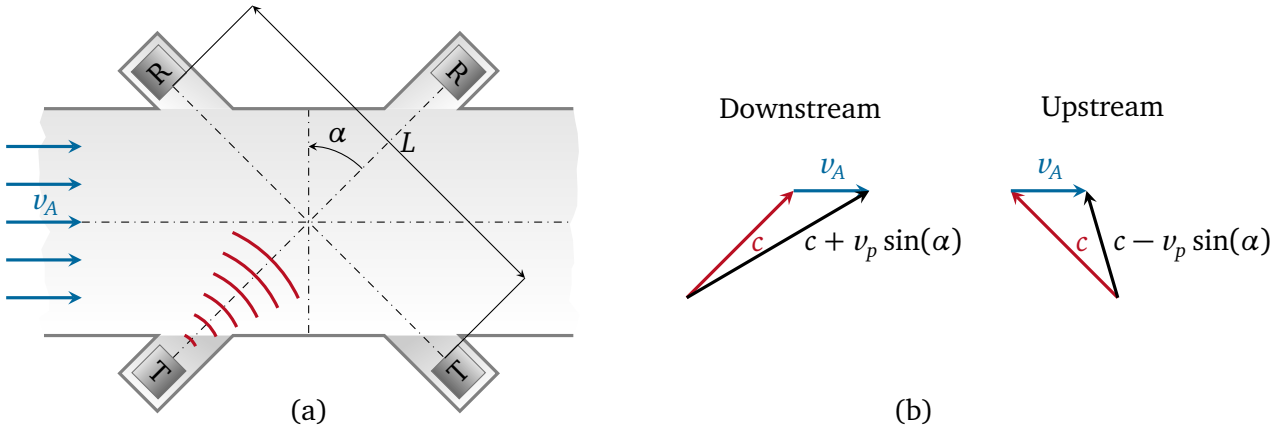

Figure 6.10.: Schematic view of a transit time flow meter (a) and vector diagrams of the two sound paths (b), assuming a box flow profile. With increasing flow velocity v, the time of flight of the downstream sound path decreases whereas the upstream time of flight increases. This is due to the additional velocity component caused by the flowing medium (blue) in addition to the speed of sound (red).

time of flights,

$$\frac{L}{t_{\mathrm{up}}} = c + v_p \cdot \sin(\alpha) \quad \text{and} \quad \frac{L}{t_{\mathrm{down}}} = c - v_p \cdot \sin(\alpha), \tag{6.1}$$

the average velocity v_p along the soundpath of the fluid can be calculated by

$$v_p = \frac{L}{2\sin(\alpha)} \left(\frac{1}{t_{\mathrm{down}}} - \frac{1}{t_{\mathrm{up}}} \right). \tag{6.2}$$

The sound drift effect

The maximum measurable flow velocity v_A is restricted by the sound drift effect [73]. In the usual symmetric setup, both transducers forming a sound path are aligned facing each other. With increasing flow the sound beam drifts towards the downstream direction. The received amplitude decreases as the maximum of the radiation pattern travels along the pipe wall. As soon as the SNR becomes too low, a velocity measurement is no longer possible. This is an unwanted effect that limits the velocity range of every flowmeter (Figure 6.11). The symmetric setup allows flow metering in both directions.

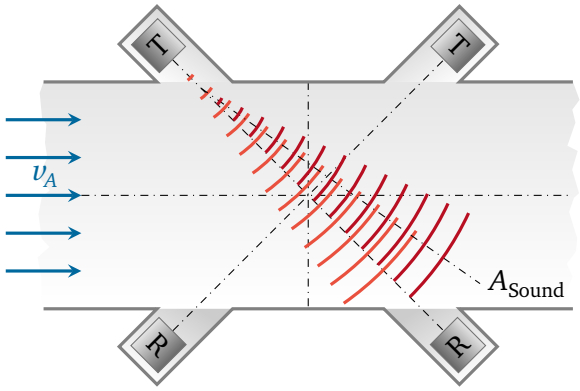

Figure 6.11.: The sound drift effect leads to reduced signal amplitudes with increasing flow speed v_A. As the velocity increases, the axis of the maximum sound pressure is tilted torwards the flow direction and no longer points into the direction of the receiving transducer but into another direction, A_{Sound}.

The received amplitude and, thus, the SNR is maximal at zero flow and drops while the flow increases in either direction. As most flow situations have a preferred flow direction, this is not the optimal configuration [74].

Two approaches of asymmetric flowmeter designs where published that increase the maximum flow rate roughly by a factor of two by sacrificing the symmetric design. Thus, they are no longer able to measure the same maximum flow velocity in both directions. In the flowmeter described in [75], this is achieved by tilting the receivers and in [74], this problem is approached by shifting the two receivers up- or downstream.

Phased arrays in flowmeters

As a phased array allows electronic steering, the sound drift effect is compensated by dynamicaly adjusting the steering angle to hit the receiving transducer, resulting in a larger measurement range and better SNR.

When a sending array is used, the array can aim for multiple receivers, replacing individual senders (Figure 6.12).

The idea of using a phased array to dynamically adjust the sending direction for a flowmeter was already proposed for liquids using transducer arrays clamped on the outside of pipes [76] or using a monolithic, MEMS-based transducer array [77]. Here, a configuration of two arrays was used. Both arrays interchange roles of sender and receiver for the upstream and downstream measurement. The challenge in adopting this principle for gas is the availability of suitable array transducers. The array developed during this thesis is suitable, although the transducers where not originally designed for a flowmeter

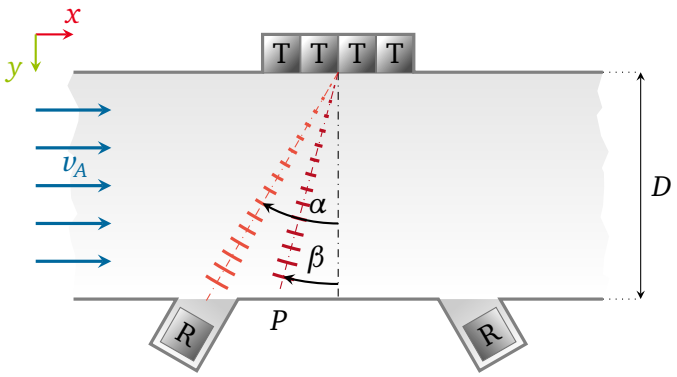

Figure 6.12.: A flowmeter consisting of a phased array transducer that can be electronically steered to aim for an upstream and a downstream receiver. With increasing flow and no compensation for the sound drift effect, the maximum of the main lobe no longer hits the receiver but a different position P and thus the received signal amplitude at the receiver is decreased.

application. However, evaluation using existing flowmeter transducers is easily possible by adopting the geometry parameters of the waveguide design.

Modelling the sound drift effect

The necessary steering is estimated by a simple model. A constant flow velocity profile along the radius of the pipe is assumed ($v_A = \text{const}$). Due to the sound drift effect, e.g. a phased array transmitting at an angle α aiming at the receiving upstream transducer, the maximum amplitude is measured next to the transducer at a position P. The actual angle of the soundbeam is a new angle β. The emission angle α needs to be increased in order to hit the transducer at the maximum amplitude.

The location of point P can be estimated based on equations describing the two velocity components in x- and y-direction of the wave front, i.e.

$$\frac{dx}{dt} = c\,\sin(\alpha) - v_p, \quad \frac{dy}{dt} = c\,\cos(\alpha), \tag{6.3}$$

where v_p is the flow velocity, α the steering angle and c is the speed of sound.

Integrating Equation 6.3 over the TOF t_f gives the two time-dependent components of the position of the wave front, i.e.

$$P_x(\alpha, t_\mathrm{f}, v_p) = \int_0^{t_\mathrm{f}} [c\,\sin(\alpha) + v_p]\,\mathrm{d}t = t_\mathrm{f}\,v_p + t_\mathrm{f}\,c\,\sin(\alpha) \tag{6.4}$$

and (6.5)

$$P_y(\alpha, t_\mathrm{f}, v_p) = \int_0^{t_\mathrm{f}} c\,\cos(\alpha)\,\mathrm{d}t = t_\mathrm{f}\,c\,\cos(\alpha). \tag{6.6}$$

Since we are only interested in the arriving position along the lower pipe wall ($y = D$, where D is the diameter of the pipe), we can eliminate t_f by requiring that P_y is equal to D, i.e.

$$P_\mathrm{y} \stackrel{!}{=} D \Rightarrow t_\mathrm{f} = \frac{D}{c\,\cos(\alpha)}. \tag{6.7}$$

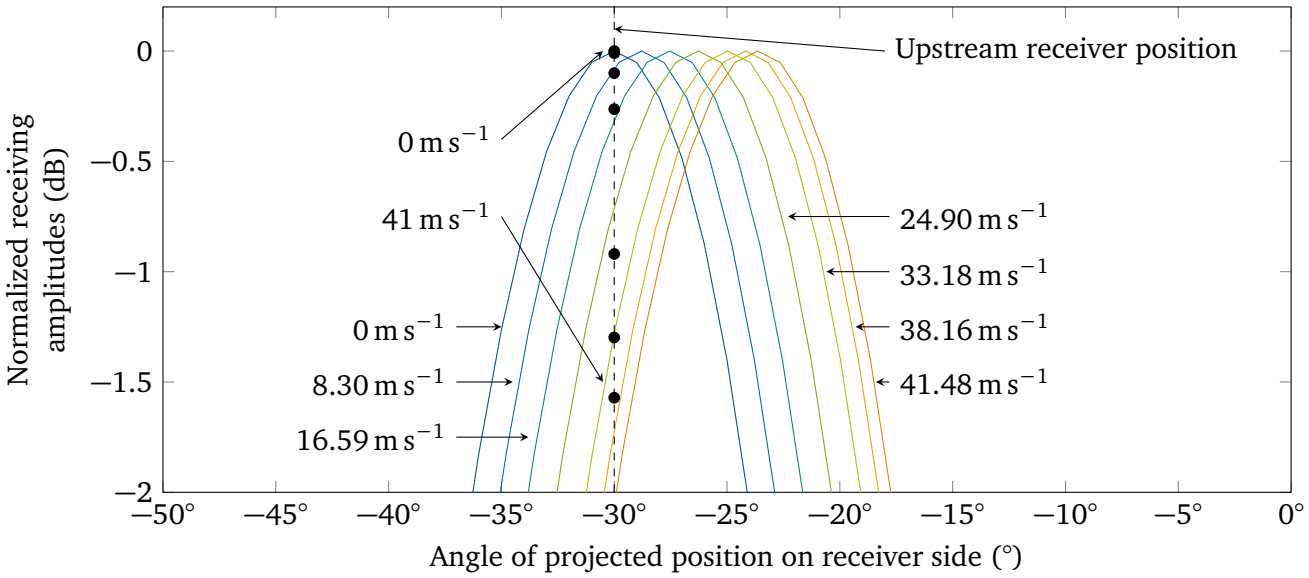

Figure 6.13.: Expected drop in receiving amplitude at the upstream receiver. The curves for the downstream receiver are not shown. The −30° beam profile is simply shifted by $\beta - \alpha$ according to the flow velocities measured in the experiment. The dots depict the actual measured amplitudes at the upstream receiver.

The expression

$$P_x(\alpha, v) = D\left[\frac{v_P}{c\cos(\alpha)} + \tan(\alpha)\right] \tag{6.8}$$

describes the point of arrival of the sound beam as a function of α and v_P.

The expected drop in amplitude depends on both the resulting main lobe width of the phased array configuration and the actual gas flow velocity v_p.

Based on the calculated position $P_x(\alpha, v_p)$, the angle β (Figure 6.12) can be inferred by the expression

$$\beta = \arctan\left[\frac{P_{\mathrm{x}}(\alpha, v_p)}{D}\right]. \tag{6.9}$$

The reduced amplitudes for each different flow velocity can be found by evaluating the shifted profile at $-30°$ (Figure 6.13). Here, an array configuration matching Figure 6.12 using an equal-length waveguide combined with the TX-only electronics is used.

The compensation of the sound drift requires a new steering angle α for each flow velocity v_p. This angle is obtained by numerically solving the equation

$$P_{\mathrm{x}}(\alpha, v_p) \stackrel{!}{=} x_{\mathrm{tr}} \Leftrightarrow x_{\mathrm{tr}} = D\left[\frac{v}{c\cos(\alpha)} + \tan(\alpha)\right] \tag{6.10}$$

$$\Rightarrow \alpha = f(v, x_{\mathrm{tr}}, D) \tag{6.11}$$

for α by requiring that P_{x} is equal to the transducer position x_{tr}. Mathematica (Version 11, Wolfram Research Inc., Champaign, IL, USA) was used for solving Equation 6.11.

Experimental setup

A custom flowmeter was built, based on a commercial flow meter body (Figure 6.14).

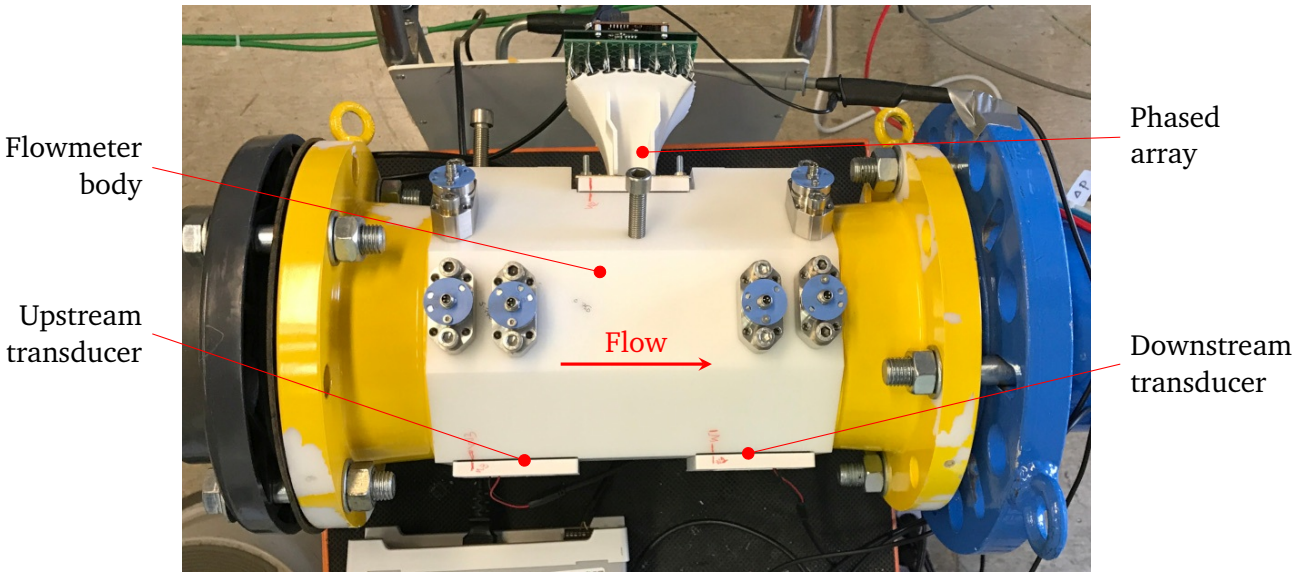

Figure 6.14.: Experimental setup consisting of a phased array mounted onto a custom made flowmeter body. The single element upstream and downstream receivers are mounted at the opposite side. The flow direction is from the left to the right.

The flowmeter body, made from nylon, has an inner diameter of 146 mm. It features three universal rectangular mounting ports of 60 mm × 60 mm each. One port at the top houses the phased array assembly. The phased array assembly consists of the equal-length waveguide combined with the TX-only electronics, a steel connector plate and a 3D-printed adapter [Figure 6.15 (c)]. This adapter extends the channels at the phased array aperture [Figure 6.15(b)] into the meter body and closes the port cavity with a curvature matching the pipe diameter.

Two other identical adapters mount the receiving transducers inclined towards the transmitting phased array [Figure 6.15(d)]. Two ports for the up- and downstream receivers are located at the opposite side at positions facing the phased array port at angles of ±30° [Figure 6.15(d)].

All experiments using the flowmeter have been conducted at a commercial gas flow rig at *Honeywell Process Solutions*, Mainz, Germany. The rig consists of a radial compressor as gas flow source (HVM 80-125 GR, Venti Oelde, Oelde Germany), with a nominal flow rate of 1750 $\mathrm{m^3\,h^{-1}}$ and a reference flow meter, (TRZ G1600 DN200, Elster Instromet, Mainz, Germany), with a nominal range of 300 $\mathrm{m^3\,h^{-1}}$ to 2500 $\mathrm{m^3\,h^{-1}}$. An oscilloscope (Model RTH, Rhode und Schwarz GmbH & Co. KG, Munich, Germany) recorded the arrival times t_u and t_d and amplitudes from both the up- and downstream receivers. The arrival times require systematic corrections mostly due to the propagation times in the waveguide, the pipe adapter and other port cavities.

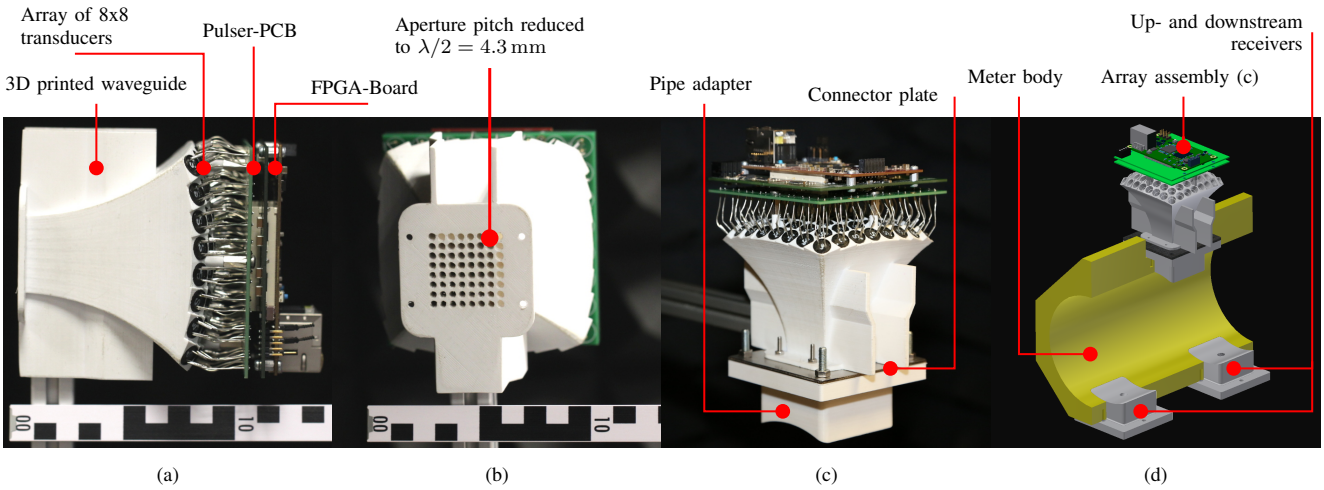

Figure 6.15.: The equal length waveguide is combined with the TX-only electronics (a). The array aperture (b) is mounted to the pipe adapter (c) using a connection plate made from steel. The pipe adapter matches the inner diameter of the flow meter body (d). Two single element transducers are used as receivers (d). Scale bars are in cm.

Signal processing

The flow velocity is calculated from the TOF t_{up} and t_{down}. In the introduction, a constant flow profile was assumed so to that average velocity along the sound path v_p (Equation 6.2) was identical to velocity averaged over the pipe area (v_A).

When a more realistic flow situation is assumed, a correction factor, the so called *meter factor* [78], is introduced, i.e.

$$k_{\mathrm{v}} = \frac{v_{\mathrm{A}}}{v_{\mathrm{p}}} = \frac{4}{D}\frac{\int_0^R v(r) r\,\mathrm{d}r}{\int_0^R v(r)\,\mathrm{d}r}. \tag{6.12}$$

Here, a velocity profile,

$$v(r) = v_{\max}\left[1 - \left(\frac{r}{R}\right)^{2m}\right], \tag{6.13}$$

with

$$m = \frac{0.8741 + 0.0121\log_{10} Re}{2(0.1259 - 0.0121\log_{10} Re)}, \tag{6.14}$$

found in [73], was used. The Reynolds number Re for Equation 6.14 was calculated with the help of the reference flow rate, obtained from the calibrated flow rig measurements.

Results

First, the array was configured to steer to $+30°$ and $-30°$, imitating a regular flow meter with no sound drift compensation. The volumetric flow rate was increased in six steps up to $2700\,\mathrm{m^3\,h^{-1}}$, the maximum available at the flow rig, resulting in a maximum flow velocity of $41.5\,\mathrm{m\,s^{-1}}$. As expected, with increasing flow velocity the received signal amplitudes measured by both receivers reduced by 39 % and 26 %, respectively, when the flow velocity was ramped up to the maximum [Figure 6.16(a) and (d)].

Second, for each flow velocity, the array was configured to steer in the directions of $-45°$ to $-15°$ for the upstream receiver and 15° to 35° for the downstream receiver in steps of one degree. For each of these flow velocity values, the angle with the maximum received amplitude was picked as the best steering angle, mimicking a working sound drift compensation. The best amplitudes per flow velocity were compared to the model (Equation 6.11) [Figure 6.16(b) and (e)]. The picked amplitudes only drop by 13% for both upstream and downstream at the maximum flow velocity of $41\,\mathrm{m\,s^{-1}}$ and exceed those without steering [Figure 6.16(a) and (d)]. Since the model uses the assumption of a constant flow velocity (box profile), the predicted receiving amplitude on the downstream receiver deviates from the experimental data. Therefore, the model needs to be extended in order to consider sound refraction effects along flow velocity gradients as well. The calculated flow velocities v_A, obtained from the measurements, match well with the one obtained from the arrival times t_u and t_d, i.e. using Equation 6.2 and Equation 6.12 [Figure 6.16(c) and (f)]. The flow rig that was available for these experiments was limited to a maximum flow velocity of $41\,\mathrm{m\,s^{-1}}$. Although a drop in amplitude for the uncompensated case was noticed, the received amplitude was sufficient in both the compensated as well as the uncompensated case.

Waveguides in flowmeters

The waveguide used here for shrinking the aperture has secondary benefits. As the dominant principle in ultrasound transducers is the piezo electric effect, the operating temperature of these transducers is limited by the Curie temperature of the respective materials. The typical Curie temperature is only several hundred degrees Celsius, preventing flow metering in exhaust systems of combustion engines.

Using a thermo insulating waveguide, ultrasound is transfered into a hot flowing medium as well as transfered from a medium to a receiving transducer. Several patents cover this approach [79, 80, 81, 82, 83]. Beside the FDM method used in this thesis, there are numerous other 3D printing methods available including selective laser melting (SLM) that fabricate parts from metals or ceramics, suitable as thermal insulators.

Conclusion

The experiment shows that the approach of using a phased array for compensating the sound drift effect, and, thus, increase the maximum velocity to measure, is feasible. Further, the use of the waveguide, motivated by the diameter of the available transducers, leads to potential increase in the maximum temperature of the gas to measure.

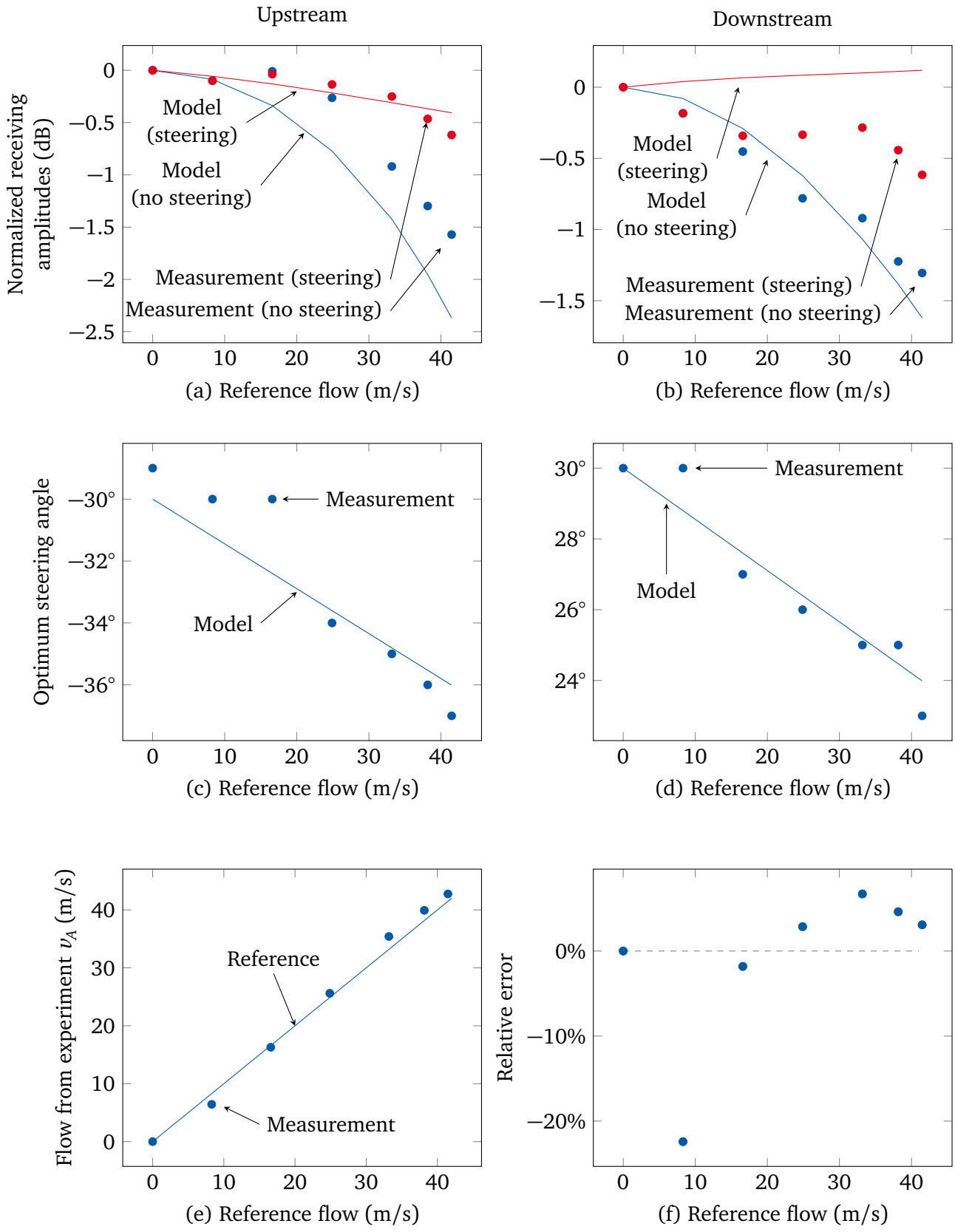

Figure 6.16.: The received amplitudes on the up- (a) and downstream receiver (b) decrease less with steering enabled. The predicted steering angle for upstream (c) and downstream (d) match the model. From the received waveforms on the transducers, the calculated flow (e) is compared to the reference (f). The difference is less than 10 % for all but one data point.

7 Conclusion and future work

The characterization and the application examples show that the approach of an aperture separating waveguide is suitable for building an unprecedented air-coupled ultrasound phased array, optimized for operation in the far field. Both waveguide designs fulfill their design goal of reducing the aperture pitch down to $\lambda/2$, resulting in a radiation pattern without grating lobes.

The equal-length waveguide implements an waveguide that shrinks the aperture pitch using channels of the same length, similar to the previous work that was utilizing heat shrink tubes [14, 13]. The state of the art is improved by reaching a $\lambda/2$-aperture-spacing in two dimensions compared to the previous work that only showed a line array. The characterization shows that the chosen geometric model indeed results in a waveguide with channels of the same length. The manufacturing was also improved by using 3D-printing. This fabrication method allows a reproduction of the waveguide and, thus, the reproduction of the experiment. In this thesis, the approach of an equal-length waveguide was only shown for a rectangular aperture arrangement. In principle, an equal length waveguide using a hexagonal aperture is possible, however, the modeling is cumbersome as the features found in current parametric CAD-applications are not suitable for this kind of abstraction.

The second waveguide design, the freeform waveguide, requires electronics that are able to compensate for different channel lengths. This allows the positioning of the transducers anywhere in a given build volume. Especially placing transducers in a flat plane is interesting as electronic components, such as ultrasound transducers, are usually soldered to a flat PCB. This removes the need for manually extending the pins on the transducers and allows transducer arrays directly mounted on PCBs to be fitted with an aperture shrinking waveguide. The characterization shows that the approach of electronic compensating the different channel lengths is also feasible. Adopting the freeform model for other aperture arrangements such as a hexagonal or sparse arrays is easily possible. The only requirement is a substrate carrying the transducers in a similar pattern as the aperture, only utilizing a larger pitch to accommodate for their physical size.

Any combination of the two waveguides with the developed electronics is possible. Both electronics are further usable for other air-coupled ultrasound experiments. The concept of the TX-electronics allows excitation frequencies of 200 kHz and above at the cost of angular resolution. Excitation voltages of up to 150 V are possible. This allows experiments using new transducer types as soon as these become available.

The combined TX/RX-electronics features trigger-in and trigger-out connectors. This makes experiments utilizing multiple arrays possible as soon as the batch of professional manufactured pieces is available. The choice of attaching the electronics directly to the array, requiring only an Ethernet connection and a power supply allows cable lengths of up to 100 m to the controlling PC. This is beneficial when the array is evaluated in an industrial environment such as flow metering.

The signal processing architecture using a conventional PC and utilize a GPU for signal processing is cost effective and allows the fast evaluating of new signal processing methods. In this thesis, only a very simple raster scan method was used. Far more sophisticated signal processing algorithms and scanning methods are available that require way less data and, thus, allow higher frame rates [84]. During all experiments, mid-class GPUs where used. These algorithms require more computing power, however scaling up is a matter of upgrading the GPUs to a more powerfull model. The opposite approach of

using an embedded GPUs is interesting as it would allow the system to work independently of a data processing computer.

The characterization revealed that the axial resolution is 12.36° in the center of the field of view and gets worse for the outer regions of the field of view. This means that the field of view of about 100° is only divided into 8 distinguishable sectors. This is not significant better than the 10 sectors in a field of view of 180° found in a current premium car. Using the raster beam method utilized here, the only way of increasing the resolution is the narrowing the main lobe of the radiation pattern. This is only achieved by increasing the dimensions of the aperture, which requires more channels in the electronics since the pitch of $\lambda/2$ is still necessary. An evaluation of other scanning methods is needed that in order to improve the lateral resolution using the existing hardware.

The flow meter experiments proof the principle of increasing the possible velocity range. However, on the flow rig used during the experiments, the maximum flow rate was limited to 41 $\mathrm{m\,s^{-1}}$. Although a higher signal amplitude was demonstrated when steering was active, the signal amplitude was sufficient even in the unsteered case. Further experiments using a flow rig with higher flow rates are necessary here. A Bachelor's thesis started just recently, investigating this topic. In addition, at the time of conducting the flowmeter experiments, only the TX-only electronics were available and receiving was done using a single element transducer attached to an oscilloscope. Therefore, no RX-beamforming was possible. Using receive beamforming, a spatial filter eliminates sources of noise from directions other than the TX-transducer or -array.

Future experiments include contactless NDT-applications. Here, a planar wave is refracted at the surface of a plate shaped sample and excites Lamb-waves. Each combination of material and thickness requires a specific angle. The phased array can be configured for any angle. By using the combined TX/RX-electronics, the optimal angle can be determined automatically. A bachelor thesis investigating this topic is currently about to finish.

The array generates sound pressures of up to 150 dB close to the aperture. Sound pressures of this magnitude allow particle manipulation applications such as acoustic levitation. First experiments of levitating small styrofoam spheres where successful, however, further experiments are necessary to relate the system to the near field levitation demonstrated by Marzo et al. [10].

One more experiment is the parametric speaker effect [85, 86, 87, 88]. Here, audible sound is modulated on the ultrasound signal. The parametric effect in air demodulates the audible sound, however, only in directions where ultrasound was present in the first. This means, a highly directional audio playback is possible. First experiments here where successful, but are not presented in this thesis.

As the freeform waveguide enables the use of planar transducer arrays, a proposal to the German research council (DFG) is currently prepared in cooperation with the department of material science. Here, an array of combined piezo-electric and electrostatic actuated transducers is proposed (Figure 7.1). Two substrates, each carrying an array of piezo-electric transducers are combined using a spacer. The piezo-electric transducers work independently but each pair of transducers from the top and bottom substrate also form an electrostatic transducer. This allows two different converter principles. Additionally, the prestress introduced by the electrostatic force tunes the piezo electric transducers and potentially allows multiple operating points, and, thus, multiple operating frequencies. The acoustic energy radiated to the top of the assembly is reflected by cavities acting as Helmholtz-resonators. A matching waveguide ensures the $\lambda/2$-spacing, regardless of the dimension of the transducers necessary to operate at 40 kHz.

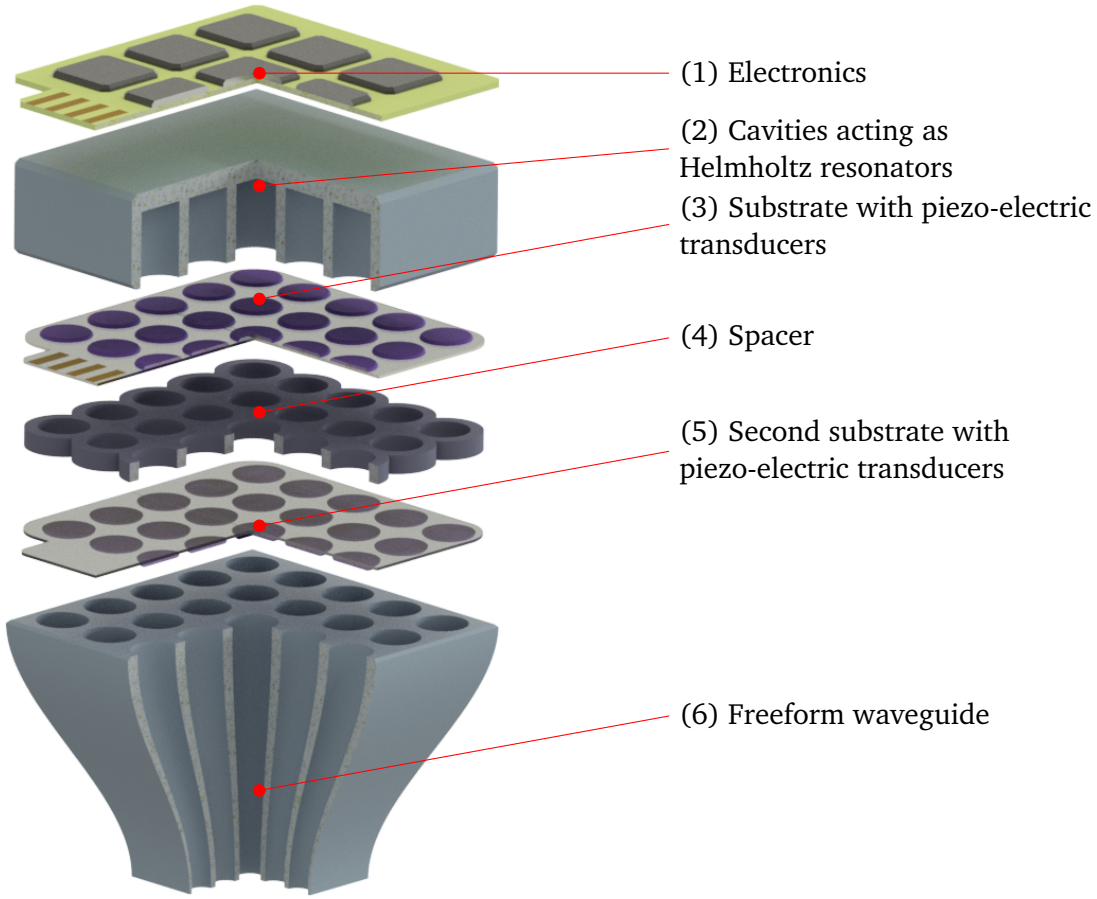

Figure 7.1.: Concept for a phased array system utilizing a combined piezo-electric and electrostatic working principle. Piezo-electric transducers are fabricated as array on a substrate [(3) and (5)]. Two of these substrates are mounted together using a spacer layer (4). Each cell consisting of the two piezo-electric transducers also acts a electrostatic transducer. The energy radiated to the top is reflected to the downside using cavities at the top acting as Helmholtz resonators (2). A freeform waveguide design adopts the transducer apertures to a $\lambda/2$-spacing. The electronics are placed again directly on the setup (1).

The diversity of future work shows that the experiments described in this thesis are just a few of the many potential applications of the array. Even with the current state of hard- and software, more fundamental experiments are possible. As soon as fully working RX/TX-electronics are available, another bunch of experiments is possible such as arrays of arrays or true pitch catch arrangements.

Vita

Dipl.-Ing. Axel Jäger
Heinrichstraße 101
64283 Darmstadt

Born October, 18th 1985 in Frankfurt am Main

Experience

Since 2/2013	Technische Universität Darmstadt Darmstadt, Germany Research Associate at the Chair of Measurement and Sensor Technology.
4/2010 - 1/2013	Fraunhofer Institute for Secure Information Technology Darmstadt, Germany Research Assistant in Cyber-physical systems
1/2005 - 3/2010	basysKom GmbH Darmstadt, Germany Software developer for Embedded Systems and Graphical User Interfaces

Education

2013	Diplom	Technische Universtität Darmstadt Darmstadt, Germany Diploma in electrical engineering Grade 2.3 (good)
2005	Abitur	Max-Beckmann-Schule Frankfurt am Main, Germany Grade 1.6 (good)

Prizes

2011	HBM Förder-stipendium	Scholarship funded by Hottinger Baldwin GmbH, Darmstadt Germany.
2005	Jugend forscht	German young scientist competition Subject: Chemistry Topic: Biological fuel cells Rank: State winner, 5th price in nation wide competition.
2004	Jugend forscht	German young scientist competition Subject: Chemistry Topic: Biological fuel cells Rank: Regional winner, qualified for state wide competion in Hessen.

Bibliography

[1] A. Jäger, D. Grokurth, M. Rutsch, A. Unger, R. Golinske, H. Wang, S. Dixon, K. Hofmann, and M. Kupnik. "Air-coupled 40-kHz ultrasonic 2D-phased array based on a 3D-printed waveguide structure". In: *2017 IEEE International Ultrasonics Symposium (IUS)*. 2017. DOI: 10.1109/ULTSYM.2017.8092532.

[2] A. Jäger, A. Unger, H. Wang, Y. Arnaudov, L. Kang, R. Su, D. Lines, S. N. Ramadas, S. Dixon, and M. Kupnik. "Ultrasonic phased array for sound drift compensation in gas flow metering". In: *2017 IEEE International Ultrasonics Symposium (IUS)*. 2017. DOI: 10.1109/ULTSYM.2017.8092174.

[3] A. Jäger, S. Johannesmann, L. Claes, M. Webersen, B. Henning, and M. Kupnik. "Evaluating the influence of 3D-printing parameters on acoustic material properties". In: *2017 IEEE International Ultrasonics Symposium (IUS)*. Nov. 2017, pp. 1–4. DOI: 10.1109/ULTSYM.2017.8092398.

[4] L. Claes, A. Jäger, S. Johannesmann, M. Webersen, M. Kupnik, and B. Henning. "Acoustic Material Characterization of Additively Manufactured Components". In: *Proceedings Sensor 2017*. 2017, pp. 605–610. DOI: 10.5162/sensor2017/P2.9.

[5] L. Kang, A. Feeney, R. Su, D. Lines, A. Jäger, H. Wang, Y. Arnaudov, S. N. Ramadas, M. Kupnik, and S. Dixon. "Two-dimensional flexural ultrasonic phased array for flow measurement". In: *2017 IEEE International Ultrasonics Symposium (IUS)*. Sept. 2017, pp. 1–4. DOI: 10.1109/ULTSYM.2017.8092220.

[6] M. Hoffmann, A. Unger, A. Jäger, and M. Kupnik. "Effect of transducer port cavities in invasive ultrasonic transit-time gas flowmeters". In: *2015 IEEE International Ultrasonics Symposium (IUS)*. Oct. 2015, pp. 1–4. DOI: 10.1109/ULTSYM.2015.0272.

[7] A. Jäger and F. Klug. "Vertical interconnection on porous substrates with conductive ink". DE 102016122508. 2016.

[8] *The Nobel Prize in Physics 1909*. 1909. URL: https://www.nobelprize.org/prizes/physics/1909/summary/.

[9] Tom Carter, Sue Ann Seah, Benjamin Long, Bruce Drinkwater, and Sriram Subramanian. "UltraHaptics: Multi-point Mid-air Haptic Feedback for Touch Surfaces". In: *Proceedings of the 26th Annual ACM Symposium on User Interface Software and Technology*. UIST '13. St. Andrews, Scotland, United Kingdom: ACM, 2013, pp. 505–514. ISBN: 978-1-4503-2268-3. DOI: 10.1145/2501988.2502018. URL: http://doi.acm.org/10.1145/2501988.2502018.

[10] A. Marzo, S. A. Seah, B. W. Drinkwater, D. R. Sahoo, B. Long, and S. Subramanian. "Holographic acoustic elements for manipulation of levitated objects". In: *Nature Communications* 6.8661 (2015). DOI: 10.1038/ncomms9661.

[11] A. Marzo, T. Corkett, and B. W. Drinkwater. "Ultraino: An Open Phased-Array System for Narrowband Airborne Ultrasound Transmission". In: *IEEE Transactions on Ultrasonics, Ferroelectrics, and Frequency Control* 65.1 (Jan. 2018), pp. 102–111. ISSN: 0885-3010.

[12] A. Langen. *Ein Verfahren zur Konstruktion anwendungsoptimierter Ultraschallsensoren auf der Basis von Schallkanälen*. IPA-IAO - Forschung und Praxis. Springer Berlin Heidelberg, 2013. ISBN: 9783642478710. URL: https://books.google.de/books?id=TNydBgAAQBAJ.

[13] T. Takahashi, R. Takahashi, and SH. Jeong. "Ultrasonic phased array sensor for an electric travel aids for visually impaired people". In: *Proc. of SPIE* 6794 (2007), pp. 67943V–67943V–6. DOI: 10.1117/12.783988.

[14] A. Unger, E. Konetzke, M. Rutsch, M. Hoffmann, S. N. Ramadas, S. Dixon, and M. Kupnik. “Versatile air-coupled phased array transducer for sensor applications”. In: *2015 IEEE SENSORS*. Nov. 2015, pp. 1–4. DOI: 10.1109/ICSENS.2015.7370187.

[15] E. Konetzke, M. Rutsch, M. Hoffmann, A. Unger, R. Golinske, D. Killat, S. N. Ramadas, S. Dixon, and M. Kupnik. “Phased array transducer for emitting 40-kHz air-coupled ultrasound without grating lobes”. In: *2015 IEEE International Ultrasonics Symposium (IUS)*. Oct. 2015, pp. 1–4. DOI: 10.1109/ULTSYM.2015.0019.

[16] M. Rutsch, E. Konetzke, A. Unger, M. Hoffmann, S. N. Ramadas, S. Dixon, and M. Kupnik. “Extending the receive performance of phased ultrasonic transducer arrays in air down to 40 kHz and below”. In: *2015 IEEE International Ultrasonics Symposium (IUS)*. Oct. 2015, pp. 1–4. DOI: 10.1109/ULTSYM.2015.0095.

[17] *MA40S4S*. Murata Manufacturing Co., Ltd. URL: https://www.murata.com/en-sg/products/productdata/8797589340190/MASPOPSE.pdf?1450668610000.

[18] C. Heil. “Sound wave guide”. US5163167A. 1988. URL: https://patents.google.com/patent/DE68915582D1.

[19] J. D. Meyer, P. Meyer, and R. D. Herr. “Manifold for a horn loudspeaker and method”. US6668969B2. 2001. URL: https://patents.google.com/patent/US6668969B2.

[20] M. Adams. “Multiple aperture speaker assembly”. US8718310B2. 2011. URL: https://patents.google.com/patent/US8718310B2.

[21] R. Magalotti. “Acoustic waveguide and electroacoustic system comprising said waveguide”. EP1927978B1. 2006. URL: https://patents.google.com/patent/EP1927978B1.

[22] C. Heil. “Public address system with adjustable directivity”. US7751581B2. 2004. URL: https://patents.google.com/patent/US7751581B2.

[23] F. Galton. *Natural Inheritance*. Macmillan, 1889.

[24] “Electrostatic loudspeaker having acoustic wavefront modifying device”. US3778562A. 1973. URL: https://patents.google.com/patent/US3778562A/en.

[25] F. Guarato, G. B. de Lima, J. F. C. Windmill, and A. Gachagan. “Airborne broad-beam emitter from a capacitive transducer and a cylindrical structure”. In: *2016 IEEE International Ultrasonics Symposium (IUS)*. Sept. 2016, pp. 1–4. DOI: 10.1109/ULTSYM.2016.7728416.

[26] G. Memoli, M. Caleap, M. Asakawa, D.R. Sahoo, B. W. Drinkwater, and S. Subramanian. “Metamaterial bricks and quantization of meta-surfaces”. In: *Nature Communications* 8 (Feb. 2017). DOI: 10.1038/ncomms14608.

[27] Y. Xie, C. Shen, W. Wang, J. Li, D. Suo, B.-I. Popa, Y. Jing, and S. A. Cummer. “Acoustic Holographic Rendering with Two-dimensional Metamaterial-based Passive Phased Array”. In: *Scientific Reports* 6.35437 (2016). DOI: 10.1038/srep35437.

[28] A. Marzo, A. Ghobrial, L. Cox, M. Caleap, A. Croxford, and B. W. Drinkwater. “Realization of compact tractor beams using acoustic delay-lines”. In: *Applied Physics Letters* 110.014102 (2017). DOI: 10.1063/1.4972407.

[29] N. J. Smith and S. van der Walt. *mpl colormaps*. Jan. 2018. URL: https://bids.github.io/colormap/.

[30] K. Moreland. “Diverging Color Maps for Scientific Visualization”. In: *Advances in Visual Computing (Proceedings of the 5th International Symposium on Visual Computing)*. 2009. DOI: 10.1007/978-3-642-10520-3_9.

[31] R. Lerch, G. M. Sessler, and D. Wolf. *Technische Akustik*. Springer, Berlin, Heidelberg, 2009. DOI: 10.1007/978-3-540-49833-9.

[32] Ilja N. Bronstein, Heiner Mühlig, Gerhard Musiol, and Konstantin A. Semendjajew. *Taschenbuch der Mathematik*. 10th ed. Verlag Europa-Lehrmittel, 2016. ISBN: 978-3-8085-5789-1.

[33] A.W. Rudge, K. Milne, and A.D. Olver. *The Handbook of Antenna Design*. Electromagnetics and Radar Series Bd. 2. P. Peregrinus, 1982. ISBN: 9780906048870. URL: https://books.google.de/books?id=QjYtNJZmWLEC.

[34] M. Möser. *Technische Akustik*. Springer Berlin Heidelberg, 2005. ISBN: 978-3-540-26445-3. DOI: 10.1007/b137595. URL: http://www.springer.com/de/book/9783540264453.

[35] Rob Opdam, Raphael Kolk, Diemer de Vries, and Michael Vorländer. "Frequency and geometry dependent automated optimized meshing algorithm for a boundary element simulation". In: *Proc. 40. Deutschen Jahrestagung für Akustik*. Mar. 2014, pp. 375–376. URL: http://pub.dega-akustik.de/DAGA_2014/data/articles/000239.pdf.

[36] P.-O. Persson and G. Strang. "A Simple Mesh Generator in MATLAB". In: *SIAM Review* 46.2 (June 2005), pp. 329–345. URL: http://persson.berkeley.edu/distmesh/.

[37] R. Schmidt. "Multiple emitter location and signal parameter estimation". In: *IEEE Transactions on Antennas and Propagation* 34.3 (Mar. 1986), pp. 276–280. ISSN: 0018-926X. DOI: 10.1109/TAP.1986.1143830.

[38] J. Capon. "High-resolution frequency-wavenumber spectrum analysis". In: *Proceedings of the IEEE* 57.8 (Aug. 1969), pp. 1408–1418. ISSN: 0018-9219. DOI: 10.1109/PROC.1969.7278.

[39] *Zero-Height SiSonicTM Microphone*. Knowles Electronics, LLC. Itasca, IL, USA. URL: https://www.knowles.com/docs/default-source/model-downloads/spu0410lr5h-qb-revh.pdf.

[40] *MEMS-based microspeaker for headphones, wearables and array applications*. USound GmbH, Graz, Austria. URL: https://www.usound.com/images/pdf/Datasheets/Achelous-1.2.pdf.

[41] T.A. Milligan. *Modern Antenna Design*. Wiley - IEEE. Wiley, 2005. ISBN: 9780471720607. URL: https://books.google.de/books?id=PPyDQXAd09kC.

[42] S. Scott Crump. "Apparatus and method for creating three-dimensional objects". US5121329A. 1989. URL: https://patents.google.com/patent/US5121329A.

[43] J. Li, C. Shen, A. Díaz-Rubio, S. A. Tretyakov, and S. A. Cummer. "Systematic design and experimental demonstration of bianisotropic metasurfaces for scattering-free manipulation of acoustic wavefronts". In: *Nature Communications* 9.1342 (2018). DOI: 10.1038/s41467-018-03778-9.

[44] Richard H. Bartels, John C. Beatty, and Brian A. Barsky. *An introduction to splines for use in computer graphics and geometric modeling*. Los Altos, Calif., 1987. ISBN: 0934613273. URL: http://scans.hebis.de/HEBCGI/show.pl?12990353_toc.pdf.

[45] G.G. Lorentz. *Bernstein polynomials*. Mathematical expositions. University of Toronto Press, 1953. URL: https://books.google.de/books?id=ISjvAAAAMAAJ.

[46] L. Svilainis, V. Dumbrava, and G. Motiejunas. "Optimization of the ultrasonic excitation stage". In: *ITI 2008 - 30th International Conference on Information Technology Interfaces*. June 2008, pp. 791–796. DOI: 10.1109/ITI.2008.4588512.

[47] *4-Channel 5-Level, +/-80V Ultrasound Pulser with T/R Switches*. HV7321. Microchip. 2016. URL: http://ww1.microchip.com/downloads/en/DeviceDoc/20005639A.pdf.

[48] *8-Channel 7-Level, +/-80V High Voltage Pulser with T/R Switches*. HV7322. Microchip. 2017. URL: http://ww1.microchip.com/downloads/en/DeviceDoc/20005920A.pdf.

[49] *16 channels ±100 V, ±2/4 A, 5/3-level RTZ, high-speed ultrasound pulser with integrated transmit beamformer*. STHV1600. ST Microelectronics. 2018. URL: https://www.st.com/resource/en/data_brief/sthv1600.pdf.

[50] *Dual Channel, High-Voltage - Multi-Level Fully Integrated Ultrasound Transmitter*. TX517. Texas Instruments. 2011. URL: http://www.ti.com/lit/ds/symlink/tx517.pdf.

[51] *Eight Channel, High Speed, Unipolar, Ultrasound Pulser 1.5A 150V*. HV7355. Microchip. 2011. URL: http://ww1.microchip.com/downloads/en/DeviceDoc/HV7355.pdf.

[52] *8-Channel High-Speed ±60V ±1A Ultrasound RTZ Pulser*. HV7350. Microchip. 2016. URL: http://ww1.microchip.com/downloads/en/DeviceDoc/20005627A.pdf.

[53] *16-Channel, 3-Level, +/-80V High Voltage Pulser with integrated transmit beamformer*. HV7358. Microchip. 2018. URL: https://www.microchip.com/wwwproducts/en/HV7358.

[54] *Octal ±90 V, ±2 A, 3-level RTZ, high-speed ultrasound pulser*. STHV800. ST Microelectronics. 2014. URL: https://www.st.com/resource/en/data_brief/sthv800.pdf.

[55] "IEEE Standard for Ethernet". In: *IEEE Std 802.3-2015 (Revision of IEEE Std 802.3-2012)* (Mar. 2016), pp. 1–4017. DOI: 10.1109/IEEESTD.2016.7428776.

[56] D. Großkurth. "Control electronics for an ultrasound phased array in air". Master's Thesis. Technische Universität Darmstadt, May 2016.

[57] J. Hinrichs. "Development and design of receiving electronics for an ultrasonic phased array in air". Master's Thesis. Technische Universität Darmstadt, June 2017.

[58] G. Allevato. "Signal processing architecture for imaging using air-coupled ultrasound phased arrays". Master's Thesis. Technische Universität Darmstadt, July 2018.

[59] *Präzisionsdrehtisch*. M-061. Physikinstrumente (PI) GmbH und Co. KG. 2014.

[60] *Lineareinheiten*. LEZ 1. isel Germany AG. 2011. URL: https://www.isel.com/de/downloads/dl/file/id/9001/technische_daten_bestellangaben_aller_lineareinheiten.pdf.

[61] *1/8 Pressure-field Microphone*. Type 4138. Brüel & Kjær. 2017. URL: https://www.bksv.com/media/doc/bp2030.pdf.

[62] *24-Bit, Flexible Resolution PXI Oscilloscope*. PXI-5922. National Instruments. 2017. URL: http://www.ni.com/pdf/manuals/374033a.pdf.

[63] Bureau International des Poids et Mesures. *Guide to the expression of uncertainty in measurement (GUM)*. Mai 2018. URL: https://www.bipm.org/utils/common/documents/jcgm/JCGM_100_2008_E.pdf.

[64] A. Mazumdar. *Principles and Techniques of Schlieren Imaging Systems*. 2013. DOI: 10.7916/D8TX3PWV.

[65] Zheng Xu, Hao Chen, Xu Yan, Meng-Lu Qian, and Qian Cheng. "Three-dimensional reconstruction of nonplanar ultrasound fields using Radon transform and the schlieren imaging method". In: *The Journal of the Acoustical Society of America* 142.1 (2017), EL82–EL88. DOI: 10.1121/1.4994282.

[66] G. S. Settles. "Color schlieren optics - A review of techniques and applications". In: *International Symposium on Flow Visualization*. 1981, pp. 187–197.

[67] Carsten Unverzagt, Sergei Olfert, and Bernd Henning. "A new method of spatial filtering for Schlieren visualization of ultrasound wave fields". In: *Physics Procedia* 3.1 (2010). International Congress on Ultrasonics, Santiago de Chile, January 2009, pp. 935–942. ISSN: 1875-3892. DOI: https://doi.org/10.1016/j.phpro.2010.01.120.

[68] Harvard Natural Sciences Lecture Demonstrations. *Schlieren Optics*. Sept. 2018. URL: https://sciencedemonstrations.fas.harvard.edu/presentations/schlieren-optics.

[69] Y. Bendel. "Schlieren optics for visualizing the acoustic field of an ultrasound levitator". Bachelor's Thesis. Technische Universität Darmstadt, Apr. 2018.

[70] H. Winner, S. Hakuli, F. Lotz, and C. Singer. *Handbuch Fahrerassistenzsysteme*. ATZMTZ. Springer Vieweg, Wiesbaden, 2015. ISBN: 978-3-658-05734-3. DOI: 10.1007/978-3-658-05734-3.

[71] *MA58MF14-7N*. Murata Manufacturing Co., Ltd. URL: https://www.murata.com/en-sg/api/pdfdownloadapi?cate=cgsubUltrasonicSensors&partno=MA58MF14-7N.

[72] Texas Instruments Incorporated. *PGA450-Q1 Ultrasonic-Sensor Signal Conditioner*. URL: http://www.ti.com/lit/gpn/pga450-q1.

[73] J. Gätke. *Akustische Strömungs- und Durchflussmessung*. Akad.-Verlag, 1991. ISBN: 9783055008597. URL: https://books.google.de/books?id=bWtRAAAACAAJ.

[74] M. Kupnik, A. Schroder, and M. Groschl. "PS-16 Adaptive Asymmetric Double-Path Ultrasonic Transit-Time Gas Flowmeter". In: *2006 IEEE Ultrasonics Symposium*. Oct. 2006, pp. 2429–2432. DOI: 10.1109/ULTSYM.2006.543.

[75] K. S. Mylvaganam. "High-rangeability ultrasonic gas flowmeter for monitoring flare gas". In: *IEEE Transactions on Ultrasonics, Ferroelectrics, and Frequency Control* 36.2 (Mar. 1989), pp. 144–149. ISSN: 0885-3010. DOI: 10.1109/58.19144.

[76] F. C. Lowell and R. H. Lyon. "Method and apparatus for measuring flow by using phase advance". US5228347A. 1991. URL: https://patents.google.com/patent/US5228347A.

[77] H. Dassler, L. Thieme, and W. Manthey. "Broadband ultrasonic MEMS for liquids". In: *16th IMEKO World Congress*. Vol. 2. 2000, pp. 343–37.

[78] In: *Ultrasonic Measurements for Process Control*. Ed. by L. C. Lynnworth. San Diego: Academic Press, 1989. ISBN: 978-0-12-460585-5. DOI: 10.1016/B978-0-12-460585-5.50001-1.

[79] Lawrence C. Lynnworth. "Ultrasonic flowmeters using waveguide antennas". US4336719A. 1980. URL: https://patents.google.com/patent/US4336719A.

[80] Lawrence C. Lynnworth. "Ultrasonic buffer/waveguide". US6047602A. 1997. URL: https://patents.google.com/patent/US6047602A.

[81] A. J. Van Bekkuma, A. M. Heijnsdijk, C. J. Hogendoorn, A. Huijzer, M. .M. Molenaar, and J. C. Visser. "Sende- und/oder Empfangskopf eines Ultraschall-Durchflußmeßgerätes". DE19812458A1. 1998. URL: https://patents.google.com/patent/DE19812458A1.

[82] J. M. van Klooster. "Durchflußmeßgerät". DE10205545B4. 2002. URL: https://patents.google.com/patent/DE10205545B4.

[83] A. M. Heijnsdijk, C. J. Hogendoorn, A. Huijzer, M. .M. Molenaar, A. .J. Van Bekkum, and J. C. Visser. "Sende- und/oder Empfangskopf eines Ultraschall-Durchflussmessgeräts". EP1046886A1. 1999. URL: https://patents.google.com/patent/EP1046886A1.

[84] Ira Oaktree Wygant. "Three-Dimensional Ultrasound Imaging Using Costum Integrated Electronics Combined With Capacitive Micromachined Ultrasonic Transducers". PhD thesis. Stanford University, 2008.

[85] W.-S. Gan, J. Yang, and T. Kamakura. "A review of parametric acoustic array in air". In: *Applied Acoustics* 73.12 (2012). Parametric Acoustic Array: Theory, Advancement and Applications, pp. 1211–1219. ISSN: 0003-682X. DOI: https://doi.org/10.1016/j.apacoust.2012.04.001.

[86] D. Olszewski. "Stark gerichtete Audio-Beschallung mit parametrischem Ultraschall-Lautsprecher". PhD Thesis. Universität Paderborn, Feb. 2008. URL: https://d-nb.info/989972852/34.

[87] T. Tanaka, M. Iwasa, Y. Kimura, and A. Nakamura. "Directional loudspeaker system". US4823908A. 1985. URL: https://patents.google.com/patent/US4823908A/en.

[88] K. Manabe. "Super-directional loudspeaker using ultrasonic wave". 1999. URL: https://patents.google.com/patent/US6556687B1/en.

A List of symbols

Symbol	Unit	Value	Description
$\varnothing$	m	-	Diameter
A	m^2	-	Area
AZ	rad	-	First angle in the AZ/EL coordinate system.
$B_{i,n}$	-	-	i-th Bernstein polynom of the n-th order.
E	1		Dimensionless directivity factor.
EL	rad	-	Second angle in the AZ/EL coordinate system.
F_1, F_2	-	-	Focus points of a hyperbola.
FP	-	-	Focal point.
H	-	-	Hyperbola
L	m		Length of acoustic path in flowmeter.
N	m		Near field distance.
R_t	m		Transducer diameter
Re	1		Reynolds number.
T	s		Duration of time period
c	$m\,s^{-1}$	$343\,m\,s^{-1}$	Speed of sound.
d	m	-	Distance between two adjacent transducers.
e	-	-	Eccentricity of a hyperbola.
f	s^{-1}	typical 40 kHz	Frequency
f_1	m	-	Focal length
i	1	-	Index variable of integer set.
k	$rad\,m^{-1}$	$2\pi/\lambda$	Angular wavenumber.
n	1	-	Number of elements in integer set.
p	$Pa = N\,m^{-2}$		Pressure
r	m	-	Distance to the origin in spherical or AZ/EL-coordinates.
t	1	-	Variable for parametrization.
t_{up}	s		Time of flight for the upstream sound path.
t_{down}	s		Time of flight for the downstream sound path.
v	$m\,s^{-1}$	-	Velocity on transducer surface.
v_P	$m\,s^{-1}$	-	Flow velocity in flow meter application along path.
v_A	$m\,s^{-1}$	-	Average flow velocity over cross-section area.
Δs	m	-	Difference in distance.
Ψ	rad	-	Phase shift between transducer signals.
α	rad	-	Designator for angle in the context of the goniometer and for flow metering
β	rad	-	Designator for angle in the context of the goniometer and for flow metering
δ	-	-	Dirac's delta distribution.
λ	m	typical 8.6 mm	Wavelength
ρ	$kg\,m^{-3}$	-	Density
φ	rad	-	First angle in a spherical coordinate system.
ϑ	rad	-	Second angle in a spherical coordinate system.
ϑ_g	rad	-	Angle of grating lobe.
ϑ_{res}	rad	-	Angular resolution.
ϑ_{res}	rad	-	Maximum steering angle.
ϑ_s	rad	-	Steering angle.

B List of abbreviations

ABS acrylonitrile butadiene styrene

ADC analog digital converter

A-scan amplitude scan

B-scan brightness scan

CT scan computed tomography scan

CAD computer aided design

DDS Direct Digital Synthesis

DOA Direction of Arrival

DS Delay and Sum

DSLR digital single-lens reflex

DUT device under test

FEM Finite Element Method

FDM fused deposition modeling

FIR finite impulse response

FNBW first null bandwidth

FPGA Field Programmable Gate Array

GIMP GNU image manipulating program

GPU graphics processing unit

HiFU high intensity focused ultrasound

IC integrated circuit

LED light emitting diode

LTE long term evolution

MEMS micro electro mechanical system

NDT non-destructive testing

RADAR radio detection and ranging

ROI region of interest

RX receive

TX transmit

PA public address system

PDC park distance control

PC personal computer

PCB printed circuit board

PETG polyethylene terephthalate

PLA polylactic acid

SLM selective laser melting

SNR signal-to-noise-ratio

SoC system on chip

SPL sound pressure level

TOF time-of-flight

VGA variable gain amplifier

WIFI wireless lan